Editorial corner – a personal view
Nanocomposite fibres: a strategy for stronger materials?

*A. Pegoretti**

Department of Materials Engineering and Industrial Technologies, University of Trento, via Mesiano 77, 38123 Trento, Italy

The scientific literature is full of claims for the exceptional potentialities of nanoscale reinforcing materials, such as nanoparticles, nanofibres, nanotubes and nanoplatelets, to improve the mechanical properties of polymer matrices. However, most of the reliable data on the effective properties of polymer nanocomposites are somewhat disappointing, particularly when compared to structural composites reinforced with high-performance continuous fibers. The main reasons advocated to explain the discrepancies with theoretical predictions include poor dispersion, inadequate alignment of nanofillers, and bad stress-transfer ability at the interface (i.e. poor adhesion with polymer matrix).

A possible route for introducing nanofillers into polymer matrices, and retaining a certain control on orientation and improving the dispersion level, can be offered by polymer fibres technology. In fact, the elevated draw ratios and elongational flow involved in typical fibre production processes can concurrently promote a disruption of the aggregates and a strong orientation of the nanofillers along the fibre axis. A variety of processing techniques can be adopted for the production of nanocomposite fibres, including spinning from polymer melts or solutions, gel-spinning, melt-blowing and electrospinning.

This approach has been proven to be extremely efficient when nanofillers with an elevated aspect ratio, such as nanofibres or nanotubes, are concerned. In fact, in the last decade several papers have been published documenting the extraordinary reinforcing efficiency of single- or multi-walled carbon nanotubes in highly oriented polymer fibres or tapes.

More recently, some successful attempts have been made to extend this approach to nanoplatelets, in particular layered silicates and graphene.

Among the drawback to overcome, one can list the marked viscosity increments generally induced by nanofillers in polymer matrices, and the consequent necessity to identify proper processing conditions for the fibre production. Moreover, the decrease of elongation at break (which is also reflected in the molten state) typically induced by some nanofillers may also limit fibre preparation possibilities.

The outstanding properties of nanocomposite fibres could improve traditional textile products, or be exploited in some advanced processing technologies, such as single- or all-polymer composites and commingled yarns composites.

Prof. Dr. Alessandro Pegoretti
Member of International Advisory Board

*Corresponding author, e-mail: alessandro.pegoretti@unitn.it

Synthesis, morphology and rheology of core-shell silicone acrylic emulsion stabilized with polymerisable surfactant

H. H. Wang*, X. R. Li, G. Q. Fei, J. Mou

Key laboratory of Auxiliary Chemistry and Technology for Chemical Industry, Ministry of Education. Shaanxi University of Science and Technology, Xi'an, 710021, P.R. China

Abstract. Core-shell silicone acrylic emulsions with 3-methacryloxypropyl trimethoxysilane (MPTS) in the shell were prepared by seeded polymerization with the assistance of polymerisable maleate surfactant (MT). Fourier transform infrared (FT-IR) demonstrated the incorporation of polymerisable surfactant in copolymer. It was found that small amount of octadecyl acrylate was beneficial to emulsion stability with decreasing the particle size from 194.6 to 165.7 nm. It was also found that the particle size increased from 165.7 to 242.9 nm with the increase of MPTS concentration. Furthermore, rheological measurement indicated that the emulsion was endowed with pseudoplasticity. At low shear rate, marginal reduction in viscosity was detected when MPTS concentration increased to 2%, while great increase in viscosity was observed with higher MPTS concentration, the interaction force among emulsion particles became the predominant factor instead of particle size. In addition, better water resistance was observed when MT concentration was lower than 1.5%, and MPTS concentration higher than 2%. Moreover, surface roughness was increased with MPTS addition, the crosslinking among core and shell reconstructed the surface morphology of film.

Keywords: polymer synthesis, core-shell, rheology, morphology

1. Introduction

Polyarylate and poly(arylate-styrene) have been widely used in coatings, paints and adhesives so forth by virtue of excellent film-forming property, cohesiveness, gloss retention, and drying capacity. However, disadvantages in water resistance, mechanical property and weather resistance limit their applications [1–3]. In contrast, polysiloxane is endowed with excellent thermal stability, low surface energy, weather resistance, high flexibility and good biological compatibility owing to its unique structure [4–8]. In the past decades, research on silicone (or polysiloxane) modified polyarylate and poly(arylate-styrene), especially the product of core-shell structure, has attracted special attention of many researchers [9–12].

It is common knowledge that it is much easier to obtain core-shell morphology particles by seeded emulsion polymerization when the seed polymer is more hydrophobic than the shell polymer [13]. Therefore, normal core/shell morphology with hydrophobic polysiloxane (PSi) as the core and with hydrophilic polyacrylate (PA) as the shell can be easily formed, while it's difficult to obtain PA/PSi core/shell particles in emulsion polymerization [4, 14]. It is obvious that excellent surface properties can be created with small amount of PSi on the shell, which is beneficial to cost reduction. Under such circumstances, dispersion polymerization in alcoholic media is put forward and is demonstrated to be an effective way for the preparation of PA/PSi core/shell particles [2, 4, 15]. In addition, seeded

polymerization [14–16] and sol-gel process [17] are also adopted to prepare core-shell particles with PSi as the shell. Zou *et al.* [16] points out that nanometer scale particles of latex can be successfully prepared by seeded polymerization induced by gamma rays. Kan *et al.* [10] state that perfect PA/ PSi core/shell particles can be synthesized when both the core and shell polymers are crosslinked, and 3-methacryloyloxyrpopyl trimethoxysilane has often been used as a crosslinking agent to form an intermediate layer between core and shell. However, ethanol and methanol have been utilized as medium instead of water in dispersion polymerization, which is detrimental to environment.

The main objective of this study is to prepare stable core-shell poly(butyl acrylate)-poly(styrene-butyl acrylate-3-methacryloxypropyl trimethoxysilane) (PBA-PSBM) emulsion particles with the assistance of polymerisable maleate surfactant with long branches, together with hydrophobic costabilizer octadecyl acrylate (ODA). Besides, seeded polymerization with water medium was adopted to prepare the emulsion. To date, no study about this system has been reported. It has been demonstrated that polymerisable surfactants exhibit an exceptionally high degree of incorporation into the emulsion polymer, protecting the emulsion from flocculation. Furthermore, the limited mobility of polymerisable surfactants avoids surface migration and the formation of hydrophilic domains in the films, resulting in greatly reduced process foaming, enhanced solvent resistance, improved adhesive and mechanical properties, and far less residual levels in effluent streams, as compared with nonreactive surfactants [22–27]. Anionic polymerisable maleate surfactants have already gotten extensive attention from a point of view of reactivity/copolymerization behavior [28, 29], and hydroxyethyl methacrylate on maleic anhydride is now available commercially [27]. However, since they are simply anionic, they don't provide steric stabilization and emulsions flocculate upon high shearing conditions or the addition of strong electrolytes or in freezing test. Maleate polymerisable surfactant with long

branches was thereby synthesized which was able to provide electrostatic stabilization as well as steric stabilization.

In this research, seeded polymerization with water as medium was adopted to prepare PBA-PSBM core-shell emulsion, which was carried out under starved-feed addition of shell to prevent secondary nucleation and benefit to form core-shell structure [18–21]. And 3-methacryloxypropyl trimethoxysilane (MPTS) was introduced into the shell of the emulsion particles to endow them with self-crosslinking properties in the film-forming process. Rheology, dynamic light scattering, transmission electron microscopy (TEM), as well as static contact angle and so on were performed to investigate the properties and morphology of core-shell particles.

2. Experimental section
2.1. Materials

3-Methacryloxypropyl trimethoxysilane (MPTS) (Wuhan Institute of Applied Technology, China) and nonyl phenol ethoxylate (TX-10) (Tianjin Kermel Chemical Reagent Co., Ltd, China) were used as received. Maleic anhydride (MAH), sodium bisulfite ($NaHSO_3$), potassium persulfate, and aqueous ammonia ($NH_3 \cdot H_2O$) from Tianjin Dengfeng Chemical Reagent Co. (China) were all analytically pure grades, and were used without further purification. The analytical reagents butyl acrylate (BA), methacrylic acid (MAA), styrene (St) and octadecyl acrylate (ODA) were all purchased from Tianjing Chemical Reagent Factory (China) and were distilled under vacuum before use.

2.2. Synthesis of polymerisable Surfactant (MT)

1 mol maleic anhydride and 1mol nonyl phenol ethoxylate were stirred in a melted state at 70°C for 3 h. $NH_3 \cdot H_2O$ was then added dropwise to the reaction mixture to adjust pH value of reaction system to 6 and thereafter the temperature was maintained
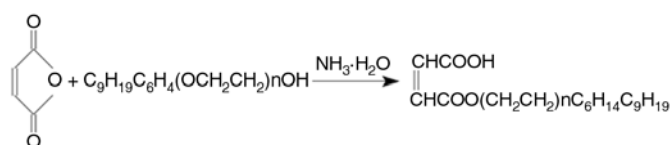

Figure 1. The chemical reaction of polymerisable surfactant

in the range of 90–95°C until the solution becomes transparent. After 2 h of reaction, a kind of transparent solution with 35% solid content, that is, polymerisable surfactant (MT) was obtained by adding certain amount of distilled water. The reaction scheme was shown in Figure 1.

2.3. Preparation of poly (BA-n-ODA) seed emulsion

Polymerisable surfactant (MT) of different amounts and distilled water were introduced into a 250 ml four-necked flask equipped with a reflux condenser, a mechanical stirrer and a digital thermometer. Then 16 g BA, 0.5 g MAA, 0.1 g NaHSO$_3$ and ODA of different amount were added into the flask. After additional 30 min equilibration at 70°C, 0.3 g potassium persulfate aqueous solution was dropped into the flask in 1 h and the final mixture was reacted at 70°C for additional 2 h, the structure of seed copolymer was shown in Figure 2.
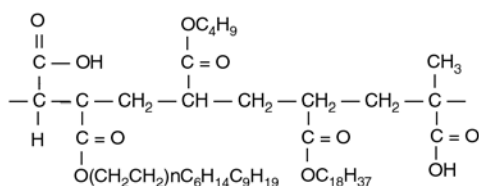

Figure 2. Structure of seed copolymer

2.4. Seeded emulsion polymerization

Using the particles prepared above as seeds, 0.2 g NaHSO$_3$ and water was added into the seed emulsion. Then 16 g St, 16 g BA, 1.0 g MAA and various amounts of MPTS in the dropping funnel was fed slowly into the flask under starved-feed addition, and simultaneously 0.5 g potassium persulfate aqueous solution was introduced into the flask in another dropping funnel with an appropriate dropping rate. The reaction was kept for another 2 h after the addition was completed. Then the obtained emulsion was cooled to room temperature and then
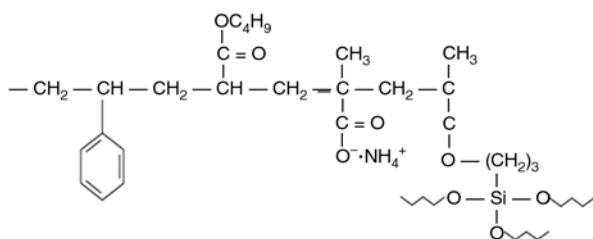

Figure 3. Structure of shell copolymer

ammonia was added to adjust the pH value of emulsion in the range of 7–8. The structure of shell copolymer was shown in Figure 3.

2.5. Structural analysis

Fourier transform infrared (FT-IR) spectra were recorded on a Bruker Vector22 (Germany) Fourier Transform Infrared Spectrometer in the range from 4000 to 400 cm^{-1}, by using polymer films. ^{1}H NMR and ^{13}C NMR were performed on a Bruker Avance 400 MHz Spectrometer (Germany) with D$_2$O as solvent.

2.6. Stability of emulsions

Centrifugal stability was determined by centrifugal method. Emulsions were filtered by 100 mesh sieve to remove impurities, and then 10 g emulsions were submitted to TDL-10B centrifuge (Shanghai Anting Scientific Instrument Factory, China) for 30 min at the speed of 3000 r/min. Electrolyte-resistant stability was determined by adding electrolyte solutions to lattices. 5% CaCl$_2$ solution was added into the emulsion and kept for 48 h, the ratio of coagulate was used as the standard for estimating emulsion stability. The ratio of coagulate (σ) was calculated by Equation (1) [27]:

$$\sigma[\%] = \frac{w_c}{w_m} \cdot 100 \tag{1}$$

where w_c is the weight of dried coagulates and w_m is total weight of all monomer. The larger the values of σ, the worse the stabilities are.

2.7. Particle size and morphology measurement

The particle size of the emulsions was analyzed by Ver 2.14 dynamic light scattering (Zeta-plus, Brookhaven Instruments Co. US). Its morphology was observed by Japanese Hitachi S570 transmission electron microscope (TEM) with phosphotungstic acid as staining agent.

2.8. Rheology measurement

The rheological properties of emulsions were analyzed in an American TA Instrument® AR2000ex Rheometer. Steady state flow tests (shear rate from

0.01 to 100 s^{-1}) were carried out at 25°C using DIN concentric cylinders geometry. Sample period: 0:00:01, percentage tolerance: 5.0, consecutive within tolerance: 3, maximum point time: 0:01:00.

2.9. Atomic force microscopy (AFM)

The films were prepared by spin coating in a freshly cleaved glass plate. The film was dried for a few minutes in air at room temperature before observation by Japanese Seiko SPI3800N/SPA 400 atomic force microscopy (AFM). All measurements were made in the contact mode.

2.10. Water resistance

Membranes were cut into circular disks by using a sharp-edged stainless steel die with inner diameter of 20 mm. The samples were dried in vacuum oven for 24 h to determine their dry weight (W). Absorption of the membranes was determined by immersing the membranes in a beaker of medium for 24 h. After wiping off the surface water with a piece of filter paper, its weight (W_1) was determined. The absorption (WS) of the films was calculated by Equation (2):

$$WS = \frac{W_1 - W}{W} \cdot 100 \qquad (2)$$

2.11. Contact angle

Contact angles were measured with a JJC-1 contact angle goniometer (Chengde Tester factory, P.R. China) at 27°C with water as medium, and the results reported are the mean values of 5 replicates.

3. Results and discussion
3.1. Structure analysis

The ^{1}H NMR and ^{13}C NMR spectra of TX-10 and MT were presented in Figure 4 and Figure 5, respectively. As shown in Figure 4, the characteristic peaks of the protons in the –CH=CH– group ($\delta = 6.17$ ppm) in ^{1}H NMR spectrum of MT demonstrate the reaction between maleic anhydride and TX-10, which is further certified by ^{13}C NMR spectra. As shown in Figure 5, the characteristic peaks at $\delta = 170.61$ ppm can be assigned to carbons in –C=O group of MT, while peaks at $\delta =$
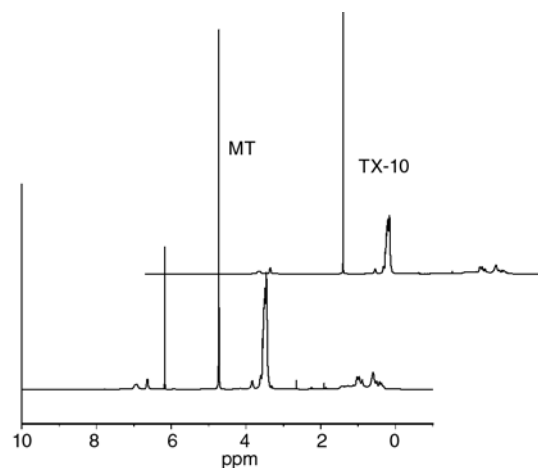
Figure 4. ^{1}H NMR spectrum of TX-10 and MT

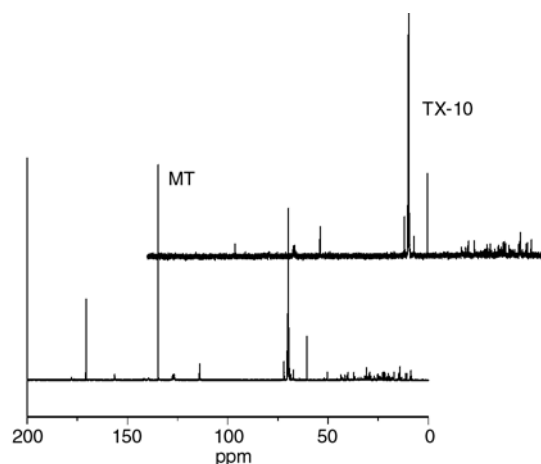**Figure 5.** ^{13}C NMR spectrum of TX-10 and MT

134.62 ppm results from –C=C– group in MT. Therefore, it can be concluded that polymerisable surfactant was successfully prepared.

The FT-IR spectra of MT polymerisable surfactant and core/shell polymer were shown in Figure 6. The existence of –COOH in MT could be confirmed by the broad peak at 3482 cm^{-1}, –C=O stretching vibration at 1733 cm^{-1} and –C–O stretching vibration at 1248 cm^{-1}. While the characteristic peak at 3482 cm^{-1} disappears in core-shell polymer, and the characteristic peak corresponding to –C=O at 1732 cm^{-1} gets stronger, the main reason can be attributed to the transfer from carboxylic acid to carboxylic salt.

It is also found that the characteristic peaks corresponding to the stretching vibration of CH=CH in the region of 1650 to 1500 cm^{-1} in FTIR spectrum of MT are absent in the spectrum of core-shell polymer, as well as the bending vibration of CH=CH at 948 cm^{-1}, demonstrating the incorporation of MT in copolymer material.
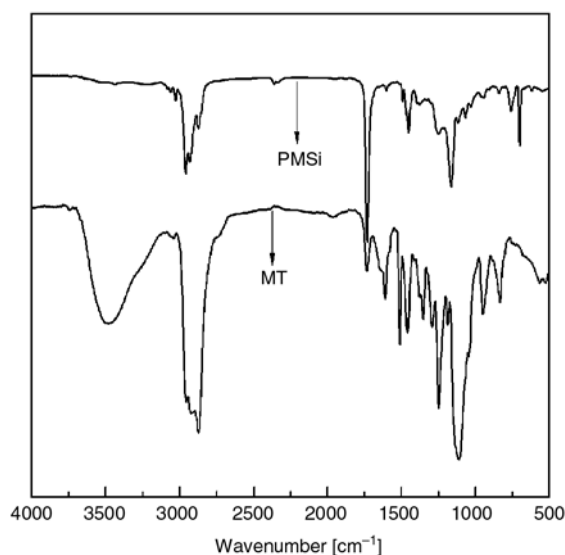
Figure 6. FT-IR spectra of polymerisable surfactant (MT) and core/shell polymer

3.2. Effects of polymerisable surfactant

Figure 7 showed effects of MT concentration on emulsion stability without any ODA and MPTS addition. It can be seen that the coagulate ratio decreased with the increase of MT and kept almost invariable when MT concentration was greater than 2% (based on total weight of monomer, the following were the same), without displaying decreasing trend with higher MT concentration. It has been reported that redundant surfactant would homopolymerize to form waterborne polymer chain that can cause flocculation, resulting in lower stability with higher surfactant concentration [29]. While for MT, it is difficult for homopolymerization to take place among MT molecules owing to its long branches, which can stabilize the emulsion through electros-
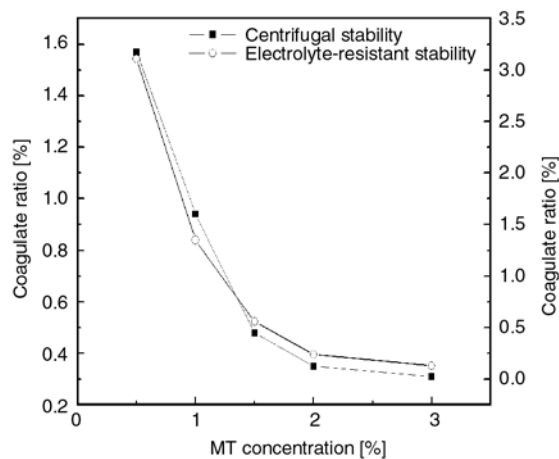
teric effects. 1.5% MT was utilized for preparation of the following samples.

3.3. Effects of octadecyl acrylate (ODA)

Octadecyl acrylate, as a kind of vinyl monomer possessing long and highly hydrophobic side chain, can improve micelle solubilization to a certain extent, to date some block copolymers containing polyoctadecyl segments have been reported to be used as stabilizers [30]. Effects of ODA concentration on emulsion stability with 1.5% MT and 0% MPTS were presented in Figure 8. It was found that ODA concentration should be neither too high nor too low. With the increase of ODA concentration, the emulsion stability increased accordingly, but decreased greatly when ODA concentration was more than 0.5%. It is stated that the destabilization of the droplets can be efficiently slowed down by an addition of a hydrophobic agent to the dispersed phase which counteracts the droplet pressure or Laplace pressure of the droplet [31]. The hydrophobe can act as an osmotic stabilizing agent. However, the hydrophobicity of copolymer chain was increased simultaneously, which will weaken the emulsion stability and result in the increase of coagulate ratio.

At the same time, effects of ODA concentration on particle size were analyzed, as shown in Figure 9. The average particle size decreased from 194.6 to 165.7 nm with 0.5% ODA addition, and increased to 187.0 nm with further increase of ODA concentration to 1.0%. The main reason is that ODA can act as a kind of costabilizer during copolymerization, which can reduce the diffusion of the monomer
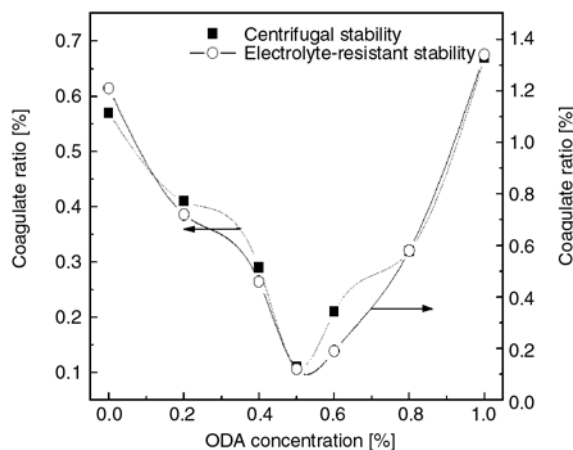

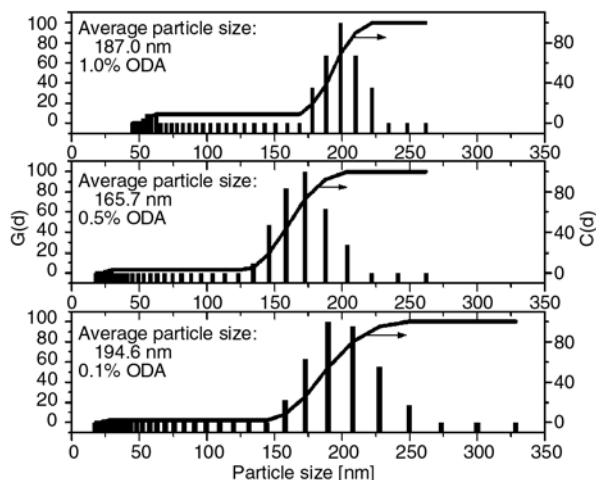**Figure 7.** Emulsion stability with different MT concentration

Figure 8. Emulsion stability with different ODA concentration

Figure 9. Particle size of emulsion with different ODA concentration

Figure 11. Particle size of the core/shell emulsion with different MPTS concentration

from smaller droplets to the larger one [32], resulting in the shrinkage of droplets with lower ODA concentration. Whereas the size of droplets with higher hydrophobe concentration will increase till the chemical potential in all droplets is equilibrated [31]. The following samples in this paper were prepared with 0.5% ODA.

3.4. Effect of 3-methacryloxypropyl trimethoxysilane (MPTS)

MPTS is a kind of important copolymerization monomer with self-crosslinking property in the film-forming process, which plays an important role in the improvement of water resistance and mechanical property. However, the Si–O–C bond in MPTS molecules is much easier to hydrolyze and condense both in acidic media and alkali media, which would bring instability to the emul-
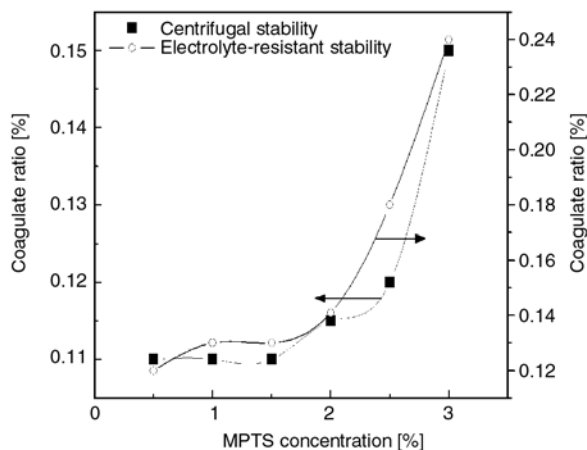
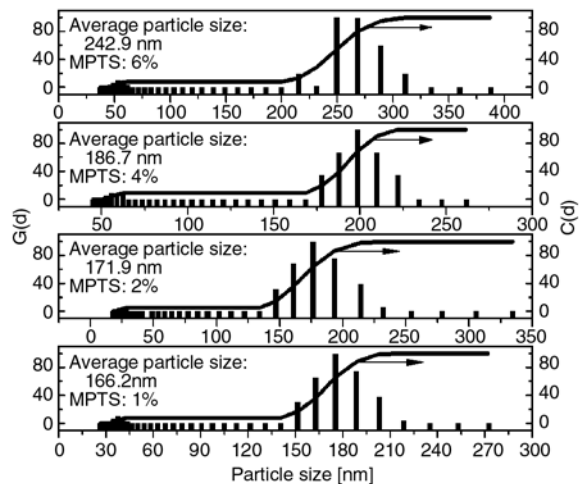sions [1]. Effects of MPTS concentration on emulsion stability with 1.5% MT and 0.5% ODA were presented in Figure 10. The emulsion kept stable when MPTS concentration was less than 4.0%, but the amount of precipitate increased greatly beyond this point, indicating that increasing Si–OH concentration resulted in the instability of emulsions.

The average particle size of the emulsions with different MPTS concentration by DLS was shown in Figure 11. A monotonic increase in particle size from 165.7 to 242.9 nm with MPTS addition was observed. With the increase of MPTS concentration, the polymer chain length increased due to the crosslinking, causing a lower growing particle number, as a result, the diameter of particles become larger.

TEM micrographs of the seed particles and core/shell particles with 4% MPTS were shown in Figure 12 and Figure 13, respectively. As shown in Figure 12, all the PBA seed particles were spherical in shape with white color. It is also evident that the

Figure 10. Effect of MPTS concentration on emulsion stability
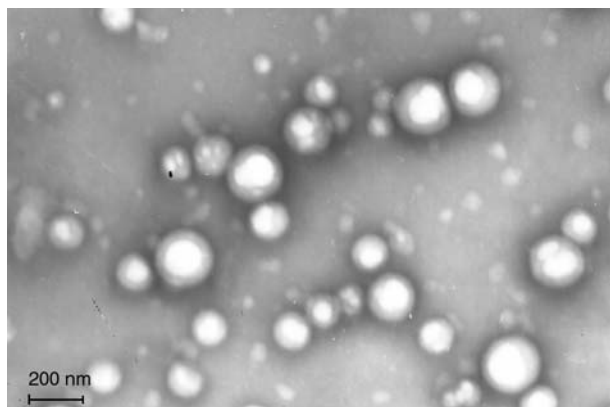

Figure 12. TEM micrograph of seed emulsion (×50 000)

Figure 13. TEM micrograph of core/shell emulsion with 4% MPTS (×50 000)

deposition of black PSBM shell onto the white seed particles is uniform without any voids, further indicating expectant PBA-PSBM core-shell structure has been formed in this study. And covalent bond between core and shell formed by MPTS can contribute to this phenomenon, too.

3.5. Rheological properties of core-shell emulsion

The viscosities and shear stress of core/shell emulsions with different MPTS concentration were plotted as a function of shear rate in Figure 14 and Figure 15, respectively. It was striking that the viscosity decreased greatly with the increase of shear rate at the start and then gradually to a constant level, indicating that the core/shell emulsions were endowed with pseudoplasticity.

At low shear rate, marginal reduction in viscosity and shear stress was detected when MPTS concen-
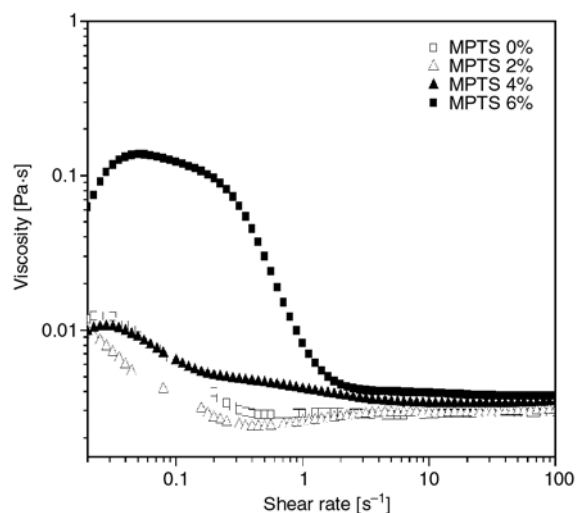

Figure 14. Viscosity versus shear rate curves with variation in MPTS concentration
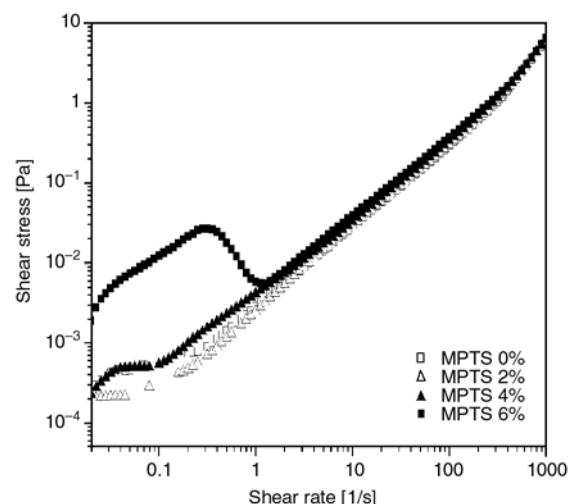

Figure 15. Shear stress versus shear rate curves with variation in MPTS concentration

tration increased to 2%, which could be ascribed to the increase of particle size. A smaller particle size generally increased the low shear viscosity due to colloidal interactions. However, a period of plateau was observed, as well as great increase in viscosity when MPTS concentration was greater than 4%, indicating interaction force among latex particles became the predominant factor influencing the viscosity instead of particle size.

While when shear rate was greater than 1 s^{-1}, the viscosity became constant with shear rate and simultaneously increased slightly with MPTS concentration, since viscosity is often independent of particle size at higher shear rates, as hydrodynamic forces dominate.

3.6. AFM analysis

AFM was used to examine the film surface and to measure its surface topography. The AFM pictures of core/shell emulsion films with 0 and 4% MPTS were shown in Figure 16 and Figure 17, respectively. The surface of the film with 0% MPTS showed a lower root-mean-square roughness value compared with the film with 4% MPTS, indicating increased surface roughness with MPTS addition. Therefore it was evident that the cross-linking between core and shell induced by MPTS reconstructed the surface morphology of the film. And the root mean square roughness induced by entanglements and penetration of molecular chain increased in the process of film-forming, demonstrating the increase of particle size, which was
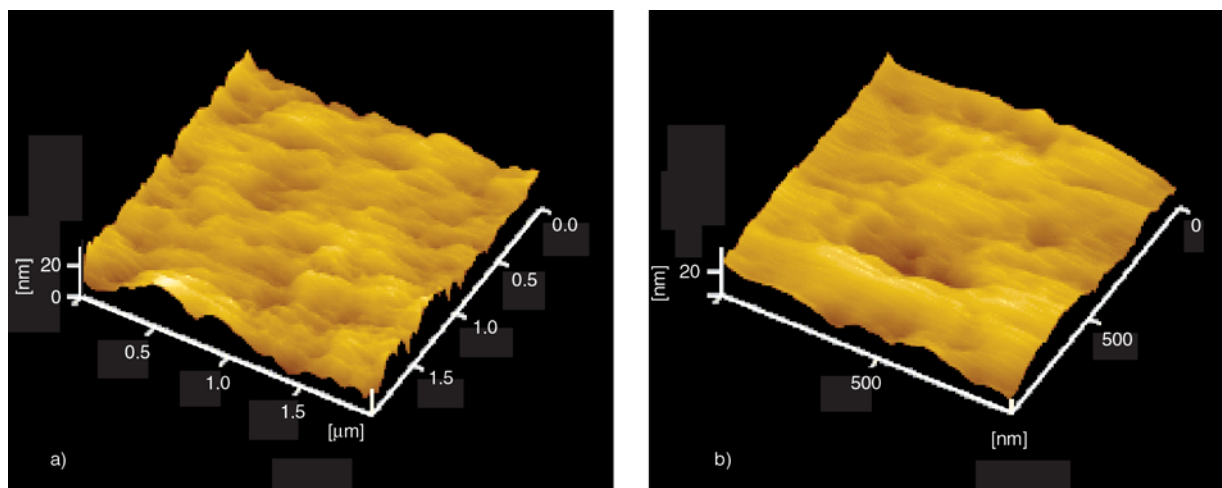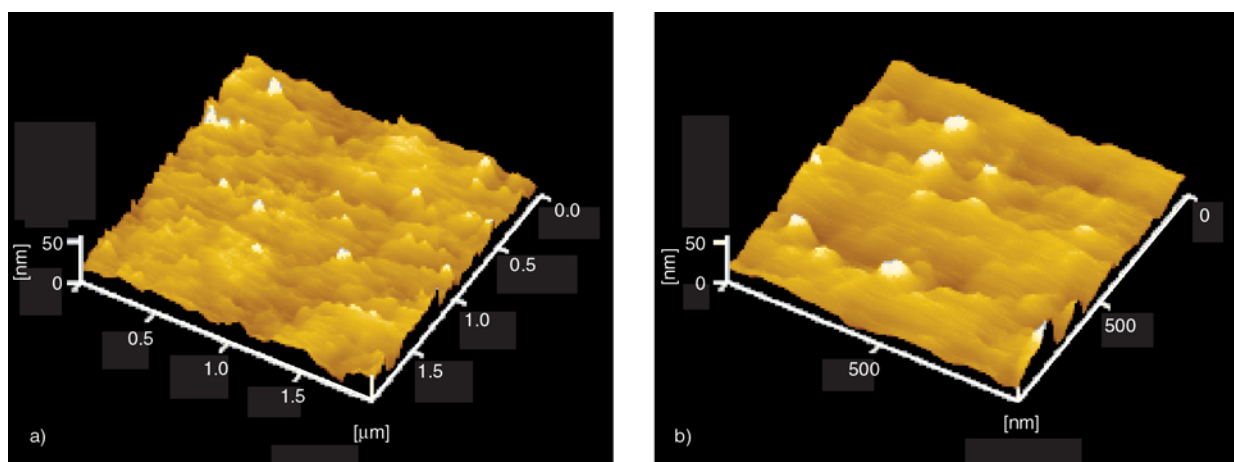
Figure 16. AFM images of the film with 0.0% MPTS

Figure 17. AFM images of the film with 4% MPTS

coincident with the aforementioned results shown in Figure 11.

3.7. Water resistance analysis

Figure 18 presented effects of MT concentration on the water absorption and contact angle of the films. As MT concentration increased from 0.5 to 1.5%, the water absorption decreased from 8.33 to 5.26%, and contact angle increased from 54 to 79°. However, when MT concentration exceeded 1.5%, the water absorption increased from 5.26 to 22.51%, contact angle decreased from 79 to 64°. The particle size was relative smaller with higher MT concentration, resulting in better particle packing and thus leading to the decrease of water absorption. On the other hand, hydrophilic groups greatly increased with the further increase of MT concentration, so the MT concentration can't be too high, or else water resistance will be weakened.
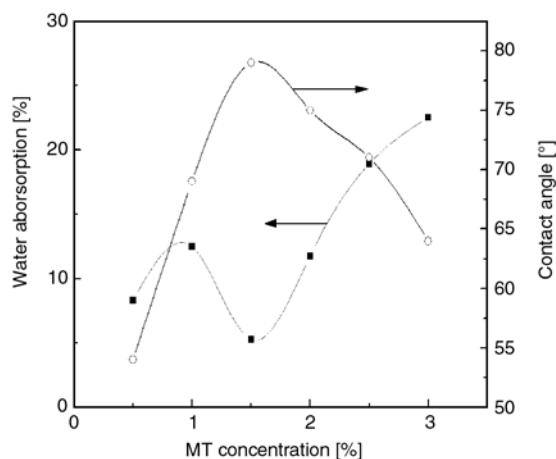

Figure 18. Effect of MT concentration on water absorption and contact angle of the films

Effects of MPTS concentration on the water absorption of the films were also investigated, as shown in Figure 19. It was found that the water absorption decreased with MPTS addition, providing a powerful proof that water resistance was
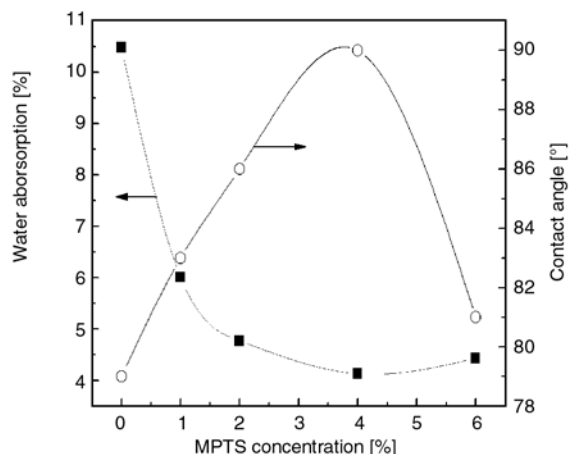
Figure 19. Effect of MPTS concentration on water absorption and contact angle of the films

enhanced by MPTS addition. It was also found that the surface contact angle increased with MPTS addition, indicating hydrophobic surface can be obtained by introducing MPTS into the shell. Conventionally, hydrophobic surfaces have been produced mainly in two ways. One is to create a rough structure on a hydrophobic surface, and the other is to modify a rough surface by materials with low surface free energy [17]. Therefore, the relative rougher surface created by MPTS (as shown in Figure 17) can be considered as another motivation for hydrophobicity improvement in addition to increased hydrophobic moieties and crosslinking degree in the shell.

4. Conclusions

Core-shell silicone acrylic emulsions with 3-methacryloxypropyl trimethoxysilane (MPTS) in the shell were successfully prepared by seeded polymerization with the assistance of polymerizable maleate surfactant. Emulsions were endowed with excellent stability when MT concentration was higher than 2.0% and ODA concentration was 0.5%. The particle size decreased from 194.6 to 165.7 nm with 0.5 % ODA addition, and increased to 187.0 nm with further addition of ODA. It was also found that the emulsion kept stable when MPTS concentration was less than 4.0%, and the particle size increased from 165.7 to 242.9 nm. Furthermore, emulsions were endowed with pseudoplasticity. At low shear rate, marginal reduction in viscosity was detected when increased to 2%, how-

ever, great increase in viscosity was observed with higher MPTS concentration, the interaction force among emulsion particles become the predominant factor instead of particle size. On the contrary, the viscosity became constant when shear rate was greater than 1 s⁻¹. In addition, the surface roughness was increased with MPTS addition, the crosslinking among core and shell reconstructed the surface morphology of film. And water resistance could be improved with MPTS addition.

Acknowledgements

References

[1] Guo T. Y., Chen X., Song M. D., Zhang B. H.: Preparation and properties of core [poly(styrene-*n*-butyl acrylate)]-shell [poly(styrene-methyl methacrylate-vinyl triethoxide silane)] structured latex particles with self-crosslinking characteristics. Journal of Applied Polymer Science, **100**, 1824–1830 (2006).
DOI: 10.1002/app.23081

[2] Cao S. S., Liu B. L., Deng X. B., Li S. J.: Core/shell particles containing 3-(methacryloxypropyl)-trimethoxysilane in the shell: Synthesis, characterization, and application. Macromolecular Bioscience, **5**, 669–676 (2005).
DOI: 10.1002/mabi.200500011

[3] Bauer F., Gläsel H. J., Decker U., Ernst H., Freyer A., Hartmann E., Sauerland V., Mehnert R.: Trialkoxysilane grafting onto nanoparticles for the preparation of clear coat polyacrylate systems with excellent scratch performance. Progress in Organic Coatings, **47**, 147–153 (2003).
DOI: 10.1016/S0300-9440(03)00117-6

[4] Liu B. L., Deng X. B., Cao S. S., Li S. J., Luo R.: Preparation and characterization of core/shell particles with siloxane in the shell. Applied Surface Science, **252**, 2235–2241 (2006).
DOI: 10.1016/j.apsusc.2005.03.223

[5] Lin F., Song M., He Z., Zhang T.: Synthesis and structural characterization of methacrylic acid/octadecyl acrylate-graft-poly(methylhydrosiloxane) by hydrosilylation. Journal of Applied Polymer Science, **107**, 3773–3780 (2008).
DOI: 10.1002/app.27487

[6] Turner J. S., Cheng Y. L.: Preparation of PDMS-PMAA interpenetrating polymer network membranes using the monomer immersion method. Macromolecules, **33**, 3714–3718 (2000).
DOI: 10.1021/ma991873k

[7] Liu B. L., Zhang B. T., Cao S. S., Deng X. B., Hou X., Chen H.: Preparation of the stable core-shell latex particles containing organic-siloxane in the shell. Progress in Organic Coatings, **61**, 21–27 (2008).
DOI: 10.1016/j.porgcoat.2007.08.008

[8] Zaioncz S., Dahmouche K., Paranhos C. M., Gil R. A. S., Soares B. G.: Relationships between nanostructure and dynamic-mechanical properties of epoxy network containing PMMA-modified silsesquioxane. Express Polymer Letters, **3**, 340–351 (2009).
DOI: 10.3144/expresspolymlett.2009.43

[9] Kan C. Y., Kong X. Z., Yuan Q., Liu D. S.: Morphological prediction and its application to the synthesis of polyacrylate/polysiloxane core/shell latex particles. Journal of Applied Polymer Science, **80**, 2251–2258 (2001).
DOI: 10.1002/app.1329

[10] Kan C. Y., Liu D. S., Kong X. Z., Zhu X. L.: Study on the preparation and properties of styrene-butyl acrylate-silicone copolymer lattices. Journal of Applied Polymer Science, **82**, 3194–3200 (2001).
DOI: 10.1002/app.2178

[11] He W-D., Pan C-Y.: Influence of reaction between second monomer and vinyl group of seed polysiloxane on seeded emulsion polymerization. Journal of Applied Polymer Science, **80**, 2752–2758 (2001).
DOI: 10.1002/app.1390

[12] Zhang T., Xi K., Chen H., Yu X.: Synthesis and properties of self-crosslinkable polyurethane-urea with silsesquioxane formation. Journal of Applied Polymer Science, **91**, 190–195 (2004).
DOI: 10.1002/app.13212

[13] Kong X. Z., Kan C. Y., Yuan Q.: Preparation of polyacrylate-polysiloxane core-shell latex particles. Polymers for Advanced Technologies, **7**, 888–890 (1996).
DOI: 10.1002/(SICI)1099-1581(199612)7:12<888::AID-PAT598>3.0.CO;2-5

[14] Kan C. Y., Kong X. Z., Yuan Q., Liu D. S.: Morphological prediction and its application to the synthesis of polyacrylate/polysiloxane core/shell latex particles. Journal of Applied Polymer Science, **80**, 2251–2258 (2001).
DOI: 10.1002/app.1329

[15] Cao S. S., Liu B. L., Deng X. B., Luo R., Chen H. L.: A novel approach for the preparation of acrylate-siloxane particles with core-shell structure. Polymer International, **56**, 357–363 (2007).
DOI: 10.1002/pi.2149

[16] Zou M. X., Zhang Z. C., He W. D., Ge X. W., Fan F.: Preparation and characterization of core-shell polystyrene-polydimethylsiloxane particles by seeded polymerization. Polymer International, **53**, 1033–1039 (2004).
DOI: 10.1002/pi.1470

[17] Xin L., Zhong X.: Preparation and characterization of micron-sized polystyrene/polysiloxane core/shell particles. Colloid and Polymer Science, **284**, 1062–1066 (2006).
DOI: 10.1007/s00396-006-1482-y

[18] Dreher W. R., Jarret W. L., Urban M. W.: Stable non-spherical fluorine-containing colloidal dispersions: Synthesis and film formation. Macromolecules, **38**, 2205–2212 (2005).
DOI: 10.1021/ma0479161

[19] Ha J-W., Park I. J., Lee S-B., Kim D-K.: Preparation and characterization of core-shell particles containing perfluoroalkyl acrylate in the shell. Macromolecules, **35**, 6811–6818 (2002).
DOI: 10.1021/ma011692u

[20] Ha J-W., Park I. J., Lee S-B.: Hydrophobicity and sliding behavior of liquid droplets on the fluorinated latex films. Macromolecules, **38**, 736–744 (2005).
DOI: 10.1021/ma0488764

[21] Cui X. J., Zhong S. L., Gao Y., Wang H. Y.: Preparation and characterization of emulsifier-free core-shell interpenetrating polymer network-fluorinated polyacrylate latex particles. Colloids and Surfaces A: Physicochemical and Engineering Aspects, **324**, 14–21 (2008).
DOI: 10.1016/j.colsurfa.2008.03.018

[22] Soula O., Guyot A.: Styrenic surfmer in emulsion copolymerization of acrylic monomers: I. Synthesis and characterization of polymerizable surfactants. Langmuir, **15**, 7956–7962 (1999).
DOI: 10.1021/la9817009

[23] Texter J.: Reaction and synthesis in surfactants systems. Marcel Dekker, NewYork (2001).

[24] Thenoz F., Soula O., Guyot A.: Reactive surfactants in heterophase polymerization. XXV. Core-shell lattices stabilized with a mixture of maleic anionic and styrenic nonionic surfactants. Journal of Polymer Science Part A: Polymer Chemistry, **37**, 2251–2262 (1999).
DOI: 10.1002/(SICI)1099-0518(19990701)37:13<2251::AID-POLA40>3.0.CO;2-R

[25] Chen S-A., Chang H-S.: Kinetic and mechanism of emulsifier-free emulsion polymerization: Styrene/surface active ionic comonomer system. Journal of Polymer Science: Polymer Chemistry Edition, **23**, 2615–2630 (1985).
DOI: 10.1002/pol.1985.170231005

[26] Onodera S., Yamamoto S., Tamai T., Takahashi H.: Reactive emulsifiers for polymerization of vinyl compounds. Japanese Patent JP 06239908, Japan (1994).

[27] Guyot A.: Recent progress in reactive surfactants in emulsion polymerization. Macromolecular Symposia, **179**, 105–132 (2002).
DOI: 10.1002/1521-3900(200203)179:1<105::AID-MASY105>3.0.CO;2-7

[28] Schoonbrood H. A. S., Unzué M. J., Beck O-J., Asua J. M.: Reactive surfactants in heterophase polymerization. 7. Emulsion copolymerization mechanism involving three anionic polymerizable surfactants (surfmers) with styrene-butyl acrylate-acrylic acid. Macromolecules, **30**, 6024–6033 (1997).
DOI: 10.1021/ma9701447

[29] Schoonbrood H. A. S., Asua J. M.: Reactive surfactants in heterophase polymerization. 9. Optimum surfmer behavior in emulsion polymerization. Macromolecules, **30**, 6304–6041 (1997).
DOI: 10.1021/ma9701494

[30] Qin S. H., Saget J., Pyun J., Jia S. J., Kowalewski T., Matyjaszewski K.: Synthesis of block, statistical, and gradient copolymers from octadecyl (meth)acrylates using atom transfer radical polymerization. Macromolecules, **36**, 8969–8977 (2003).
DOI: 10.1021/ma0349985

[31] Antonietti M., Landfester K.: Polyreactions in miniemulsions. Progress in Polymer Science, **27**, 689–757 (2002).
DOI: 10.1016/S0079-6700(01)00051-X

[32] Quzineb K., Graillat C., Mckenna T. F.: Study of compartmentalization in the polymerization of miniemulsions of styrene and butyl methacrylate. Journal of Applied Polymer Science, **91**, 115–121 (2004).
DOI: 10.1002/app.13181

Dehydration of an azeotrope of ethanol/water by sodium carboxymethylcellulose membranes cross-linked with organic or inorganic cross-linker

T. Uragami, D. Wakita, T. Miyata*

Department of Chemistry and Materials Engineering, High Technology Research Center, Kansai University, Suita, Osaka 564-8680, Japan

Abstract. To control the swelling of sodium carboxymethylcellulose (CMCNa) membranes, mixtures of CMCNa and glutaraldehyde (GA) and mixtures of CMCNa as an organic component and tetraethoxysilane (TEOS) as an inorganic component were prepared, and CMCNa/GA cross-linked membranes and CMCNa/TEOS hybrid membranes were formed. In the separation of an ethanol/water azeotrope by pervaporation (PV), the effects of the GA or TEOS content on the water/ethanol selectivity and permeability of these CMCNa/GA cross-linked and CMCNa/TEOS hybrid membranes were investigated. Cross-linked and hybrid membranes containing up to 10 wt% GA or 10 wt% TEOS exhibited higher water/ethanol selectivity than CMCNa membrane without any cross-linker. This resulted from both increased density and depressed swelling of the membranes by the formation of a cross-linked structure. The relationship between the structure of the CMCNa/GA cross-linked membranes and CMCNa/TEOS hybrid membranes and their permeation and separation characteristics for an ethanol/water azeotrope during PV is discussed in detail.

Keywords: biopolymers, biocomposite, polymer membranes, bio-ethanol, dehydration

1. Introduction

An aqueous bio-ethanol solution can be produced by fermentation of biomass resources such as dregs of sugar corn, stems of corn and so on, separation and concentration of an aqueous ethanol solution are actively noticed from the viewpoint of a new energy source instead of limited petroleum resource. In general, aqueous alcohol solutions are concentrated by distillation, but an azeotrope (96.5 wt% ethanol) cannot be further separated by distillation. In particular, pervaporation (PV) is a promising technique for separation of azeotropes [1, 2] such as an aqueous solution of 96.5 wt% ethanol, and close boiling point mixtures [3, 4] through polymer membranes. In PV separation, membrane performance is highly dependent upon the physical and

chemical structures of the membrane. Therefore, carefully designing the membrane structure is required to develop membranes with high selectivity and permeability. We have studied several kinds of cross-linked polymer membranes and organic-inorganic hybrid membranes to separate aqueous ethanol solutions during PV. For example, chitosan membranes cross-linked with glutaraldehyde [5], quaternized chitosan membranes cross-linked with glutaraldehyde [6], ethylenglycoldiglycidylether [7] and poly(ethylene oxydiglycolic acid) [8], poly(vinyl alcohol) and tetraethoxysilane (TEOS) [9], poly(vinyl alcohol-*co*-acrylic acid) and TEOS [10], and quaternized chitosan and TEOS [11] hybrid membranes prepared by sol-gel reaction all showed high water/ethanol selectivity for an

---

azeotrope of ethanol/water because their membrane swelling could be effectively controlled by cross-linking or hybridization.

In this study, sodium carboxymethylcellulose (CMCNa) was selected as a membrane material because CMCNa can be easily formed into fine membrane. In general, CMCNa has been applied as sizing in paper fabrication, as emulsion stabilizer, in water-borne paints and so on. We prepared sodium carboxymethylcellulose (CMCNa) membranes cross-linked with glutaraldehyde (GA) and novel organic-inorganic hybrid membranes by the sol-gel reaction between CMCNa as an organic component and tetraethoxysilane (TEOS) as an inorganic component in order to reduce the swelling of the CMCNa membranes. Furthermore, the permeation and separation characteristics of an azeotrope of ethanol/water through the CMCNa/GA cross-linkd membranes and the CMCNa/TEOS hybrid membranes during PV are discussed as a function of the GA or TEOS content. Recently, organic-inorganic hybrid materials are recognized as significant composite materials with both the functionality of an organic compound and with the strength of an inorganic compound. Therefore, in this study we call CMCNa/TEOS cross-linked membranes as CMCNa/TEOS hybrid membranes.

2. Materials and methods
2.1. Materials

Sodium carboxymethylcellulose (CMCNa), whose degree of sodium carboxymethylation is 0.91 purchased from Tokyo Kasei Industry Co. Ltd., Japan. GA and trifluoroacetic acid anhydride were supplied by Wako Chemical Industry Co. Ltd., Japan. TEOS was supplied by Shinetsu Chemical Industry Co. Ltd., Japan. All other reagents and solvents used in this study were supplied by commercial sources.

2.2. Preparation of CMCNa membrane, CMCNa/GA cross-linked membranes and CMCNa/TEOS hybrid membranes

The CMCNa membranes were prepared by pouring 3 wt% CMCNa in 0.01 M HCl onto a glass plate treated with silicon, allowing water to evaporate at 50°C for 10 h in an oven, and then drying under reduced pressure. The CMCNa/GA cross-linked and CMCNa/TEOS hybrid membranes were prepared by pouring 3 wt% CMCNa in 0.01 M HCl with a desired amount of GA as an organic cross-linker or a desired amount of TEOS as an inorganic cross-linker onto a glass plate treated with silicon, allowing water to evaporate at 50°C for 10 h in an oven, and then drying under reduced pressure. The resulting CMCNa membranes, CMCNa/GA cross-linked membranes and CMCNa/TEOS hybrid membranes were kept in a desiccator at room temperature *in vacuo*.

2.3. PV apparatus and measurements

The PV cell and PV apparatus have been described in a previous paper [12]. The effective membrane area was about 13.8 cm^2. The PV experiments were carried out under the following conditions: permeation temperature, 40°C; and pressure of the permeate side, 1.33 Pa. The feed solution, an aqueous solution of 96.5 wt% ethanol, was circulated between the PV cell and the feed tank to maintain a constant concentration of feed solution in the PV cell. The permeation rate [kg/m^2·h] for an azeotrope of ethanol/water during PV was determined from the weight [kg] of permeate collected in a cold trap, the permeation time [h] and the effective membrane area [m^2]. The results of the permeation for an azeotrope of ethanol/water by PV were reproducible, and the errors inherent in these permeation measurements ranged within a few percent of the permeation rates through the membranes. The permeation results in this study were determined after steady-state flux.

The ethanol concentration in the feed and permeate was determined by means of a gas chromatograph (Shimadzu GC-14A, Japan) using a flame ionization detector (FID) and a capillary column (Shimadzu Co. Ltd: PorapacQ, Japan) heated to 180°C. The separation factor, $\alpha_{sep.H_2O/EtOH}$, was calculated from Equation (1):

$$\alpha_{sep.H_2O/EtOH} = \frac{P_{H_2O} / P_{EtOH}}{F_{H_2O} / F_{EtOH}} \tag{1}$$

where F_{EtOH} and F_{H_2O} are the weight fractions of ethanol and water in the feed solution, and P_{EtOH} and P_{H_2O} are those in the permeate, respectively.

2.4. Composition of solution absorbed into CMCNa/GA cross-linked membranes and CMCNa/TEOS hybrid membranes

The CMCNa/GA cross-linked and CMCNa/TEOS hybrid membranes were dried completely under reduced pressure at room temperature and weighed. The dried membranes were immersed into an azeotropic mixture of ethanol/water in a sealed vessel at 40°C until equilibrium was reached. A large amount of the swollen CMCNa/GA cross-linked and CMCNa/TEOS hybrid membranes was placed in a container as reported in a previous paper [13]. The system was evacuated, and the container with the swollen membranes was then heated. The solution sorbed into the swollen membranes was completely desorbed under reduced pressure, and was collected in a U-tube cooled with liquid nitrogen. The composition of the solutions sorbed into the CMCNa/GA cross-linked and CMCNa/TEOS hybrid membranes was then determined by measuring the ethanol concentration in the collected solution by gas chromatography (Shimadzu GC-14A). The ethanol/water composition in the CMCNa/GA cross-linked and CMCNa/TEOS hybrid membranes versus that in the feed solution yielded the sorption selectivity, $\alpha_{sorp.H_2O/EtOH}$, as expressed in Equation (2):

$$\alpha_{sorp.H_2O/EtOH} = \frac{M_{H_2O} / M_{EtOH}}{F_{H_2O} / F_{EtOH}} \qquad (2)$$

where F_{H_2O} and F_{EtOH} are the weight fractions of water and ethanol in the feed solution, and M_{H_2O} and M_{EtOH} are those sorbed into the membrane, respectively.

2.5. Degree of swelling

The CMCNa and CMCNa/GA cross-linked and CMCNa/TEOS hybrid membranes were completely dried under reduced pressure at 40°C and weighed. These dried membranes were immersed in an ethanol/water azeotrope (96.5 wt% ethanol) in a sealed vessel at 40°C until equilibrium was reached. The membranes were removed from the vessel, wiped quickly with filter paper, and weighed. The degree of swelling of the membrane (DS) was determined from Equation (3):

$$DS = \frac{W_s}{W_d} \qquad (3)$$

where W_d and W_s are the weights of the dried membrane and swollen membrane in the feed, respectively.

2.6. Measurement of the contact angle

The contact angle for methylene iodide on the surface of the CMCNa/GA cross-linked and CMCNa/TEOS hybrid membranes was measured by a contact angle meter (Dropmaster Kyouwa Sci. Co. Ltd.) at 25°C. The contact angle, θ, was calculated from Equation (4) [14]:

$$\theta = \cos^{-1}\left(\frac{\cos\theta_a + \cos\theta_r}{2}\right) \qquad (4)$$

where θ_a and θ_r are the advancing contact angle and the receding contact angle, respectively.

2.7. X-ray photoelectron spectroscopy (XPS) measurements

To characterize the surfaces of the CMCNa membrane, the CMCNa/GA cross-linked and CMCNa/TEOS hybrid membranes, the hydroxyl groups of their surfaces were fluorinated by trifluoroacetic acid anhydride as shown by Equation (5):

$$\begin{array}{c} \quad\;\; O \quad\;\; O \\ \quad\;\; \| \quad\;\; \| \\ R\text{–}OH + F_3C\text{–}C\text{–}O\text{–}C\text{–}CF_3 \rightarrow \\[4pt] \quad\;\; O \qquad\qquad\;\; O \\ \quad\;\; \| \qquad\qquad\;\; \| \\ R\text{–}O\text{–}C\text{–}CF_3 + HO\text{–}C\text{–}CF_3 \qquad (5) \end{array}$$
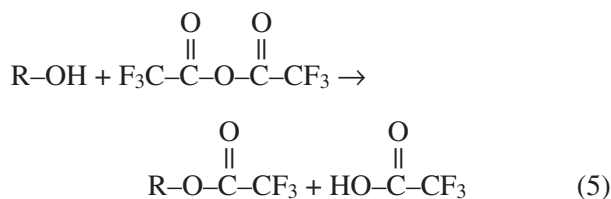
The fluorination was carried out as follows. Specimens of these membranes (5 mm×5 mm) were immersed in a mixture of benzene (20 ml), pyridine (4 ml) and trifluoroacetic acid anhydride (4 ml) for 1.5 h at room temperature, and the immersed specimens were washed with benzene repeatedly. Next, they were placed in a Soxhlet extractor with diethylether for 12 h to completely remove the trifluoroacetic acid anhydride and trifluoroacetic acid, and then dried in a desiccator under reduced pressure at room temperature.

The fluorinated surfaces of these membranes were characterized with an X-ray photoelectron spectroscope (XPS) (Shimadzu, ESCA-3400, Japan). The typical operating conditions were as follows: $CuK_{\alpha \text{ radiation}}$ of 15 kV and 10 mA. The pressure in the instrument chamber was less than $1.0 \cdot 10^{-6}$ Pa. No radiation damage was observed during the data collection time.

The atomic compositions on the surface of the CMCNa/GA cross-linked and CMCNa/TEOS hybrid membranes were determined by Equations (6) and (7):

$$CMCNa / (CMCNa+TEOS) = F / (F+Si) \qquad (6)$$

$$CMCNa / (CMCNa+GA) = F / (F+ O) \qquad (7)$$

where F, Si and O are the fractions of each element on the surface of the CMCNa/GA membranes and CMCNa/TEOS membranes.

2.8. Transmission electron micrographs (TEM)

The CMCNa/GA cross-linked and CMCNa/TEOS hybrid membranes were embedded in epoxy resin and sliced into thin films (thickness ≈ 50 nm) with a microtome (Leica; Reichert Ultracut E). The structure of the membranes was observed by a transmission electron microscope (TEM) (JEOL JEM-120L, Japan) at an accelerating voltage of 80 kV.

3. Results and discussion

3.1. Effect of the cross-linker content on the permeation and separation characteristics

Figure 1 shows the effects of the cross-linker content on the permeation rate and separation factor for an azeotrope of ethanol/water through the CMCNa/GA cross-linked and CMCNa/TEOS hybrid membranes during PV. As can be seen from Figure 1, the separation factors of all CMCNa/GA cross-linked and CMCNa/TEOS hybrid membranes were higher than those of the neat CMCNa membrane. These results support the contention that all membranes had water/ethanol selectivity. The separation factors of the CMCNa/TEOS hybrid membranes were higher than those of CMCNa/GA cross-linked membranes. Furthermore, in both CMCNa/GA cross-linked and CMCNa/TEOS
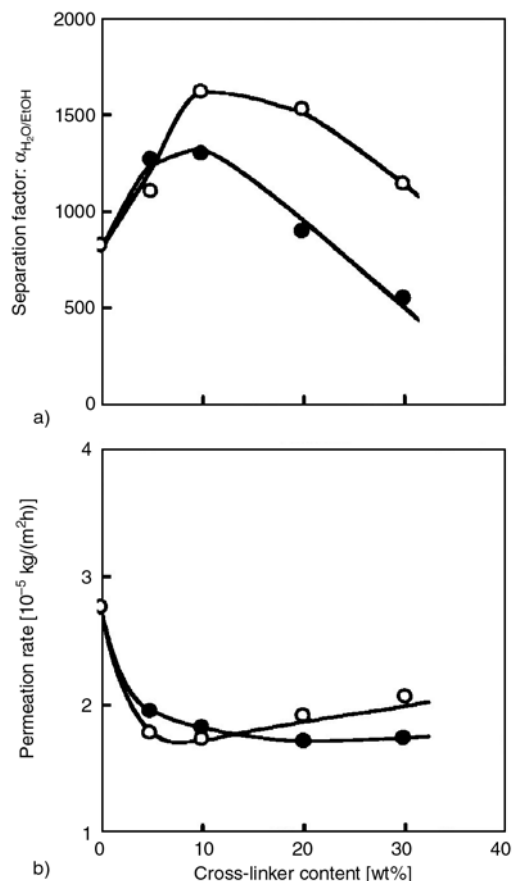
Figure 1. Effects of the GA or TEOS content on the permeation rate and separation factor for an azeotrope of ethanol/water through CMCNa/GA cross-linked membranes (●) or CMCNa/TEOS hybrid membranes (○) during PV at 40°C

hybrid membranes, the membranes cross-linked with 10 wt% of cross-linker showed the highest separation factors. On the other hand, one can understand that the permeation rates of both CMCNa/TEOS hybrid and CMCNa/GA cross-linked membranes decreased until 10 wt% of cross-linker content, but above this content, the dependency of permeation rate on the cross-linker content significantly differ. Thus, the permeation rate in the CMCNa/TEOS membrane increased but that in the CMCNa/GA membrane decreased slightly.

3.2. Chemical structure of CMCNa/GA cross-linked membranes and CMCNa/TEOS hybrid membranes

In general, the permeation and separation characteristics of these membranes are significantly governed by the chemical and physical structure of the membrane. Thus, it is known that the chemical

structure influences the solubility of the permeants into the membrane and the physical structure affects the diffusivity of the permeants through the membrane. Therefore, we analyzed the chemical structure of the membranes by the measuring the composition of solution in the membrane, the contact angle of the membrane surface and XPS, and the physical structure by the measuring the membrane density, and the degree of swelling of the membranes, and by TEM observation to elucidate their permeation and separation characteristics, as shown in Figure 1.
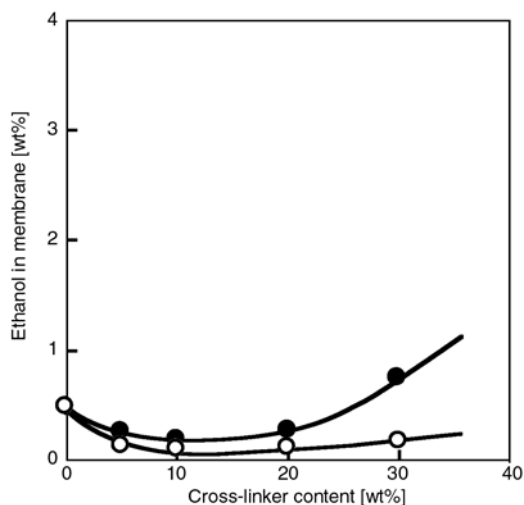
Figure 2. Effect of the cross-linker content on the ethanol concentration in the CMCNa/GA cross-linked membranes (●) and CMCNa/TEOS hybrid membranes (o) immersed in an aqueous solution of 96.5 wt% ethanol at 40°C
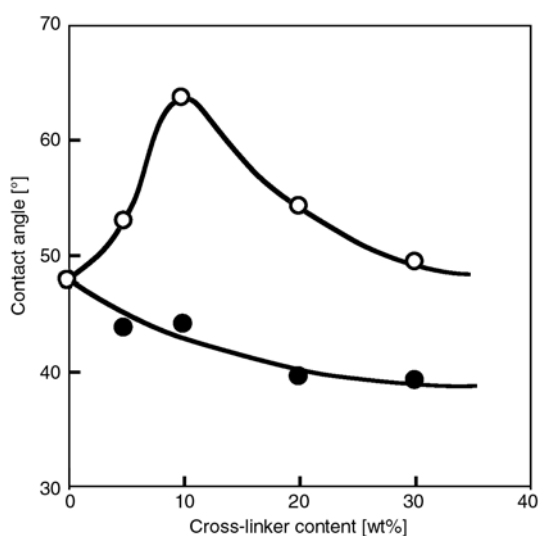
Figure 3. Contact angle for methylene iodide on the surface of CMCNa/GA cross-linked membranes (●) and CMCNa/TEOS hybrid membranes (o) as a function of the cross-linker content

In Figures 2 and 3, the ethanol concentration sorbed into the membrane immersed in an azeotrope of ethanol/water and the contact angle of the membrane surface for methylene iodide as a function of the cross-linker content are shown. As can be seen from Figure 2, the ethanol concentration sorbed into the membrane for both the CMCNa/GA cross-linked and CMCNa/TEOS hybrid membranes decreased slightly with increasing content up to 10 wt% of GA or TEOS, whereas the ethanol concentration in the CMCNa/TEOS membrane increased faintly, and the ethanol concentration in the CMCNA/GA membrane increased more than 10 wt% of cross-linker content.

On the other hand, the sorbed ethanol concentration for the CMCNa/TEOS hybrid membranes was lower than that of the CMCNa/GA cross-linked membranes over the whole range cross-linker contents. The higher separation factors for the CMCNa/TEOS hybrid membranes in Figure 1 are dependent on this result.

In Figure 3, the increase or decrease in the contact angle for methylene iodide, which is a hydrophobic solvent, suggests that the membrane surface became more hydrophilic or hydrophobic with an increase in the cross-linker content, respectively. The contact angles of the CMCNa/TEOS hybrid membranes were higher than those of the CMCNa/GA cross-linked membranes. This result suggests that the former membranes are more hydrophilic than the latter. In the CMCNa/TEOS hybrid membranes, the contact angle at 10 wt% of TEOS showed a maximum, and all contact angles were higher than that of the CMCNa membrane. These results suggest that the CMCNa/TEOS hybrid membranes are more hydrophilic than CMCNa membranes without TEOS. The contact angles of the CMCNa/GA cross-linked membranes decreased with an increasing GA content, and were lower than that of the membrane without GA. This suggests that the CMCNa/GA cross-linked membranes are more hydrophobic than membranes without GA. The higher hydrophilicity of the CMCNa/TEOS hybrid membranes could be attributed to the fact that some silanol groups from the four silanol groups formed from TEOS form the hydrogen and covalent bonds by reacting with the hydroxyl groups in CMCNa and remained silanol groups from TEOS can be introduced into the CMCNa/TEOS membrane, and consequently hydrophilic silanol groups in CMCNa/

TEOS membrane increase, and thus the higher hydrophobicity of the CMCNa/GA cross-linked membranes could be due to the fact that the hydroxyl groups in the CMCNa molecule can be consumed by the condensation reaction between the aldehyde group in the GA molecule and the hydroxyl group in the CMCNa molecule.

3.3. XPS measurements of the membranes

To determine the chemical structure of the surface of the CMCNa/GA cross-linked and CMCNa/TEOS hybrid membranes in more detail, the hydroxyl groups on the surface of cross-linked and hybrid membranes were labeled by trifluoroacetic acid anhydride as per Equation (5).

In Figures 4 and 5, the XPS spectra of the fluorinated surfaces of CMCNa/GA cross-linked and CMCNa/TEOS hybrid membranes are shown, respectively. In Figure 4, with increasing GA content, the peak intensity assigned to the F atom at 690 eV decreased, whereas the peak intensity due to the O atom at about 532 eV increased. On the other hand, as can be seen in Figure 5, the peak intensity assigned to the Si atom at 105 eV increased and the F atom at 690 eV decreased slightly upon introducing TEOS into the CMCNa membrane. In
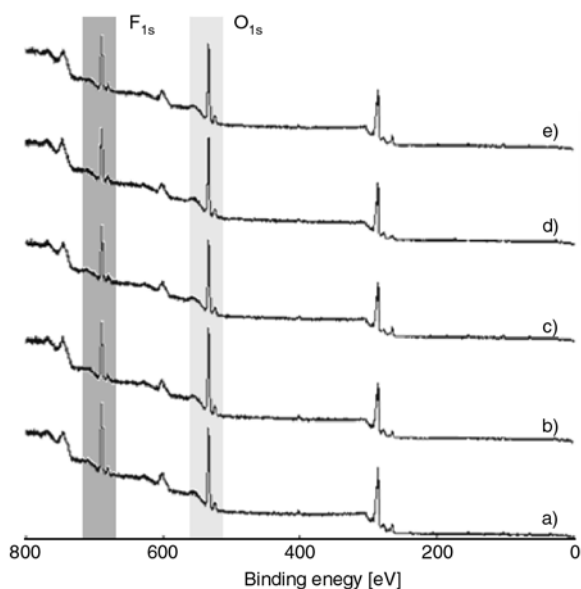
Figure 5. XPS spectra of (a) the CMCNa membrane, (b) a TEOS content of 5 wt%, (c) a TEOS content of 10 wt%, (d) a TEOS content of 20 wt% and (e) a TEOS content of 30 wt% in the CMCNa/TEOS hybrid membranes. The surfaces of these membranes were treated with trifluoroacetic acid anhydride

the spectrum (c) of the CMCNa/TEOS hybrid membrane with a TEOS content of 10 wt%, however, the peak intensity of the F atom increased but that of the Si atom decreased. Above 10 wt% of TEOS content, the peak intensity at the F atom decreased and that of the Si atom increased. The results from Figures 4 and 5 support the results of the contact angle measurements in Figure 3. Thus, it is found that the networks of CMCNa/GA cross-linked and CMCNa/TEOS hybrid membranes and the amount of the hydroxyl and silanol groups on the surface of these membranes were significantly influenced by the GA or TEOS content.

In Figure 6, the effects of the cross-linker content on the atomic compositions on the surface of the CMCNa/GA cross-linked and CMCNa/TESO hybrid membranes are shown, respectively. With increasing GA content, the amount of F atoms decreased because of the decrease in the hydroxyl group based on the condensation reaction between the hydroxyl groups in the CMCNa molecule and the aldehyde groups in the GA molecule. In Figure 6, the introduction of a small amount of TEOS into the CMCNa accelerated the reactions between the hydroxyl groups and the silanol groups formed due to the hydrolysis of TEOS and the amount of

Figure 4. XPS spectra of (a) the CMCNa membrane, (b) a GA content of 5 wt%, (c) a GA content of 10 wt%, (d) a GA content of 20 wt% and (e) a GA content of 30 wt% in the CMCNa/GA cross-linked membranes. The surfaces of these membranes were treated with trifluoroacetic acid anhydride
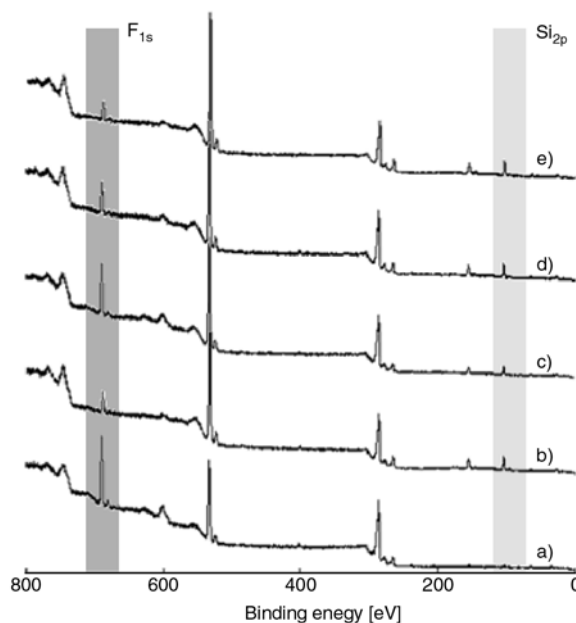
Figure 6. Effect of the cross-linker content on the atomic composition on the surface of CMCNa/GA cross-linked membranes (●) and CMCNa/TEOS hybrid membranes (○)

hydroxyl groups in the CMCNa molecule decreased and consequently the amount of F atoms decreased. At 10 wt% of TEOS content, the amount of F atoms increased due to the increase in the silanol group during the sol-gel process. Above 10 wt% of TEOS content, since the number of hydroxyl groups were decreased by excess condensation reactions, the amount of F atom decreased. These findings also support those observed in the contact angle measurements.

3.4. Structure of CMCNa/TEOS hybrid membranes

Based on the above results, the structure of CMCNa/TEOS hybrid membranes is illustrated in Figure 7, showing the process polycondensation reaction of TEOS [15]. In the first step of the process of preparing the CMCNa/TEOS hybrid membranes, the silanol groups were formed by hydrolyzing TEOS in the presence of an acid catalyst (A). The resulting silanol groups yielded siloxane bonds due to the dehydration or dealcoholysis

Figure 7. Hydrolysis and condensation scheme for TEOS

Figure 8. Illustration of the interaction between CMCNa and TEOS

reactions with other silanol groups or ethoxy groups during the membrane drying process (B). These reactions led to cohesive bodies between siloxane groups in the membrane. Since the siloxane groups were dispersed in the membrane, the silanol groups in the siloxane and the hydroxyl groups in CMCNa formed hydrogen and covalent bonds, which are the cross-linking points, as illustrated in Figure 8.

However, the dehydration and dealcoholysis reactions occurred predominantly rather than the formation of hydrogen and covalent bonds. Thus, a rough cohesive structure of TEOS was formed, and hence a membrane with a more open structure was produced, leading to a decrease in the water/ethanol selectivity.

3.5. Physical structure of CMCNa/GA cross-linked and CMCNa/TEOS hybrid membranes

In Figure 9, the degree of swelling of the CMCNa/GA cross-linked and CMCNa/TEOS hybrid membranes is shown as a function of the GA or TEOS content. The degree of swelling of both membranes decreased with an increase in the GA or TEOS content. The swelling of the CMCNa/TEOS hybrid membranes was smaller than that of the CMCNa/GA cross-linked membranes. These results can be supported by the results of the membrane density.
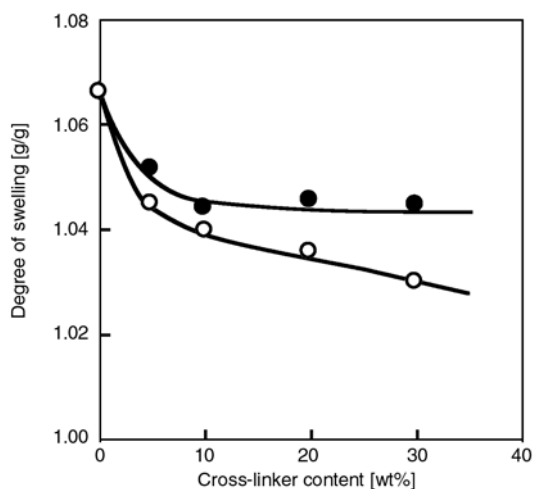
Figure 9. Effect of the cross-linker content on the degree of swelling of CMCNa/GA cross-linked membranes (●) and CMCNa/TEOS hybrid membranes (○)

3.6. Permselectivity mechanism of cross-linked and hybrid membranes

In the solution-diffusion model [16, 17] differences in the solubility of the permeants in the membranes and differences in the diffusivity of the permeants in the polymer membranes are very significantly related to their permselectivity [18]. It is very important to determine the sorption selectivity and diffusion selectivity to elucidate the separation mechanism of an azeotrope of ethanol/water through CMCNa/GA cross-linked and MCNa/TEOS hybrid membranes. Thus, in order to discuss the water/ethanol selectivity of an azeotrope of ethanol/water through CMCNa/GA cross-linked and CMCNa/TEOS hybrid membranes from the viewpoint of the solution-diffusion mechanism, both the sorption selectivity and the diffusion selectivity must be determined. The sorption selectivity, $\alpha_{sorp.H_2O/EtOH}$, was determined from Equation (2), whereas the diffusion selectivity, $\alpha_{diff.H_2O/EtOH}$, could be calculated from Equation (8) using Equations (1) and (2):

$$\alpha_{diff.H_2O/EtOH} = \frac{\alpha_{sep.H_2O/EtOH}}{\alpha_{sorp.H_2O/EtOH}} \qquad (8)$$

In Figure 10, the separation factor, the sorption selectivity and the diffusion selectivity for an azeotrope of ethanol/water through CMCNa/GA cross-linked or CMCNa/TEOS hybrid membranes are shown as a function of the GA or TEOS content. The sorption selectivities of all membranes
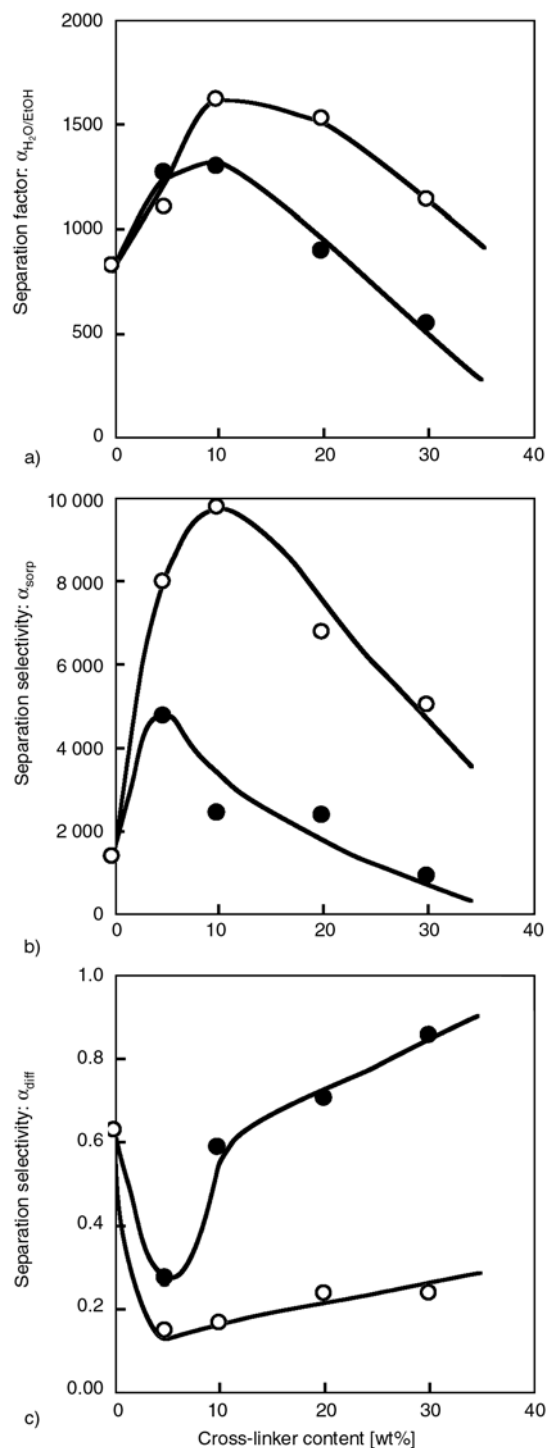

Figure 10. Effects of the cross-linker content on the separation factor, the sorption selectivity and the diffusin selectivity for an azeotrope of ethanol/water through CMCNa/GA cross-linked membranes (●) and CMCNa/TEOS hybrid membranes (○) during PV at 40°C

with various GA or TEOS contents were greater than their diffusion selectivities. This observation suggests that the dehydration process from an aqueous solution of 96.5 wt% ethanol using CMCNa/GA

cross-linked and CMCNa/TEOS hybrid membranes is mainly governed by the sorption process. The fact that water was preferentially absorbed into these membranes rather than ethanol also supports this conclusion. Furthermore, the sorption selectivities of the CMCNa/TEOS hybrid membranes were higher than those of the CMCNa/GA cross-linked membranes. These results are supported by the composition absorbed into the membrane as shown in Figure 2. On the other hand, the diffusion selectivities of the former membranes were smaller than those of the latter membranes. This is due to the fact that with increasing GA or TEOS content, the degree of swelling of the membrane decreased as shown in Figure 9. The increase in the water permselectivity with increasing GA or TEOS content was mainly due to an increase in the solubility of water in the CMCNa/GA cross-linked and CMCNa/TEOS hybrid membranes.

3.7. TEM images of cross-linked and hybrid membranes

Figure 11 shows TEM images of the CMCNa membrane, the CMCNa/GA cross-linked membranes and CMCNa/TEOS hybrid membranes with 10 and 30 wt% of GA or TEOS content. The black portion in these images is dependent on the Si atom in TEOS. As can be seen from these TEM images, the structure of the CMCNa membrane was homogeneous but in the CMCNa/TEOS hybrid membranes, a phase separated structure was observed, especially in the hybrid membrane with 30 wt% of TEOS content which showed a heterogeneously dispersed cohesion of TEOS. On the other hand, in the CMCNa/GA cross-linked membranes such a phase separated structure was not observed.

Based on the above results, the hypothetical structure of the CMCNa/TEOS hybrid membranes is shown in Figure 12. In the CMCNa/TEOS hybrid
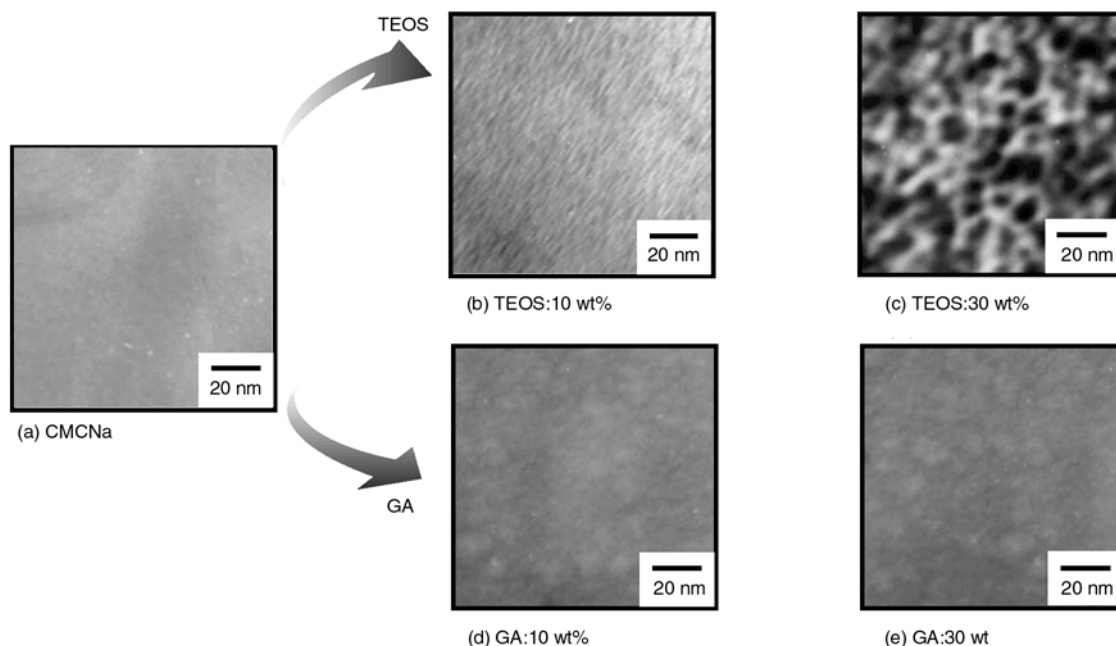

Figure 11. TEM images of : (a) the CMCNa membrane, (b) with a TEOS content of 10 wt%, (c) with a TEOS content of 30 wt% in CMCNa/TEOS hybrid membranes, (d) with a GA content of 10 wt%, (e) with a GA content of 30 wt% in CMCNa/GA cross-linked membrane
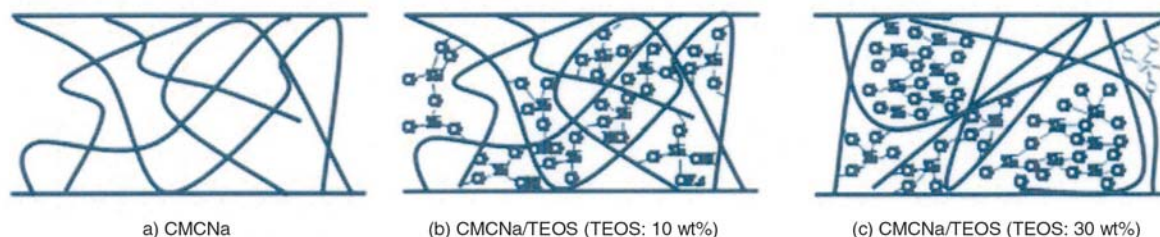

Figure 12. Change in the cross-linked structure of CMCNa/TEOS hybrid membranes

membranes containing 10 wt% TEOS or less, the cross-linked structure was formed by smooth reactions between the CMCNa and TEOS and between the TEOS molecules. Consequently, although the permeation rate decreased with increasing TEOS content, the water/ethanol selectivity was improved remarkably, as shown in Figure 1. However, in the CMCNa/TEOS hybrid membrane containing excess TEOS (>10 wt%) the polycondensation reaction between the TEOS molecules proceeds preferentially. Therefore, the cross-linking reaction between CMCNa and TEOS was less favored. The resulting cohesion in the TEOS domains prevents the hydrogen bonds between the CMCNa molecules. These results influence the diffusion path and consequently the permeation rates and the selectivity. Therefore, an increase in the permeation rate and a decrease in the water/ethanol selectivity were observed.

4. Conclusions

Both CMCNa/GA cross-linked and CMCNa/TEOS hybrid membranes showed high water/ethanol selectivity. Consequently, it was found that the introduction of the cross-linking structure into CMCNa molecule was very effective.The water/ethanol selectivity of the CMCNa/TEOS hybrid membranes was higher than that of the CMCNa/GA cross-linked membranes. When a suitable amount of TEOS was added to CMCNa, the TEOS was homogeneously dispersed in the membrane, and the most suitable cross-linked structure was formed. Consequently, the best water/ethanol selectivity was obtained. In comparing of the role of TEOS and GA as cross-linkers, since TEOS gave higher cross-link points than GA, a denser cross-linked structure was formed, the swelling of the membrane was effectively controlled. Consequently, the CMCNa/TEOS hybrid membranes showed higher water/ethanol selectivity. The abrupt changes in some properties of CMC membranes cross-linked with 10 wt% of TEOS can be explained as follows: in the sol-gel process the CMC membranes with 10 wt% of TEOS is homogeneous with a lot of hydroxyl groups and consequently chemical and physical structures of this membrane are very fine. In this study, we demonstrated that membranes with high water/ethanol selectivity can be designed by the hybridization of CMCNa as an organic component and TEOS as an inorganic component using the sol-gel reaction, and CMCNa offers potential for the selective separation of an azeotrope of ethanol/water.

References

[1] Baker R. W.: Pervaporation. in 'Membrane separation system, recent developments and future directions' (eds.: Baker R. W., Cusssler E. L., Eykamp W., Koros W. J., Riley R. L., Strathmann H.) Noyes Data Corporation, Park Ridge, USA, 151–187 (1991).

[2] Psaume R., Aptel Ph., Aurell Y., Mora C. J., Bersillon J. L.: Pervaporation: Importance of concentration polarization in the extraction of trace organics from water. Journal of Membrane Science, **36**, 373–384 (1988).
DOI: 10.1016/0376-7388(88)80030-9

[3] Blume I., Wijmans J. G., Baker R. W.: The separation of dissolved organics from water by pervaporation. Journal of Membrane Science, **49**, 253–286 (1990).
DOI: 10.1016/S0376-7388(00)80643-2

[4] Fang Y., Pham V. A., Matuura T., Santerre J. P., Narbaitz R. M.: Effect of surface-modifying macromolecules and solvent evaporation time on the performance of polyethersulfone membranes for the separation of chloroform/water mixtures by pervaporation. Journal of Applied Polymer Science, **54**, 1937–1943 (1994).
DOI: 10.1002/app.1994.070541216

[5] Uragami T., Matsuda T., Okuno H., Miyata T.: Structure of chemically modified chitosan membranes and their characteristics of permeation and separation of aqueous ethanol solutions. Journal of Membrane Science, **88**, 243–251 (1994).
DOI: 10.1016/0376-7388(94)87010-1

[6] Uragami T., Tanaka Y., Nishida S.: Permeation and separation under high temperature and high pressure for ethanol/water vapors through cross-linked quaternized chitosan composite membranes. Desalination, **147**, 449–454 (2002).
DOI: 10.1016/S0011-9164(02)00642-2

[7] Uragami T., Takuno M., Miyata T.: Evapomeation characteristics of cross-linked quaternized chitosan membranes for the separation of an ethanol/water azeotrope. Macromolecular Chemistry and Physics, **203**, 1162–1170 (2002).
DOI: 10.1002/1521-3935(200206)203:9<1162::AID-MACP1162>3.0.CO;2-Q

[8] Uragami T., Yamamoto S., Miyata T.: Dehydration from alcohols by polyion complex cross-linked chitosan composite membranes during evapomeation. Biomacromolecules, **4**, 137–144 (2003).
DOI: 10.1021/bm025642o

[9] Uragami T., Okazaki K., Matsugi H., Miyata T.: Structure and permeation characteristics of an aqueous ethanol solution of organic-inorganic hybrid membranes composed of poly(vinyl alcohol) and tetraethoxysilane. Macromolecules, **35**, 9156–9163 (2002).
DOI: 10.1021/ma020850u

[10] Uragami T., Matsugi H., Miyata T.: Pervaporation characteristics of organic-inorganic hybrid membranes composed of poly(vinyl alcohol-*co*-acrylic acid) and tetraethoxysilane for water/ethanol separation. Macromolecules, **38**, 8440–8446 (2005).
DOI: 10.1021/ma051450k

[11] Uragami T., Katayama T., Miyata T.: Dehydration of an ethanol/water azeotrope by novel organic-inorganic hybrid membranes based on quaternized chitosan and tetraethoxysilane. Biomacromolecules, **5**, 1567–1574 (2004).
DOI: 10.1021/bm0498880

[12] Inui K., Miyata T., Uragami T.: Permeation and separation of organic liquid mixtures through liquid-crystalline polymer networks. Die Angewandte Makromolekulare Chemie, **240**, 241–250 (1996).
DOI: 10.1002/apmc.1996.052400123

[13] Uragami T., Ohshima T., Miyata T.: Removal of benzene from an aqueous solution of dilute benzene by various cross-linked poly(dimethylsiloxane) membranes during pervaporation. Macromolecules, **36**, 9430–9436 (2003).
DOI: 10.1021/ma0345753

[14] Uragami T., Tsukamoto K., Miyata T.: Pervaporation characteristic s of a benzoylchiotsan membrane for benzene/ cychlohexane mixtures. Macromolecular Chemistry and Physics, **199**, 49–54 (1998).

[15] Sakka S., Ito S., Kamiya K.: Electronic spectra of transition metal ions in gel-derived and melt-derived glasses. Journal of Non-Crystalline Solids, **71**, 311–315 (1985).
DOI: 10.1016/0022-3093(85)90301-1

[16] Binning R. C., Lee R. J., Jennings J. F., Martin E. C.: Separation of liquid mixtures by pervaporation. Industrial Engineering and Chemistry, **53**, 45–50 (1961).
DOI: 10.1021/ie50613a030

[17] Aptel P., Cuny J., Jozefonvicz J., Morel G., Neel J.: Liquid transport through membranes prepared by grafting of polar monomers onto poly(tetrafluoroethylene) films. III. Steady-state distribution in membrane during pervaporation. Journal of Applied Polymer Science, **18**, 365–378 (1974).
DOI: 10.1002/app.1974.070180205

[18] Uragami T., Meotoiwa T., Miyata T.: Effects of morphology of multicomponent polymer membranes containing calixarene on permselective removal of benzene from a dilute aqueous solution of benzene. Macromolecules, **36**, 2041–2048 (2003).
DOI: 10.1021/ma025863m

Synthesis of novel functional liquid and its application as a modifier in SBR/silica composites

Y. D. Lei[1], Z. H. Tang[1], B. C. Guo[1,2], L. X. Zhu[1], D. M. Jia[1]*

[1]Department of Polymer Materials and Engineering, South China University of Technology, Guangzhou 510640, China
[2]State Key Laboratory of Pulp and Paper Engineering, South China University of Technology, Guangzhou 510640, China

Abstract. A novel functional ionic liquid (IL), 1-methylimidazolium methacrylate (MimMa), was synthesized for modifying styrene butadiene rubber (SBR)/silica composites. MimMa was found to be readily polymerized via the initiated radical mechanism and could be analogously grafted onto rubber chains during vulcanzation. Substantial hydrogen bonding between polymerized MimMa (poly(MimMa)) and silica can facilitate the silica dispersion and improve the SBR/silica interfacial bonding. Filler networking, curing behavior, silica dispersion and mechanical performance of the modified SBR/silica composites were studied. With a low concentration of MimMa, remarkable improvements in the interfacial interactions and mechanical properties were achieved which was attributed to the improved silica dispersion and strengthened interfacial bonding induced by MimMa. A modified interphase structure was accordingly proposed and related to the mechanical performance of the modified SBR/silica composites.

Keywords: rubber, silica, ionic liquid, interface

1. Introduction

The filler dispersion and the rubber/filler interfacial bonding are two critical factors in determining the performance of the filled rubber composites. Conventionally, the surface treatments with various modifiers such as silanes have been used to improve the filler dispersion and strength the rubber/silica interfacial bonding [1–4]. Due to the high polarity of silica particles, the dispersion of silica in silane included systems and controllability of the performance are far from satisfactory. Ionic liquid (IL), a kind of fascinating molten salt with nearly zero vapor pressure and high thermal stability [5–7], has demonstrated high affinity toward various kinds of solid, such as carbon nanotubes [8–14], silica [15–17] and clays [18]. Various interactions, including cation-π interaction [8–11, 19], van der Waal forces [13], delocalized electron interaction [14] and hydrogen bonding [16, 18]

have been well acknowledged and therefore subjected to a plenty of applications [14, 16–18, 20–26]. Thanks to these interactions, ILs with specific structure can be employed as possible interfacial modifiers for various filled polymer composites. However, due to the limited compatibility toward rubber [27–29] and the environmental unfriendliness of the fluorine containing anions [30], these two factors deter the common ILs such as 1-butly-3-methylimidazole hexafluorophosphate (BmimPF$_6$) from their corresponding promising applications in modifying rubber/filler composites. Previously, we have confirmed that, via special treating methods, such as solution dispersion, mechanical grinding or microwave irradiation treatment, BmimPF$_6$ could not only influence surface properties of rubber fillers, but also improve the mechanical performance of the filled polymer materials [31–33]. However, an excess loading of

BmimPF$_6$ proved to be unacceptable because of its poor interaction toward rubber chains and its high economic cost. Consequently, designing functional ILs with special functional structure and economic rationality is of crucial importance in exploring novel interfacial modifier for rubber/filler composites.

In a recent study, protic ILs could be high efficiently fabricated and their structure ccould be easily tailored with numerous commercially available raw materials such as Bronsted acids and bases [34–38]. In our previous work, a functional group was successfully induced into the anion of IL. Through a procedure similar to the synthesis of protic ILs, 1-methylimidazolium sorbate (MimS) was synthesized and investigated as a modifier for improving silica dispersion and interfacial bonding [39]. The mechanical performance of the MimS modified styrene butadiene rubber (SBR)/silica composites were effectively improved. In the present work, another novel functional IL, 1-methylimidazolium methacrylate (MimMa), is synthesized and utilized as a modifier for the SBR/silica rubber composites. Based on the disclosed MimMa/silica interaction and the graftability of MimMa toward rubber chains, an improved interfacial structure is proposed. The performance of SBR/silica composites is studied. The vulcanization behavior, mechanical performance and the abrasion resistance are all correlated to the improved dispersion and interfacial structure induced by MimMa.

2. Experimental

2.1. Materials

N-methylimidazole, with 99% purity, was purchased from Alfa Aesar, TianJin, China. Methacrylic acid, analytical grade, was produced by Tianjin Bodi Chemical Holding Co. Ltd, China. Styrene butadiene rubber (SBR), with trade name SBR1502 (styrene content 23.5 wt%), was manufactured by Jilin Chemical Industry Company, China.

Precipitated silica, with trade name WL180, was manufactured by NanPing Jialian Chem. Ltd., China. The Brunauer-Emmett-Teller (BET) value of silica was re-determined to be 200 m^2/g by Micromeretics ASAP 2020. Other rubber additives were industrial grade and used as received.

2.2. Synthesis of MimMa

Stoichiometric N-methylimidazole was added dropwise to methacrylic acid. The reaction was kept below 20°C under stirring and lasted for 1 hour. The transparent colorless liquid product (1-methylimidazolium methacrylate, MimMa) was characterized by FTIR spectroscopy (Bruker Vertex 70 FTIR spectrometer) and ^{1}H NMR spectroscopy (Bruker AVANCE Digital NMR spectrometer, 300 MHz). ^{1}H NMR (CDCl$_3$, 300 MHz): 11.83 (s, 1H, N–H), 7.68 (s, 1H, N–CH=N), 7.08–7.09 (t, 1H, J1 = 1.20 Hz, J2 = 1.05 Hz, C=CH–N=C), 6.86–6.87 (t, 1H, J = 1.29 Hz, (CH$_3$)N–CH=C–N), 6.11–6.13 (m, 1H, *cis* –OOC–C=CH), 3.69 (s, 3H, N–CH$_3$), 1.94–1.95 (m, 3H, (CH$_3$)(–OOC)C=C). FTIR (Bruker Vertex 70, KBr) [40–43]: 3400 (N–H), 3130 (imidazole-H), 1523 (C=N), 1693 (C=O), 1630 (C=C in the anion).

2.3. Polymerizability of MimMa and its graftability toward SBR chains

Bulk polymerization of MimMa were conducted with 2,2'-azobisisobutyronitrile (AIBN) (0.5 wt%) as the initiator at 65°C for 4 hours under nitrogen protection. Grafting copolymerization of MimMa onto SBR was performed in toluene with AIBN as the initiator (SBR/MimMa/AIBN, 10/5/0.15, wt/wt/wt). The reaction was conducted at 65°C for 5 h. The crude graft product was first washed with deionized water for three times and then extracted with water on a Soxhlet extractor for 3 days. The MimMa grafted product (poly(SBR-g-MimMa)) was then obtained after vacuum drying. Poly(MimMa) and poly(SBR-g-MimMa) were verified by FTIR spectroscopy.

2.4. Interactions of MimMa and poly(MimMa) with silica

Another bulk polymerization of MimMa in the presence of silica was performed according to the procedure mentioned above. FTIR, differential scanning calorimetry (DSC; Q5000 differential scanning calorimeter, TA Instruments) and X-ray photon spectroscopy (XPS; Kratos Axis Ultra DLD) were performed to reveal the interaction

between them. In the XPS experiment, silica and MimMa/silica were tested with a monochromated Aluminum Kα source (1486.6 eV). Those XPS spectra of Si and C atoms were obtained by fine scanning with step width of 0.1 eV. The MimMa/silica (10/1, wt/wt) sample were mixed, washed with acetone, centrifuged and lastly obtained after a vacuum drying. All XPS spectra were calibrated to its reference C1s component at 285.0 eV [44]. A Gaussian function was employed to fit the curve in order to distinguish the chemical components with different chemical environments. The DSC cures on poly(MimMa) and poly(MimMa)/silica were scanned from –85 to 20°C at 10°C·min^{-1} with nitrogen as the purging gas.

2.5. Preparation of SBR/silica compounds and their characterizations

All the rubber compositions were summarized in Table 1. SBR and other additives were mixed on an open two-mill moll. The dependence of shear modulus (G') on the strain of uncured rubber compounds was measured with the strain from 0.5 to 100% at 70°C on viscoelastography rubber processing analyzer (Göttfert-Werkstoff-Prüfmaschinen GmbH, Germany). The frequency was set as 1 Hz. The curing characteristics of the rubber compounds were determined by a UR-2030 vulcameter (U-CAN, Taiwan) at 170°C. After the rubber compounds were vulcanized for vulcanization time (T_{c90}) at 170°C, tensile and tear tests of the vulcanizates were performed according to ISO 37-2005 and ISO 34-2004, respectively. The dynamic mechanical analysis (DMA) was performed on the EPLEXOR dynamic mechanical analyzer (Gabo Qualimeter Testanlagen GmbH; Ahlden, Germany). The samples were scanned from –100 to 100°C at 3°C/min. A tensile mode was adopted. Scanning electron microscopy (SEM) observation was performed on cryogenically fractured vulcanizates with a LEO 1530 VP scanning electron microscope (Leo system GmbH; Schwerte, Ger-

many). Before the observation, a thin gold was evaporated on the fractured surface. Transition electron microscopy (TEM) observations were done on ultramicrotomed slices (~200 nm) using a Philips Tecnai 12 transmission electron microscope (Eindhoven, Netherlands) with an accelerating voltage of 30 kV.

3. Results and discussion
3.1. Polymerization of MimMa and its reactivity towards SBR chains

Polymerizability of MimMa and its graftability toward SBR chains are characterized by their FTIR spectra (Figure 1). According to the spectra of poly(MimMa), the stretching of the double bound (C=C) was not found, which indicates the polymerization of MimMa happened. Also a shift of the C=O band from 1693 to 1680 cm^{-1} indicates an environmental change of the anion. In the FTIR spectrum pattern of poly(SBR-g-MimMa), the aromatic hydrogen (3020 and 3060 cm^{-1}), the CH$_2$ (2912 and 2843 cm^{-1}), the *trans* C=CH (964 cm^{-1}) and the phenyl (694 cm^{-1}) can be assigned to the SBR backbone [43, 45]. The characteristic groups of MimMa, such as C=N (1530 cm^{-1}), carbonyl (1690 cm^{-1}) and C=CH (3142 cm^{-1}) in the imida-
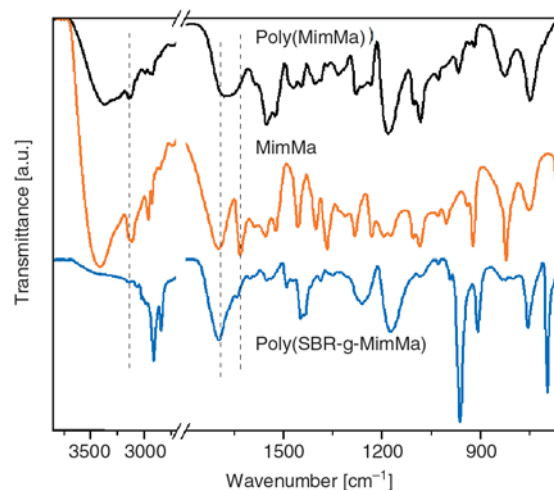

Figure 1. FTIR spectra of MimMa, poly(MimMa) and poly(SBR-g-MimMa)

Table 1. Composition of SBR/silica rubber composites [a]

Sample code	R0MimMa	R1MimMa	R2MimMa	R3MimMa	R4MimMa
SBR	100	100	100	100	100
Silica	40	40	40	40	40
MimMa	0	1	2	3	4

[a] rubber ingredients: zinc oxide 5, stearic acid 1, dicumyl peroxide (DCP) 1,2-mercaptobenzoimidazole 1.5 (all in parts per hundred parts of rubber [phr])

zolium cation, indicate the successful grafting of MimMa onto SBR chains.

3.2. MimMa/silica interactions and its influences on filler networking

As shown in the upper curve in Figure 2, the binding energies (BE) of silicon (Si) in silanol group (Si–OH) and in silicon-oxygen bond (Si–O–Si) were located at 105.0 and 103.7 eV, respectively [46]. Once silica was treated with MimMa, the adsorption peaks of Si are distinguished. The peak at 103.6 eV was related to the region where is geometrically unavailable for the Si–O–Si/MimMa interaction. The peak located at 104.0 eV was ascribed to the Si atoms in different original chemical environments. First, it was partially originated from Si–OH because the anion of MimMa, interacting with Si–OH via hydrogen bonding, could decrease the BE value of Si by strengthening the electron screening effect. Second, it was partially ascribed to the Si–O–Si bond since its BE value of Si could be increased by weakening its electron screening effect due to the hydrogen bonding between silica and the imidazolium cation.

Due to the disclosed interaction between MimMa and silica, filler networking in rubber compounds, which is usually evaluated by the Payne effect [47, 48], may be influenced a lot. According to the dependence of shear modulus (G') on strains, the discrepancy of G' ($\Delta G'$) between a small strain (~0.5%) and a large strain (~100%) can be employed to study the filler networking in the rubber matrix. As a larger extent of the network forms in the filled rubber compounds, a bigger $\Delta G'$ appears. The
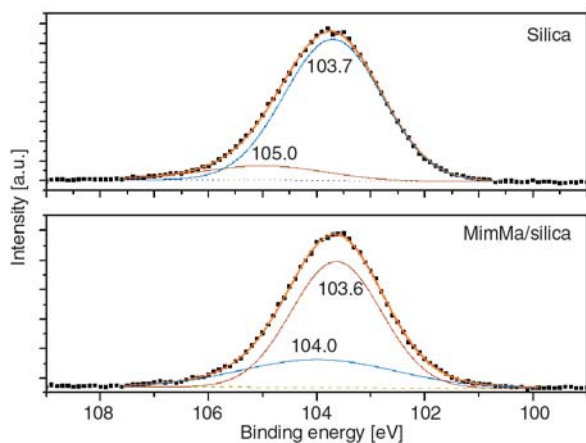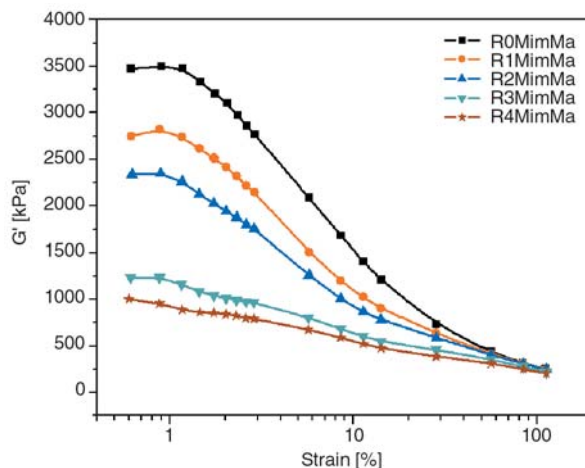

Figure 3. Strain dependence of G′ of SBR/silica compounds

dependence of G' on strain for the uncured rubber compounds is showed in Figure 3. The value of G' at low strains (<1%) is high, indicating the formation of silica networking in the rubber matrix. However, with increasing loading of MimMa, the values of G' are considerably decreased. For example, the values of G' at lower strains (<1%) is largely decreased from 3500 kPa for R0MimMa to 1000 kPa for R3MimMa. Furthermore, the values of $\Delta G'$ for the rubber compounds are effectively decreased, indicating the weakened Payne effects. Take R4MimMa for example, its values of $\Delta G'$ 800 kPa, which is only about one quarter of that value of R0Mimma (3220 kPa). The alleviated networking of silica by the addition of MimMa can be ascribed to the weakened interactions among silica particles due to the hydrogen bonding between MimMa and silica as substantiated above.

3.3. Interactions between poly(MimMa) and silica

As shown in Figure 1, abundant hydrogen bond functionalities such as carbonyl and imidazole rings are contained in poly(MimMa). Thus, it is expected that poly(MimMa) can interact with silica through special interactions. The FTIR spectra of poly(MimMa) and poly(MimMa)/silica is compared in Figure 4. Red shifts of N–H group (from 3364 to 3387 cm⁻¹) and C=O group (from 1680 to 1693 cm⁻¹) were found, while the C=C–H in the imidazolium cation and the C–O in the anion showed blue shifts from 3142 to 3122 cm⁻¹ and from 1182 to 1171 cm⁻¹, respectively. Both shifts

Figure 2. Curve fitting of XPS spectra of Si 2p in silica and poly(MimMa)/silica
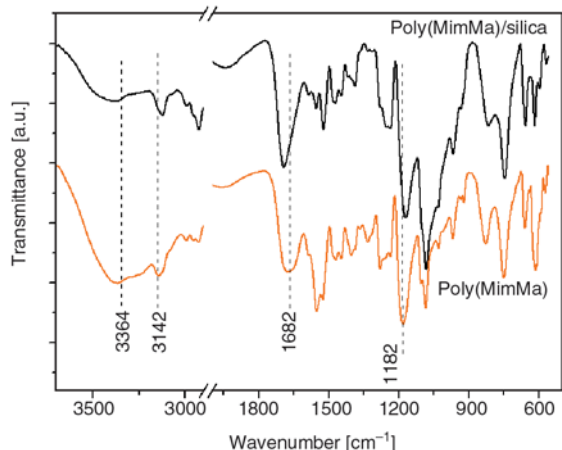
Figure 4. FTIR spectra of poly(MimMa) and poly(MimMa)/silica

strongly suggest that the strong interactions between poly(MimMa) and silica also exist. The possible interaction is partially ascribed to the hydrogen bonding between the imidazolium cation and Si–O–Si and partially ascribed to the hydrogen bonding between the anion and Si–OH groups on silica surface, which is well agreement with others' work [16].

The hydrogen bonding may be between poly (MimMa) and silica may affect the glass transition as the mobility of poly(MimMa) was restricted. The DSC curves on poly(MimMa) and poly (MimMa)/silica were presented in Figure 5. The glass transition temperature (T_g) of poly(MimMa) is located around –57°C. When about 10 wt% silica is incorporated, no visible glass transition is detected below 0°C. It indicates that the mobility of the poly(MimMa) chains is greatly restricted by the strong hydrogen bonding between poly(MimMa) and silica.
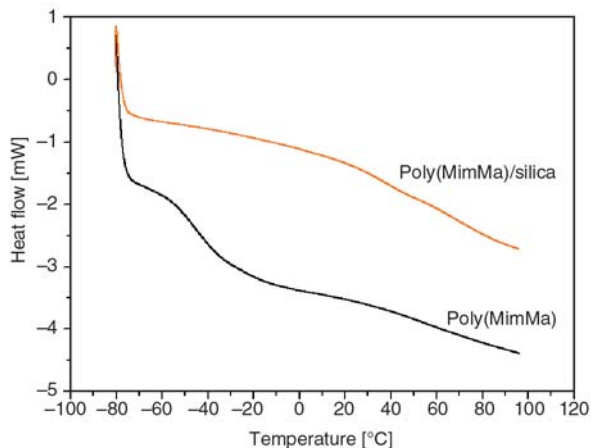
3.4. Effect of MimMa on the vulcanization behavior of SBR rubber compounds

Due to the MimMa/filler interaction and the reactivity of MimMa toward SBR which have been substantiated, the vulcanization behavior of the modified SBR/silica rubber compounds was studied. The curing curves are depicted in Figure 6. It can be seen that with higher MimMa loading, the value of the minimum torque (T_{min}) during vulcanization is gradually lowered. As indicated from the restrained filler networking in Figure 6, the effective silica volume is substantially decreased because of the weakened interaction among silica particles [49–51]. So with increasing loading of MimMa, the value of T_{min} is consistently lowered. Interestingly, the maximum torque (T_{max}) for these samples does not exhibit a simple trend. With increasing loading of MimMa, the value of T_{max} takes a maximum for R1MimMa and then gets decreased significantly. There are several factors in governing this change. First, the incorporated MimMa may cover the silica surface and suppress the DCP adsorption on silica. Second, MimMa consumes part of DCP during the vulcanization. Third, the addition of MimMa facilitates the dispersion of silica in rubber and results in lower effective filler volume [47, 52, 53]. The overall effect of MimMa depends upon the competition of these factors. When the first factor dominates, the T_{max} value will be higher. However, when the last two factors dominate, the T_{max} value will be lower. When 1 phr of MimMa is used, the consumption of DCP by MimMa and the change in silica dispersion should be limited. So the first factor dominates and higher T_{max} is observed. When the content of MimMa is
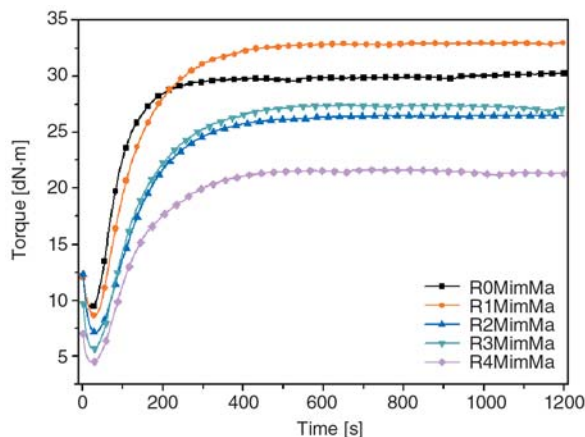

Figure 5. DSC curves for poly(MimMa) and poly(MimMa)/silica

Figure 6. Vulcanization curves of SBR/silica rubber compounds

further increased, the second and third factors cannot be ignored and consequently much lower T_{max} values are obtained.

3.5. Effect of MimMa on the silica dispersion

Silica dispersion in the rubber matrix is studied by SEM and TEM observations. For R0MimMa vulcanizate, as shown in the two left photos in Figure 7, there are a lot of agglomerates with large sizes more than 100 nm. From these two photos of R4MimMa on the right, it is clear to see that the agglomerate size is significantly decreased and the particles of silica are uniformly dispersed in the rubber matrix. Both the SEM and TEM observations reveal that the dispersion of silica in the modified vulcanizates is obviously improved. The improved filler dispersion is also attributed to the

interfacial interactions induced by the functional IL. Also, the morphology observations are well consistent with the conclusion derived from the decreased Payne effect in the uncured rubber compounds.

3.6. Mechanical performance and abrasion resistance of SBR/silica vulcanizates

The dependences of tensile strength and tear strengths on MimMa loading are revealed in Table 2. With only 4 phr of MimMa, the tensile strength is largely increased by an increment of 59% and the tear strength is enhanced by 58%. Simultaneously, the modulus (always estimated by the stress at 300%) is effectively increased by up to 80%. The hardness of the vulcanizates shows practically no variation. From Table 2, the abrasion
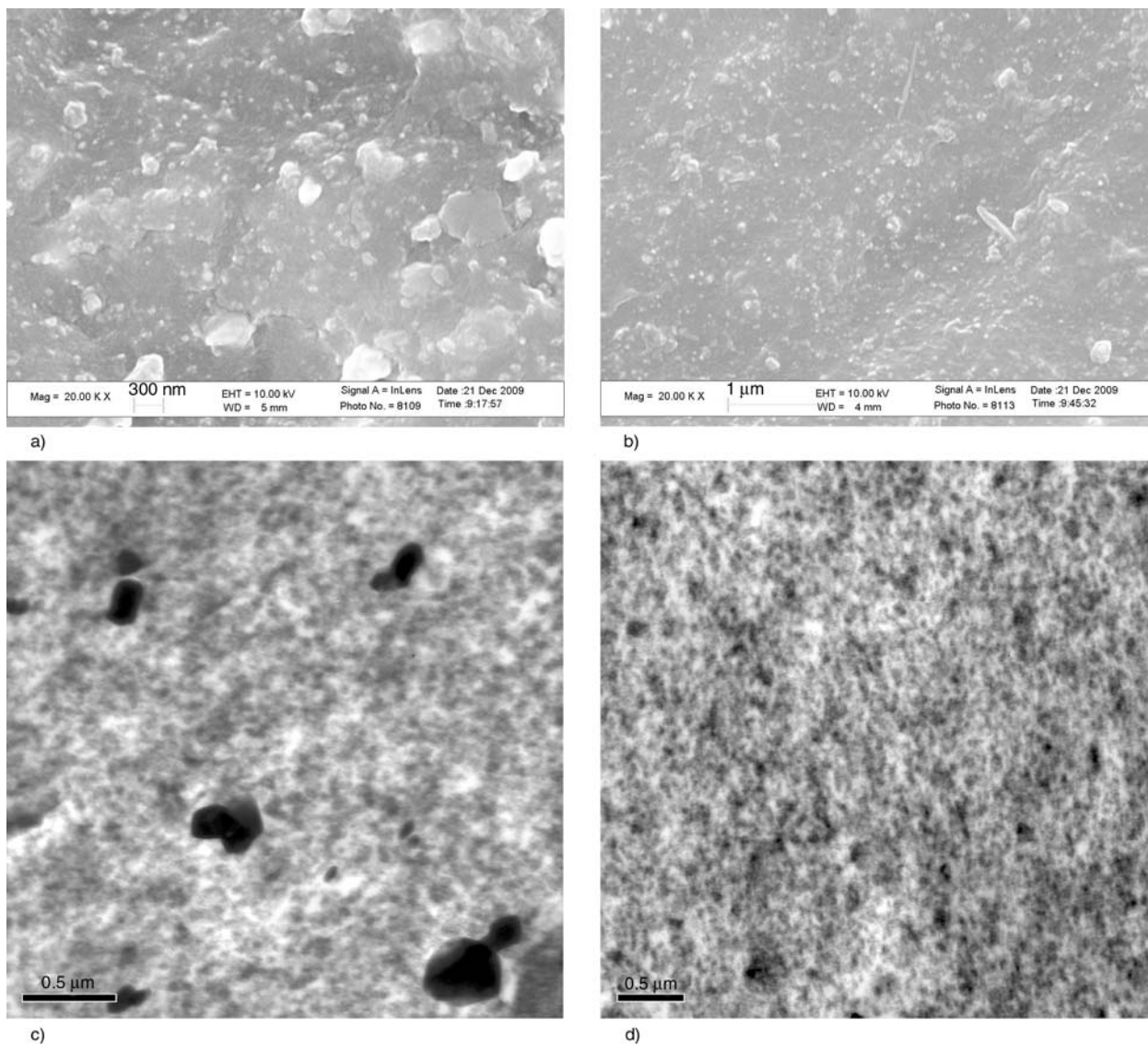

Figure 7. SEM (a, b) and TEM (c, d) photos of R0MimMa and R4MimMa vulcanizates

Table 2. Mechanical performance of the SBR/silica vulcanizates

	R0MimMa	R1MimMa	R2MimMa	R3MimMa	R4MimMa
Stress at 100% [MPa]	2.0±0.1	2.7±0.1	2.6±0.1	2.8±0.1	2.6±0.1
Stress at 300% [MPa]	4.9±0.1	7.8±0.2	7.3±0.4	9.5±0.2	8.9±0.2
Elongation at break [%]	544±12	436±12	506±14	498±14	589±15
Tensile stress [MPa]	15.4±1.0	13.9±1.0	18.9±0.8	19.5±1.0	24.5±1.2
Tear strength [kN·m^{-1}]	34.8±0.5	44.8±1.6	47.7±1.8	49.4±2.5	54.9±1.2
Shore A hardness	69	72	67	68	68
Volume loss [cm^3·1.61 km^{-1}]	2.86	2.68	2.27	1.85	1.56

resistance is also observed. It can be seen that with increasing MimMa loading, the abrasion resistance is consistently improved. The abrasion volume for the R4MimMa is dramatically dropped to 1.56 cm^3·1.61 km^{-1}, which is about half of the control one (2.86 cm^3·1.61 km^{-1}). All the largely improved performances may be related to the substantiated improved silica dispersion and the interfacial bonding [54], which have been disclosed.

The dynamic mechanical analysis (DMA) of the modified vulcanizates was also performed. The dependence of modulus and tangent delta on temperature is revealed in Figure 8. The glass transition temperature (T_g), indicated from tangent delta in Figure 8b, is practically unchanged (both around –50°C). As shown in Figure 8a, the elastic modulus (E') below T_g of R4MimMa is higher than that of R0MimMa. While the loss modulus (E'') of R4MimMa is slightly lowered. Both indicate that the elasticity of the modified vulcanizate below T_g is fortified. It may be due to the weakened silica networking and modified interfacial structure in the SBR/silica composites. However, when the sample is in its high elastic state, no practical difference is observed because in this state the mechanical modulus is mainly dependent on the rubber matrix. Noticeably, the mechanical loss of R4MimMa (Figure 8b) is much higher than the control one. It may

be related to the interfacial structure with noncovalent bondings such as ionic bond or hydrogen bond. It may provide a promising perspective on designing damping material based on the functionality of ILs.

3.7. Interfacial interactions and proposed modification mechanism

Within various methods for evaluating the interfacial interactions with the stress-strain curve, the slopes at certain strains and/or certain ranges of strains have always been utilized [55–57]. However, ignoring the significant impact of crosslink density (V_r) on the modulus may be not sound [57]. According to the theory of rubber elasticity, stress of unfilled rubber vulcanizate (σ_r) can be theoretically expressed by following.

Considering the ending segments which did not contribute to the rubber network formation but negatively influence the stress at certain strains, σ_r could be expressed by Equation (1) [58, 59]:

$$\sigma_r = N_r RT\left(\lambda - \frac{1}{\lambda^2}\right) \tag{1}$$

where R is the universal gas constant, λ is the tensile ratio, T is the absolute temperature, N_r is the
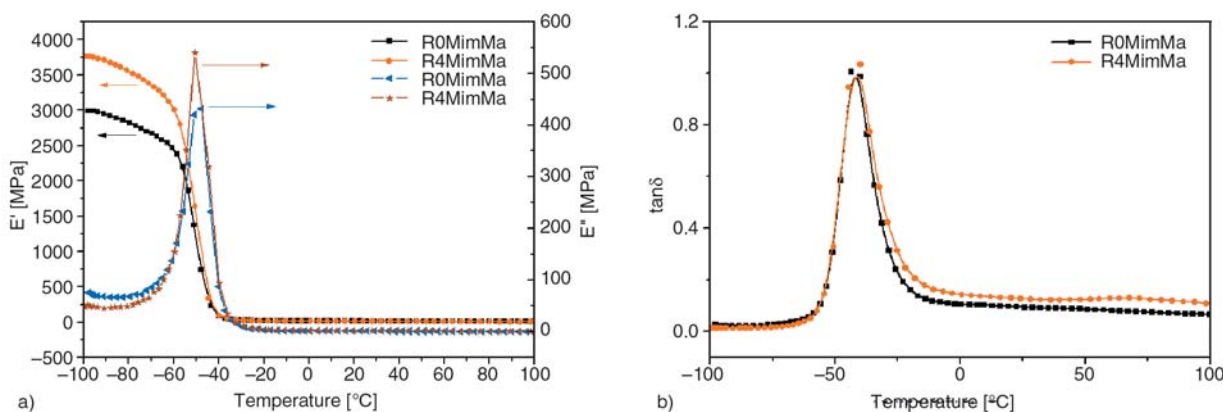

Figure 8. Effect of MimMa on elastic modulus (a) and hysteresis (b) of SBR/silica vulcanizates

density of chain segments introduced by curatives and also introduced by entanglements of rubber chains.

Stress in filled vulcanizates (σ_{com}) was greatly influenced by multi factors including filler, rubber and the interfacial interactions. A possible Equation (2) could be employed to describe σ_{com} as follows:

$$\sigma_{com} = \psi(\sigma_r, \sigma_f, \sigma_{int}) \qquad (2)$$

where σ_r, σ_f and σ_{int} are the stress resulting from rubber network, filler and rubber/filler interfacial phase, respectively. The contributions of these three components to σ_{com} are dependent on strains. Under lower strains, σ_f, which is possibly related to the formation of filler network, has a dominant impact on σ_{com}. However, for the poor deformability of rigid filler network, its contribution to σ_{com} at large strains may be ignored. Thus, at large strains, the strong interaction between rubber chains and filler was regarded as physical and/or chemical crosslinks [60]. Equation (2) could be approximated by the following Equation (3):

$$\sigma_{com} = (N_r + N_{int})RT\left(\lambda - \frac{1}{\lambda^2}\right) \qquad (3)$$

where N_{int} is the density of chain segments additionally introduced by the interfacial interaction, respectively.

In the calculation of N_r, V_r was determined by the equilibrium swelling method. N_r could be expressed by the product of V_r and its functionality of the crosslink points (X_r). Supposed that functionality of crosslink point was 3 and X_r was therefore to be 3/2

in present system, Equation (3) could be rearranged into Equation (4):

$$N_{int} = \left[\frac{\sigma_{com}}{RT(\lambda - \lambda^{-2})} - N_r\right] =$$
$$= \frac{\sigma_{com}}{RT(\lambda - \lambda^{-2})} - \frac{3}{2}V_r \qquad (4)$$

N_{int} could thus be utilized to evaluate the interfacial interaction between rubber chains and filler. Keeping in mind that N_r is largely dependent on the deformation of the filled vulcanizates, curves of N_{int} versus strain of SBR/silica vulcanizates were plotted in Figure 9. Within a range of lower strains, the dramatically high value of N_{int} may be ascribed to the silica network formation. With increasing strains, the value of N_{int} was gradually increased, implying that the SBR/silica interaction was dependent on the deformation of rubber network. Also with increasing strains, stronger interfacial interactions could be observed possibly due to the intensified entanglements and the non Gaussian distribution of the stretched chains. With increasing loading of MimMa as shown in Figure 9, N_{int} was obviously increased. This strongly indicates that the interfacial interaction between rubber and silica was largely improved. It may be related to the graft copolymerization and the high affinity between MimMa and silica as described above.

Accordingly, an interfacial structure was proposed for explaining the possible mechanism in the present system and elucidated in Figure 10. The hydrogen bonding between MimMa and silica can greatly decrease the Payne effect in uncured rubber compounds. The filler networking is obviously
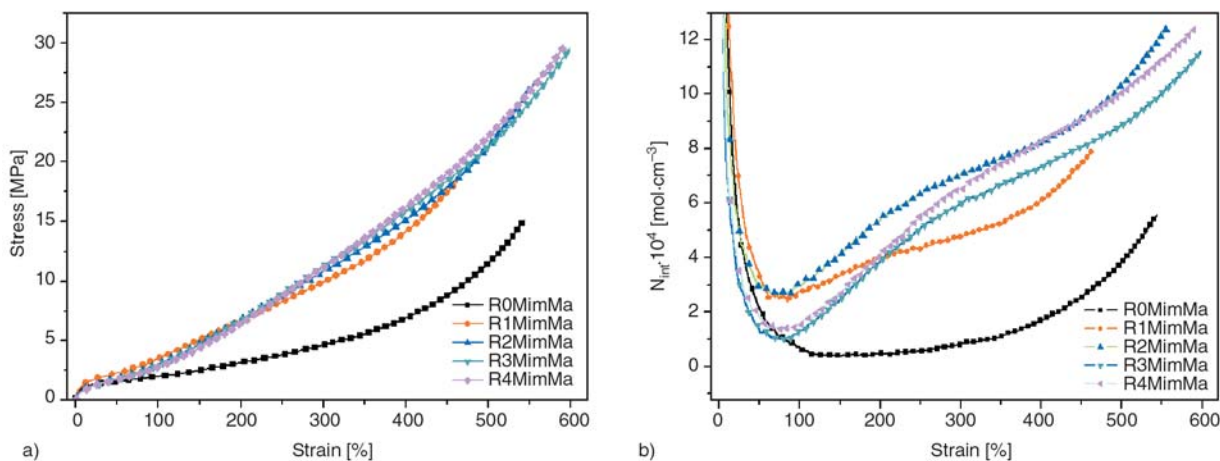

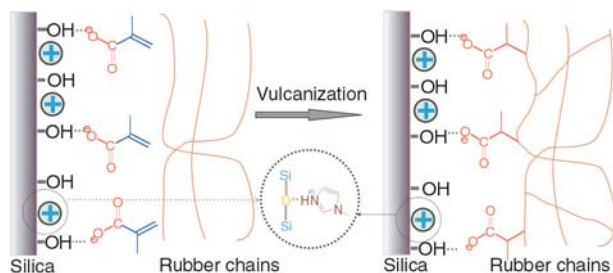**Figure 9.** Dependence of stress (a) and N_{int} (b) on tensile strains

Figure 10. Proposed interfacial structure for the SBR/silica/MimMa composites

restrained by weakening the interactions among silica particles. Once the vulcanization is performed, MimMa is mainly grafted onto SBR molecules via a radical mechanism. The graft product, poly(SBR-g-MimMa), can effectively enhance the compatibility between MimMa and SBR. The hydrogen bonding interactions, which exist in both uncured rubber compounds and rubber vulcanizates, can not only contribute the filler dispersion but also the structure change of SBR/silica interface.

4. Conclusions

A novel functional ionic liquid (IL), 1-methylimidazolium methacrylate (MimMa), was synthesized and investigated as a modifier in a SBR/silica composites. The affinity of MimMa toward silica was proved to be hydrogen bonding between silica and the ionic units. The interaction among silica particles was weakened and the filler networking of silica in the rubber matrix was effectively restrained. MimMa was found to be reactive toward SBR chains through its graft copolymerization onto rubber chains during vulcanization. With a small addition of MimMa, silica dispersion and mechanical performance of the vulcanizates were effectively improved. The increased mechanical loss under dynamic load indicated a promising utilization as a damping material. A modified interfacial structure, which included the high affinity of MimMa toward silica and its reactivity to rubber chains, was accordingly proposed. Remarkable improvements in the rubber performances were related to the proposed interfacial structure.

References

[1] Jesionowski T., Krysztafkiewicz A.: Influence of silane coupling agents on surface properties of precipitated silicas. Applied Surface Science, **172**, 18–32 (2001).
DOI: 10.1016/S0169-4332(00)00828-X

[2] Liu Y-H., Lin H-P., Mou C-Y.: Direct method for surface silyl functionalization of mesoporous silica. Langmuir, **20**, 3231–3239 (2004).
DOI: 10.1021/la0358421

[3] Rao A. V., Kulkarni M. M., Amalnerkar D. P., Seth T.: Surface chemical modification of silica aerogels using various alkyl-alkoxy/chloro silanes. Applied Surface Science, **206**, 262–270 (2003).
DOI: 10.1016/S0169-4332(02)01232-1

[4] Wang M. J.: Effect of polymer-filler and filler-filler interactions on dynamic properties of filled vulcanizates. Rubber Chemistry and Technology, **71**, 520–589 (1998).

[5] Rogers R. D., Seddon K. R.: Ionic liquids- Solvents of the future? Science, **302**, 792–793 (2003).
DOI: 10.1126/science.1090313

[6] Wasserscheid P., Keim W.: Ionic liquids – New 'solutions' for transition metal catalysis. Angewandte Chemie-International Edition, **39**, 3773–3789 (2000).
DOI: 10.1002/1521-3773(20001103)39:21<3772::AID-ANIE3772>3.0.CO;2-5

[7] Huddleston J. G., Visser A. E., Reichert W. M., Willauer H. D., Broker G. A., Rogers R. D.: Characterization and comparison of hydrophilic and hydrophobic room temperature ionic liquids incorporating the imidazolium cation. Green Chemistry, **3**, 156–164 (2001).
DOI: 10.1039/b103275p

[8] Fukushima T., Kosaka A., Ishimura Y., Yamamoto T., Takigawa T., Ishii N., Aida T.: Molecular ordering of organic molten salts triggered by single-walled carbon nanotubes. Science, **300**, 2072–2074 (2003).
DOI: 10.1126/science.1082289

[9] Turner M. B., Spear S. K., Holbrey J. D., Rogers R. D.: Production of bioactive cellulose films reconstituted from ionic liquids. Biomacromolecules, **5**, 1379–1384 (2004).
DOI: 10.1021/bm049748q

[10] Whitten P. G., Spinks G. M., Wallace G. G.: Mechanical properties of carbon nanotube paper in ionic liquid and aqueous electrolytes. Carbon, **43**, 1891–1896 (2005).
DOI: 10.1016/j.carbon.2005.02.038

[11] Fukushima T., Asaka K., Kosaka A., Aida T.: Fully plastic actuator through layer-by-layer casting with ionic-liquid-based bucky gel. Angewandte Chemie-International Edition, **44**, 2410–2413 (2005).
DOI: 10.1002/anie.200462318

[12] Zhou X. S., Wu T. B., Ding K. L., Hu B. J., Hou M. Q., Han B. X.: The dispersion of carbon nanotubes in water with the aid of very small amounts of ionic liquid. Chemical Communications, **2009**, 1897–1899 (2009).
DOI: 10.1039/b900849g

[13] Wang J. Y., Chu H. B., Li Y.: Why single-walled carbon nanotubes can be dispersed in imidazolium-based ionic liquids. ACS Nano, **2**, 2540–2546 (2008).
DOI: 10.1021/nn800510g

[14] Zhang Y. J., Shen Y. F., Li J. H., Niu L., Dong S. J., Ivaska A.: Electrochemical functionalization of single-walled carbon nanotubes in large quantities at a room-temperature ionic liquid supported three-dimensional network electrode. Langmuir, **21**, 4797–4800 (2005).
DOI: 10.1021/la050026+

[15] Gobel R., Hesemann P., Weber J., Moller E., Friedrich A., Beuermann S., Taubert A.: Surprisingly high, bulk liquid-like mobility of silica-confined ionic liquids. Physical Chemistry Chemical Physics, **11**, 3653–3662 (2009).
DOI: 10.1039/b821833a

[16] Zhou Y., Schattka J. H., Antonietti M.: Room-temperature ionic liquids as template to monolithic mesoporous silica with wormlike pores via a sol-gel nanocasting technique. Nano Letters, **4**, 477–481 (2004).
DOI: 10.1021/nl025861f

[17] Cammarata L., Kazarian S. G., Salter P. A., Welton T.: Molecular states of water in room temperature ionic liquids. Physical Chemistry Chemical Physics, **3**, 5192–5200 (2001).
DOI: 10.1039/b106900d

[18] Byrne C., McNally T.: Ionic liquid modification of layered silicates for enhanced thermal stability. Macromolecular Rapid Communications, **28**, 780–784 (2007).
DOI: 10.1002/marc.200600754

[19] Ma J. C., Dougherty D. A.: The cation-π interaction. Chemical Reviews, **97**, 1303–1324 (1997).
DOI: 10.1021/cr9603744

[20] Yoo K., Choi H., Dionysiou D. D.: Ionic liquid assisted preparation of nanostructured TiO_2 particles. Chemical Communications, **2004**, 2000–2001 (2004).
DOI: 10.1039/b406040g

[21] Wu B. H., Hu D., Kuang Y. J., Liu B., Zhang X. H., Chen J. H.: Functionalization of carbon nanotubes by an ionic-liquid polymer: Dispersion of Pt and PtRu nanoparticles on carbon nanotubes and their electrocatalytic oxidation of methanol. Angewandte Chemie-International Edition, **48**, 4751–4754 (2009).
DOI: 10.1002/anie.200900899

[22] Tu W. W., Lei J. P., Ju H. X.: Functionalization of carbon nanotubes with water-insoluble porphyrin in ionic liquid: Direct electrochemistry and highly sensitive amperometric biosensing for trichloroacetic acid. Chemistry-A European Journal, **15**, 779–784 (2009).
DOI: 10.1002/chem.200801758

[23] Chen Y. T., Chen X., Lin Z. Y., Dai H., Qiu B., Sun J. J., Zhang L., Chen G. N.: An electrically heated ionic-liquid/multi-wall carbon nanotube composite electrode and its application to electrochemiluminescent detection of ascorbic acid. Electrochemistry Communications, **11**, 1142–1145 (2009).
DOI: 10.1016/j.elecom.2009.03.033

[24] Yuan L-M., Ren C-X., Li L., Ai P., Yan Z-H., Zi M., Li Z-Y.: Single-walled carbon nanotubes used as stationary phase in GC. Analytical Chemistry, **78**, 6384–6390 (2006).
DOI: 10.1021/ac060663k

[25] Xu Y-P., Tian Z-J., Wang S-J., Hu Y., Wang L., Wang B-C., Ma Y-C., Hou L., Yu J-Y., Lin L-W.: Microwave-enhanced ionothermal synthesis of aluminophosphate molecular sieves. Angewandte Chemie-International Edition, **45**, 3965–3970 (2006).
DOI: 10.1002/anie.200600054

[26] Dai Z., Xiao Y., Yu X. Z., Mai Z. B., Zhao X. J., Zou X. Y.: Direct electrochemistry of myoglobin based on ionic liquid-clay composite films. Biosensors and Bioelectronics, **24**, 1629–1634 (2009).
DOI: 10.1016/j.bios.2008.08.032

[27] Dupont J., Suarez P. A. Z.: Physico-chemical processes in imidazolium ionic liquids. Physical Chemistry Chemical Physics, **8**, 2441–2452 (2006).
DOI: 10.1039/b602046a

[28] Winterton N.: Solubilization of polymers by ionic liquids. Journal of Materials Chemistry, **16**, 4281–4293 (2006).
DOI: 10.1039/b610143g

[29] Marwanta E., Mizumo T., Nakamura N., Ohno H.: Improved ionic conductivity of nitrile rubber/ionic liquid composites. Polymer, **46**, 3795–3800 (2005).
DOI: 10.1016/j.polymer.2005.02.113

[30] Swatloski R. P., Holbrey J. D., Rogers R. D.: Ionic liquids are not always green: Hydrolysis of 1-butyl-3-methylimidazolium hexafluorophosphate. Green Chemistry, **5**, 361–363 (2003).
DOI: 10.1039/B304400a

[31] Lei Y. D., Guo B. C., Liu X. L., Jia D. M.: Structure evolution of carbon black under ionic-liquid-assisted microwave irradiation. Applied Surface Science, **255**, 8488–8493 (2009).
DOI: 10.1016/j.apsusc.2009.05.163

[32] Lei Y. D., Guo B. C., Tang Z. H., Jia D. M.: SBR/silica composites modified by a polymerizable protic ionic liquid. Polymer Journal, **42**, 555–561 (2010).
DOI: 10.1038/pj.2010.43

[33] Guo B., Liu X., Zhou W. Y., Lei Y. D., Jia D. M.: Adsorption of ionic liquid onto halloysite nanotubes: Mechanism and reinforcement of the modified clay to rubber. Journal of Macromolecular Science Part B: Physics, **49**, 1029–1043 (2010).
DOI: 10.1080/00222341003609823

[34] Belieres J-P., Angell C. A.: Protic ionic liquids: Preparation, characterization, and proton free energy level representation. Journal of Physical Chemistry B, **111**, 4926–4937 (2007).
DOI: 10.1021/jp067589u

[35] Greaves T. L., Weerawardena A., Fong C., Drummond C. J.: Many protic ionic liquids mediate hydrocarbon-solvent interactions and promote amphiphile self-assembly. Langmuir, **23**, 402–404 (2006).
DOI: 10.1021/la062895k

[36] Lin B. C., Cheng S., Qiu L. H., Yan F., Shang S. M., Lu J. M.: Protic ionic liquid-based hybrid proton-conducting membranes for anhydrous proton exchange membrane application. Chemistry of Materials, **22**, 1807–1813 (2010).
DOI: 10.1021/Cm9033758

[37] Nakamoto H., Watanabe M.: Brønsted acid-base ionic liquids for fuel cell electrolytes. Chemical Communications, **2007**, 2539–2541 (2007).
DOI: 10.1039/b618953a

[38] Huang M-M., Weingärtner H.: Protic ionic liquids with unusually high dielectric permittivities. ChemPhysChem, **9**, 2172–2173 (2008).
DOI: 10.1002/cphc.200800523

[39] Guo B. C., Chen F., Lei Y. D., Liu X. L., Wan J. J., Jia D. M.: Styrene-butadiene rubber/halloysite nanotubes nanocomposites modified by sorbic acid. Applied Surface Science, **255**, 7329–7336 (2009).
DOI: 10.1016/j.apsusc.2009.03.092

[40] Rajkumar T., Rao G. R.: Synthesis and characterization of hybrid molecular material prepared by ionic liquid and silicotungstic acid. Materials Chemistry and Physics, **112**, 853–857 (2008).
DOI: 10.1016/j.matchemphys.2008.06.046

[41] Jerman I., Jovanovski V., Vuk A. Š., Hocevar S. B., Gaberšcek M., Jesih A., Orel B.: Ionic conductivity, infrared and Raman spectroscopic studies of 1-methyl-3-propylimidazolium iodide ionic liquid with added iodine. Electrochimica Acta, **53**, 2281–2288 (2008).
DOI: 10.1016/j.electacta.2007.09.043

[42] Vuk A. Š., Jovanovski V., Pollet-Villard A., Jerman I., Orel B.: Imidazolium-based ionic liquid derivatives for application in electrochromic devices. Solar Energy Materials and Solar Cells, **92**, 126–135 (2008).
DOI: 10.1016/j.solmat.2007.01.023

[43] Yu J. J., Ryu S. H.: Ultraviolet-initiated photografting of glycidyl methacrylate onto styrene-butadiene rubber. Journal of Applied Polymer Science, **73**, 1733–1739 (1999).
DOI: 10.1002/(SICI)1097-4628(19990829)73:9<1733 ::AID-APP14>3.0.CO;2-J

[44] Watts J. F., Wolstenholme J.: An introduction to surface analysis by XPS and AES. Wiley, Chichester (2003).
DOI: 10.1002/0470867930

[45] Romero-Sánchez M. D., Pastor-Blas M. M., Martín-Martínez J. M.: Adhesion improvement of SBR rubber by treatment with trichloroisocyanuric acid solutions in different esters. International Journal of Adhesion and Adhesives, **21**, 325–337 (2001).
DOI: 10.1016/S0143-7496(01)00005-7

[46] Paparazzo E.: On the XPS analysis of Si–OH groups at the surface of silica. Surface and Interface Analysis, **24**, 729–730 (1996).
DOI: 10.1002/(SICI)1096-9918(19960930)24:10<729 ::AID-SIA183>3.0.CO;2-P

[47] Wang M-J.: The role of filler networking in dynamic properties of filled rubber. Rubber Chemistry and Technology, **72**, 430–448 (1999).

[48] Payne A. R.: The dynamic properties of carbon black-loaded natural rubber vulcanizates. Part I. Journal of Applied Polymer Science, **6**, 57–63 (1962).
DOI: 10.1002/app.1962.070061906

[49] Murphy L. J., Wang M. J., Mahmud K.: Carbon-silica dual phase filler: Part III. ESCA and IR characterization. Rubber Chemistry and Technology, **71**, 998–1014 (1998).

[50] Murphy L. J., Khmelnitskaia E., Wang M-J., Mahmud K.: Carbon-silica dual phase filler: Part IV. Surface chemistry. Rubber Chemistry and Technology, **71**, 1015–1027 (1998).

[51] Wang M. J.: Effect of filler-elastomer interaction on tire tread performance part II. Kautschuk Gummi Kunststoffe, **61**, 33–42 (2008).

[52] Wang M. J., Mahmud K., Murphy L. J., Patterson W. J.: Carbon-silica dual phase filler, a new generation reinforcing agent for rubber, Part I. Characterization. Kautschuk Gummi Kunststoffe, **51**, 348–359 (1998).

[53] Wang M-J., Lu S. X., Mahmud K.: Carbon-silica dual-phase filler, a new-generation reinforcing agent for rubber. Part VI. Time-temperature superposition of dynamic properties of carbon-silica-dual-phase-filler-filled vulcanizates. Journal of Polymer Science Part B: Polymer Physics, **38**, 1240–1249 (2000).
DOI: 10.1002/(SICI)1099-0488(20000501)38:9<1240 ::AID-POLB15>3.0.CO;2-Q

[54] Wang M. J.: Effect of filler-elastomer interaction on tire tread performance. Part III. Kautschuk Gummi Kunststoffe, **61**, 159–165 (2008).

[55] Ayala J. A., Hess W. M., Dotson A. O., Joyce G. A.: New studies on the surface properties of carbon blacks. Rubber Chemistry and Technology, **63**, 747–778 (1990).

[56] Ayala J. A., Hess W. M., Kistler F. D., Joyce G. A.: Carbon-black-elastomer interaction. Rubber Chemistry and Technology, **64**, 19–39 (1991).

[57] Zhang H., Datta R. N., Talma A. G., Noordermeer J. W. M.: Modification of EPDM with alkylphenol polysulfide for use in tire sidewalls, 2-mechanistic and morphological characterizations. Macromolecular Materials and Engineering, **295**, 76–83 (2010).
DOI: 10.1002/mame.200900126

[58] Flory P. J., Rehner J.: Statistical mechanics of crosslinked polymer networks I. Rubberlike elasticity. The Journal of Chemical Physics, **11**, 512–520 (1943).
DOI: 10.1063/1.1723791

[59] Flory P. J., Rehner J.: Statistical mechanics of crosslinked polymer networks II. Swelling. The Journal of Chemical Physics, **11**, 521–526 (1943).
DOI: 10.1063/1.1723792

[60] Cai J. J., Salovey R.: Model filled rubber, Part V. Mechanical properties of rubbery composites. Journal of Materials Science, **36**, 3947–3953 (2001).
DOI: 10.1023/A:1017922322114

Preparation and characterization of the heat-resistant UV curable waterborne polyurethane coating modified by bisphenol A

Z. H. Fang[1,2], *J. J. Shang*[1,2], *Y. X. Huang*[1,2], *J. Wang*[1,2], *D. Q. Li*[1,2], *Z. Y. Liu*[1,2*]

[1]College of Chemistry & Chemical Engineering, Shihezi University, Shihezi, Xinjiang, 832003, People's Republic of China
[2]Xinjiang Bingtuan Key Laboratory for Green Processing of Chemical Engineering, Shihezi, Xinjiang, 832003, People's Republic of China

Abstract. In this study, the modified ultraviolet (UV) curable waterborne polyurethane was obtained from isophorone diisocyanate (IPDI), polyethylene glycol (PEG, MW=600), α,α-dimethylol propionic acid (DMPA), hydroxyethyl acrylate (HEA) and bisphenol A. The rigid moiety was introduced into the main chain of polyurethane to improve its heat-resistance. The copolymer structure was confirmed by Fourier transform infrared spectroscopy (FT-IR). Thermal property and UV curable behavior of the coatings were investigated. The glass transition temperature (T_g) of the modified film was determined by differential scanning calorimetry (DSC). Thermal gravimetric analysis (TGA) was employed to investigate the thermal stability of the modified film. The results show that the average particle diameters increased from 69.25 to 95.12 µm as the content of bisphenol A increased from 0.00 to 9.25%. The optimum bisphenol A dosage was 7.23% (wt%), the T_g of the modified film increased by 7.07°C and 5% weight-loss temperature (233°C) increased by 14°C. The optimum irradiation time was 10–20 minutes after the coatings being painted on an armor plate at room temperature and initiator dosage was 5% (wt%) of the latex.

Keywords: coatings, waterborne polyurethane, bisphenol A, modification, heat-resistant

1. Introduction

Recently, environmental legislation is increasingly strict with coatings industry. The coatings technology is changed from traditional solvent-borne coatings to environmental friendly coatings [1]. Waterborne coatings are new safe materials that can reduce environmental pollution [2]. Because of the virtues in environmental protection, waterborne coatings which were rapidly developed in the past few years have been paid more and more attention and expected to substitute the solvent coatings. But the waterborne coatings are inferior to the solvent coatings for their low chemical resistance, scratch

resistance and slow solidification [3]. Although ultraviolet (UV) radiation is a well-accepted technology for the fast curing of polymeric materials, the UV curable coatings have odor, emission monomers and are not zero-VOC emission [4]. Therefore, in order to overcome above disadvantages, UV curable waterborne coating is generated. Presently, because of many merits, including non-flammable, non-toxic, friendly environment, fast solidification, resistance to organic solvents and excellent mechanical properties [5–8], UV curable waterborne polyurethane coatings (UVWPU) have received more and more attention in the past few

years and their development has resulted in a wide variety of technical approaches in industrial applications, such as fast drying protective coatings, printing inks and adhesives [9, 10]. But they have some inferior properties such as low heat resistance and weak tensile strength when the external temperature exceeds 80°C [11]. Thus, the heat resistance of the UVWPU was improved by several scholars. The conventional method of preparing the heat resistance UV curable waterborne coatings is by way of synthesizing hyperbranched polymer introducing the vinyl groups into the polyurethane chains. For example, Xiong *et al.* [12] synthesized dendritic poly(urethane acrylate) by using 2,4-toluidene diisocyanate, β-hydroxyethyl arcylate, glycidyl methacrylate and polyol under the condition of the thermal degradation temperature of 208°C. It is well known that the thermal degradation of polyurethane contains two steps and the first one is related to the hard segments [13]. However, the heat resistance of the film was improved by synthesizing special hard segment [14].

Therefore, in this article, a series of novel modified polymers of UVWPU are prepared in three steps. Firstly, the preparation of UVWPU prepolymer is synthesized from isophorone diisocyanate (IPDI), polyethylene glycol (PEG, MW=600), 2,2-dimethylol propionic acid (DMPA). Secondly, the UVWPU chain is extended by bisphenol A. finally, the polyurethane main chain is end capped with hydroxyethyl acrylate (HEA), neutralized with triethylamine (TEA) and dispersed with deionized water. The rigid moiety is introduced into the polyurethane molecule by using bisphenol A to improve the thermal properties of coating.

At present, the particle size of the modified UVWPU dispersions was investigated by Microtrac S3500 (Microtrac Montgomeryville, PA, USA). The structure and properties of the modified film were studied by several techniques such as FT-IR (Fourier transform infrared spectroscopy), DSC (differential scanning calorimetry) and TGA. The results show that the modified film has a good heat-resistance.

2. Materials and methods
2.1. Materials
IPDI (pure grade, 98%) was purchased from Alfa Aesar (Massachusetts, USA) and used without fur-

ther purification. Dibutyltin dilaurate (pure grade 90%) was supplied by Energy Chemical (Shanghai, China) as a catalyst. PEG600 (AR) was produced by Shanghai Sangon Biological Engineering Technology and Services Co., Ltd. (Shanghai, China) which was dried for 5 h at 105°C in the vacuum oven before use. DMPA (pure grade 99%) was obtained from Alfa Aesar (Massachusetts, USA), which was purified and dried at 105°C for 4 h in the vacuum oven. Triethylamine (TEA) and acetone (AR) were obtained from Fuyu (Tianjing) Industry of Fine Chemicals Co., Ltd. (Tianjing, China), which were dried for one week with 4 Å molecular sieves (AR, Shanghai Zeolite Molecular Sieve Co., Ltd, China) before use. 2-hydroxyl-2-methylpropiophenone (pure grade, 97%) was supplied by Sigma Aldrich Inc. (Shanghai, China). HEA (pure grade 97%) was supplied by Energy Chemical (Shanghai, China). Bisphenol A (pure grade 99%) was supplied by Bio Basic Inc. (Toronto, Canada). HEA and bisphenol A were used without further purification.

2.2. Preparation of aqueous dispersion
The preparing process of dispersion is shown in Figure 1. The synthesis was carried out in a four-necked, round-bottomed flask equipped with mechanical stirrer, dropping funnel, nitrogen protector and reflux condenser with a drying tube. The reaction temperature was controlled by using a constant-temperature oil bath. Firstly, IPDI, PEG600, and DMPA were added with suitable mole ratio. Then, dibutyltin dilaurate was added into the flask under moderate stirring. The reaction was conducted at 85°C until the theoretical –NCO group content reached. Then, the bisphenol A was added into the system and reacted at 75°C for 2 h. Thereafter the HEA and catalyst were added into the system and reacted at 75°C. The end point of reaction was determined by the disappearance of –NCO stretching peak through infrared (IR) spectroscopy. The acetone was added into the flask to adjust the viscosity of the solution in course of reaction. When the reaction was completed, the reaction system was cooled down to 25°C and the neutralizing agent (TEA) was added and stirred for 30 minutes. The aqueous dispersion was obtained by adding deionized water as the dispersion medium to the reaction system under vigorous stirring. The UV
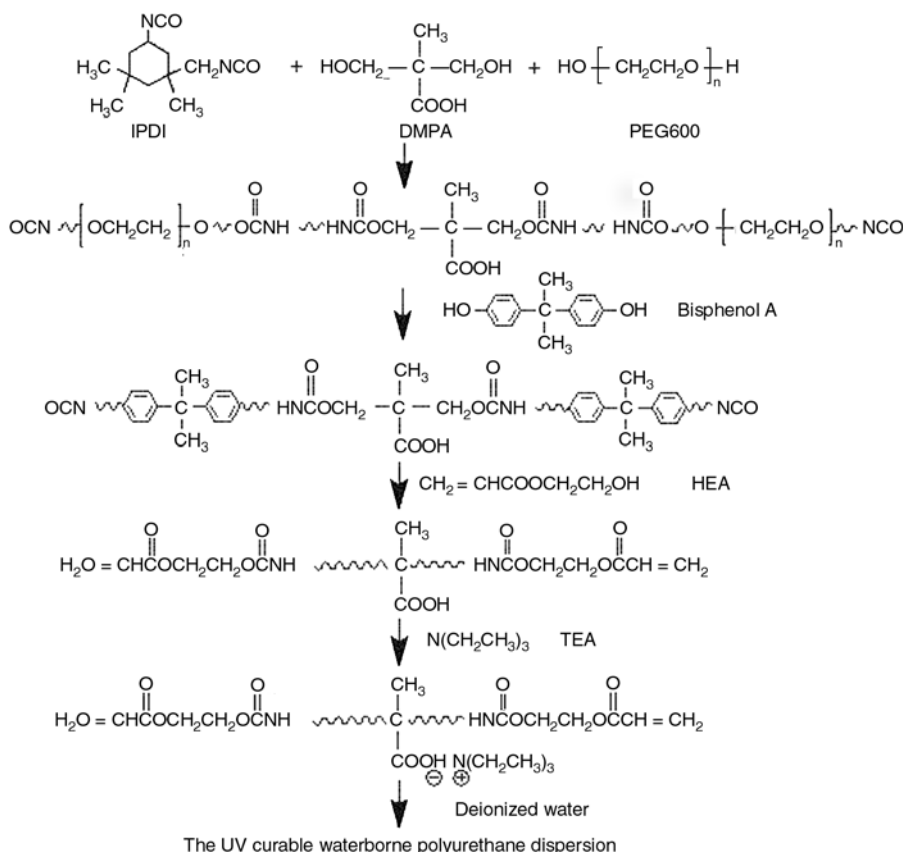
Figure 1. The preparation process of the UVWPU dispersion

curable waterborne polyurethane dispersion (solid content 25%) was obtained after removal of the acetone from the reaction system by rotary vacuum evaporation.

The varying content of –NCO during the reaction was determined by the di-*n*-butylamine back titration method. The theoretical value of –NCO was calculated by Equation (1) [5]:

$$NCO\,[\%] = \frac{(M_{NCO} - M_{OH}) \cdot 42}{W_{NCO} + W_{OH}} \cdot 100 \qquad (1)$$

where M_{NCO} was the mole number of NCO group in the system. M_{OH} was the mole number of OH group. W_{NCO} was the weight of diisocyanate. W_{OH} was the weight of alcohols.

2.3. Preparation of UV cured films

The UVWPU films were formed by irradiating with UV mercury lamp (15 W) in the period of time with suitable photoinitiator 2-hydroxyl-2-methylpropiophenone based on the resins onto an armor plate at room temperature and followed by drying the film 48 h at room temperature after water was evaporated until reaching a constant weight before test.

2.4. Characterization and measurements

2.4.1. IR analysis

The infrared (IR) spectra were recorded with a Fourier transform infrared spectroscopy (FT-IR) instrument in the 400–4000 cm⁻¹ region. Samples were coated directly on to the surface of a KBr crystal, respectively, and measured after film forming and drying.

2.4.2. Particle sizes and distributions

The particle size distributions of the dispersion were measured by using the Microtrac S3500 (Microtrac Inc., Montgomeryville, PA, USA) laser light particle size analysis apparatus. Samples were diluted with water into an appropriate concentration as indicated by the instrument. Test temperature: 25°C.

2.4.3. TGA analysis

The TGA of the UVWPU films were carried out on a Model ZRY-2P (Shanghai Precision and Scientific Instrument Co., Ltd., China) thermal analyzer and the samples were placed in a platinum sample

pan and characterized by performing a scan from 50 to 700°C at heating rate of 10°C/min in N$_2$ atmosphere.

2.4.4. DSC analysis

The T_g of UV cured films is evaluated by Mettler DSC1 (Mettler Toledo, Switzerland) thermal analyzer at temperatures from –100 to 250°C and 10°C/min heating rate in N$_2$ atmosphere.

2.4.5. Gel contents of the film

The ultraviolet curable behaviors of UVWPU were detected in gel content. The gel ratio (G) of the UVWPU specimen was tested by immersing the UVWPU films in acetone at 48 h and was calculated by Equation (2) [15, 16]:

$$G = \frac{M_1}{M_2} \cdot 100 \tag{2}$$

where M_2 and M_1 are the weight of UVWPU film before and after purification, respectively.

3. Results and Discussion

3.1. IR Analysis

The structure of the UVWPU was confirmed by FT-IR as shown in Figure 2. The typical absorption peaks of polyurethane could be seen from the figure at 3310–3360 cm^{-1} (NH stretching vibration), 2850–2950 cm^{-1} (–CH$_2$ stretching vibration), 1714 cm^{-1} (C=O stretching vibration), 1615 cm^{-1} (–C$_6$H$_5$ stretching vibration), 1540 cm^{-1} (NH deformation vibration), 1461 cm^{-1} (–CH$_2$ deformation vibration) and 1124 cm^{-1} (C–O–C stretching vibration), respectively. The –NCO absorption appeared at 2265 cm^{-1} for prepolymer and disappeared for the product which indicated that –NCO groups had been blocked for the product. The –C$_6$H$_5$ absorption appeared at 1615 cm^{-1} for polymer after chain extension which indicated that bisphenol A had been introduced into the main chain of the polyurethane. The spectrum of the product obviously showed the absorption peaks at 1631 cm^{-1} (C=C stretching vibration), which demonstrated that the C=C bond had been incorporated in the polyurethane chains. In addition, the spectra of UVWPU film displayed that the C=C bond decreased significantly after UV radiation, which
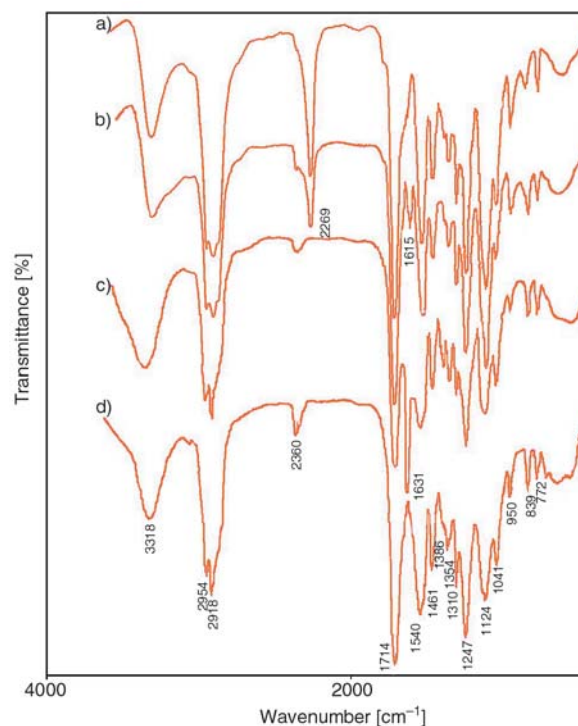

Figure 2. The FT-IR spectra of the modified UVWPU: a) prepolymer, b) polymer after chain extension, c) end-capping polymer, d) cured film)

illustrated that the C=C bond of the polyurethane chains has been polymerized.

3.2. Average particle size of the UVWPU dispersions

It is well known that the average particle size and dispersibility of the UVWPU are governed by several factors such as the hydrophilicity, prepolymer viscosity, ionic group position, chain rigidity, etc. [17, 18]. In this study, the molar ratio of –NCO/–OH, the mass ration of DMPA, HEA and PEG are fixed to a number separately. We have synthesized a series of UVWPU with different content of the bisphenol A. The average particle diameters of the UVWPU dispersions are shown in Figure 3. The average particle diameters of the suspension are mainly affected by the mass ration of bisphenol A and DMPA. Figure 3 and Table 1 show the content of DMPA in the main chain decrease and the dilution stability of the suspension becomes worse as the content of bisphenol A increased from 0.00 to 9.25%, and the average particle diameters increased from 69.25 to 95.12 µm obviously, the reason of which was the decreasing of the hydrophilicity content of the chains and the increased chain rigidity after using bisphenol A as the chain extender.

Table 1. Suspension stability of the UVWPUs at different content of DMPA

Bisphenol A content [wt%]	DMPA content [wt%]	Centrifugal[a]		Dilute stability[b]
		Before	After	
0.00	9.93	Translucence	Translucence	Translucence
2.67	9.42	Translucence	Translucence	Translucence
5.06	8.92	Translucence	Translucence	Translucence
7.23	8.50	Translucence	Translucence	Flocculation
9.25	8.10	Translucence	Translucence	Delamination, flocculation

[a]Rev: 3000 r/min, time: 15 min
[b]Latex was diluted with adding deionized water (solid content of the diluted latex, 3%)
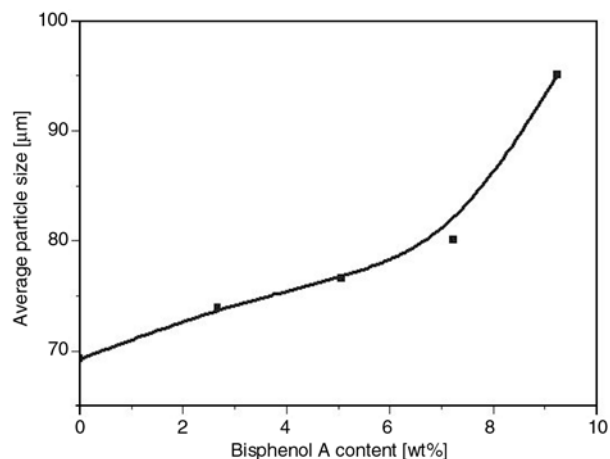 and deposited 48 h before observing experimentally

Figure 3. Effect of the bisphenol A content [wt%] on the latex average particle size

The experiment result of the suspension stability is shown in Table 1.

3.3. Thermal properties

In this study, heat-resistance of the UVWPU film with different content of the bisphenol A is measured according to GB 1735-79 (Table 2). The date of the Table 2 displayed that the heat-resistance of the UVWPU film without bisphenol A is bad, but the heat-resistance of the UVWPU film is increased with the addition of the bisphenol A as chain extender gradually increasing from 0.00 to 7.23%. In our study, we found that the UVWPU film is the best heat-resistance during the content of the bisphenol A at 7.23%. The explanation of this fact is that the chain rigidity is increased and the cross-linking density is decreased which is due to the fact that the content of HEA of system decreases as the content of bisphenol A increased from 0.00 to 9.25%. When the content of bisphenol A exceeds 7.23%, the heat-resistance is decreased by the reduction of the cross-link density.

The TGA curves of the unmodified film and the modified film (content of bisphenol A at 7.23%) are shown in Figure 4. The results showed that the sample UVWPU without bisphenol A had lower initial thermal decomposition temperature than that with bisphenol A as the chain extender. The results of TGA for the modified film obviously indicated the 5% weight-loss temperature of the modified film at 233°C, which was improved by 14°C than
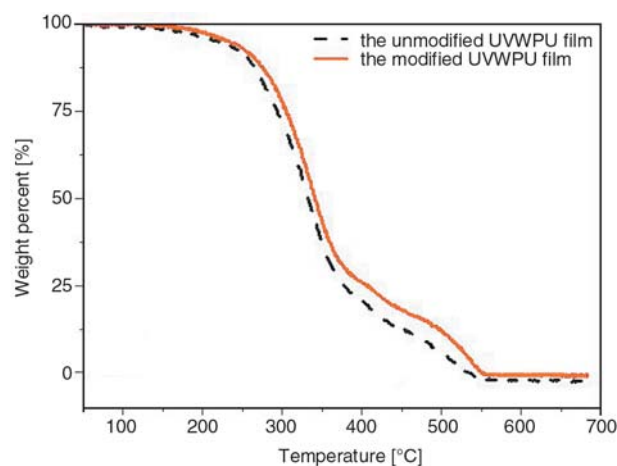
Figure 4. The TGA curves of the UVWPU films at the heating rate of 10°C/min

Table 2. Thermal properties of UVWPU films at different content of bisphenol A

Bipsphenol A content [wt%]	Thermal properties of UVWPU films[a]				
	80°C	90°C	100°C	110°C	120°C
0.00	Acceptance	Below grade	–	–	–
2.67	Acceptance	Acceptance	Acceptance	Below grade	–
5.06	Acceptance	Acceptance	Acceptance	Below grade	–
7.23	Acceptance	Acceptance	Acceptance	Acceptance	Below grade
9.25	Acceptance	Acceptance	Acceptance	Below grade	–

[a]Test time is 2 h, acceptance means the film without color change , crinkle, desquamate, dehisce and frothy

the UVWPU without using bisphenol A. In several studies, it has been concluded that the first and second stages of degradation of polyurethane copolymers are related to the degradations of the hard and soft segments, respectively [11]. The UVWPU polymer coating film in the TGA test presents two stages of degradation associated with the degradations of urethane hard segments and PEG600 soft segment. The unmodified film exhibits lower temperature of 5% weight loss due to the high aliphatic chain of hard segments. Notably, the urethane groups of the modified film after benzene ring incorporating in hard segment decompose at higher temperature than the urethane groups of the unmodified film, implying that the degradation of urethane groups of the modified film is hindered by the aromatic chains.

The DSC curves of the unmodified UVWPU film and the modified UVWPU film (content of bisphenol A at 7.23%) are shown in Figure 5.

Figure 5 showed that the unmodified UVWPU film was observed only one T_g at 34.86°C, which is lower than that of the modified UVWPU film (dosage of bisphenol A at 7.23%) and the T_g of the modified film increased by 7.07°C (about 41.93°C). The explanation is that the chain rigidity is introduced by using bisphenol A as the chain extender, the chain movement is confined, which increases the T_g value. But we can observe a weak peak (139.50°C) in the DSC curve of the modified film, which might be due to the evaporation of water. The UVWPU film with only one T_g might be due to the chain high cross-linking density which was formed by irradiating with UV mercury lamp. In addition, the soft-segment and hard-segment have nicer compatibility.

3.4. Ultraviolet curable behaviors

The most important parameter for the UV curing process is the gel rate. In this study, the contents of initiator (4%) and the content of bisphenol A (7.23%) are fixed separately. We have investigated the effect of different drying times before irradiation on the UV curing process (Figure 6). Figure 6 shows that the sample with drying time at 20 min exhibits the highest gel rate and the curing rate of the modified UVWPU film increases with the increasing of irradiation time at the beginning of irradiation before reaching a constant value. It can also be seen from Figure 6 that the curing rate presents the different variation tendency and increases rapidly. Comparing the sample curve with drying time at 10 min to that at 20 min, we find that the curing rate of the former approaches to that of latter and the curing process is absolutely accomplished after 30 min. Reason for this is the higher water content at the beginning of the irradiation and the low concentration of active center and the curing rate. Therefore, the optimum irradiation time is the 10–20 min after the resins onto an armor plate at room temperature.

There is the optimum initiator content in the specifically system. In this study, the content of bisphenol A (7.23%) is a fixed number. We have investigated the effect of initiator content on the UV curing process (Figure 7). Comparing the sample with initiator contents at 4 and 6%, Figure 7 shows that the highest gel ratio of sample happens at an initiator content of 5%, which is caused by the lower energy utilization rate and active center con-

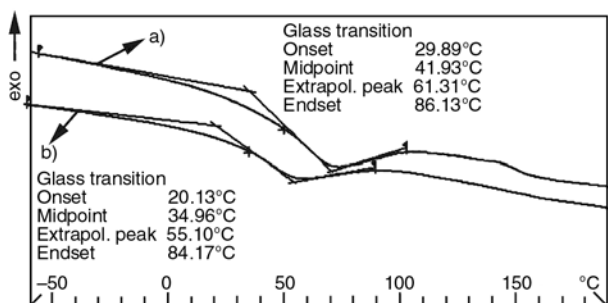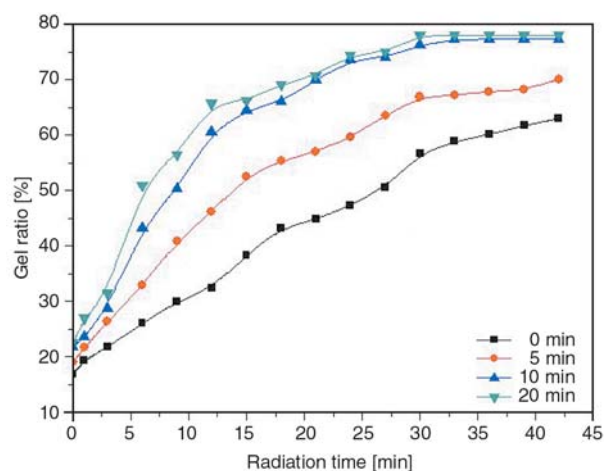**Figure 5.** The DSC curve of the films at the heating rate of 10°C/min: a) the modified UVWPU film, b) the unmodified UVWPU film

Figure 6. Relationship between the gel ratio for different drying time and the radiation time
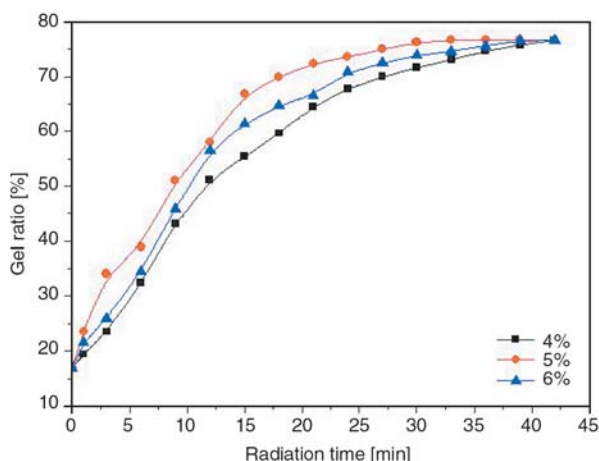
Figure 7. Relationship between the gel ratio for different initiator content and the photo-irradiation time

centration when the initiator content was low. On the other hand, the active center concentration increases with the increasing of the initiator content, which results in the chain termination in superfluous active center coupling each other [19]. Therefore, it can be revealed that the optimum initiator content is 5%.

4. Conclusions

We have successfully synthesized the novel ultraviolet curable waterborne polyurethane coating by introducing the rigid moiety into the main chain of the polyurethane using bisphenol A as chain extender. The results showed that the optimum bisphenol A dosage was 7.23% (wt%), the average particle diameters increased from 69.25 to 95.12 µm as the content of bisphenol A increased from 0.00 to 9.25%. Comparing with the unmodified UVWPU, the obvious advantage of heat resistance of modified UVWPU film was displayed after the rigid chain was introduced into the polyurethane main chain. Otherwise, the T_g of the modified UVWPU was 41.93°C which increased by 7.07°C and the 5% weight-loss temperature (233°C) of the modified UVWPU film increased by 14°C. The curing process indicated that the optimum irradiation time was 10–20 min after the resins onto an armor plate at room temperature and initiator content was 5%.

References

[1] Hwang H-D., Moon J-I., Choi J-H., Kim H-J., Kim S. D., Park J. C.: Effect of water drying conditions on the surface property and morphology of waterborne UV-curable coatings for engineered flooring. Journal of Industrial and Engineering Chemistry, **15**, 381–387 (2009).
DOI: 10.1016/j.jiec.2008.11.002

[2] Athawale V. D., Kulkarni M. A.: Synthesis, characterization, and comparison of polyurethane dispersions based on highly versatile anionomer, ATBS, and conventional DMPA. Journal of Coatings Technology and Research, **7**, 189–199 (2010).
DOI: 10.1007/s11998-009-9184-2

[3] Rahman M. M., Lee W-K.: Properties of isocyanate-reactive waterborne polyurethane adhesives: Effect of cure reaction with various polyol and chain extender content. Journal of Applied Polymer Science, **114**, 3767–3773 (2009).
DOI: 10.1002/app.30848

[4] Lee M. H., Choi H. Y., Jeong K. Y., Lee J. W., Hwang T. W., Kim B. K.: High performance UV cured polyurethane dispersion. Polymer Degradation and Stability, **92**, 1677–1681 (2007).
DOI: 10.1016/j.polymdegradstab.2007.06.006

[5] Bai C. Y., Zhang X. Y., Dai J. B., Li W. H.: A new UV curable waterborne polyurethane: Effect of C=C content on the film properties. Progress in Organic Coatings, **55**, 291–295 (2006).
DOI: 10.1016/j.porgcoat.2005.12.002

[6] Bai C. Y., Zhang X. Y., Dai J. B.: Effect of the hard segment on the properties of UV curable waterborne blocked polyurethanes. Journal of Polymer Research, **15**, 67–73 (2008).
DOI: 10.1007/s10965-007-9144-4

[7] Asif A., Shi W. F., Shen X. F., Nie K. M.: Physical and thermal properties of UV curable waterborne polyurethane dispersions incorporating hyperbranched aliphatic polyester of varying generation number. Polymer, **46**, 11066–11078 (2005).
DOI: 10.1016/j.polymer.2005.09.046

[8] Yang Z. L., Wicks D. A., Hoyle C. E., Pu H. T., Yuan J. J., Wan D. C., Liu Y. S.: Newly UV-curable polyurethane coatings prepared by multifunctional thiol- and ene-terminated polyurethane aqueous dispersions mixtures: Preparation and characterization. Polymer, **50**, 1717–1722 (2009).
DOI: 10.1016/j.polymer.2008.12.018

[9] Asif A., Hu L. H., Shi W. F.: Synthesis, rheological, and thermal properties of waterborne hyperbranched polyurethane acrylate dispersions for UV curable coatings. Colloid and Polymer Science, **287**, 1041–1049 (2009).
DOI: 10.1007/s00396-009-2062-8

[10] Sow C., Riedl B., Blanchet P.: Kinetic studies of UV-waterborne nanocomposite formulations with nanoalumina and nanosilica. Progress in Organic Coatings, **67**, 188–194 (2010).
DOI: 10.1016/j.porgcoat.2009.10.002

[11] Chuang F-S., Tsi H-Y., Chow J-D., Tsen W-C., Shu Y-C., Jang S-C.: Thermal degradation of poly(siloxane-urethane) copolymers. Polymer Degradation and Stability, **93**, 1753–1761 (2008).
DOI: 10.1016/j.polymdegradstab.2008.07.029

[12] Xiong Y-Q., Lu W-H., Xia X-N., Zhang X-H., Xu W-J.: Synthesis of PUA dendrimer and its UV-curing properties (in Chinese). Journal of Hunan University (Natural Sciences), **33**, 81–84 (2006).

[13] Santos C. C., Delpech M. C., Coutinho F. M. B.: Thermal and mechanical profile of cast films from waterborne polyurethanes based on polyether block copolymers. Journal of Materials Science, **44**, 1317–1323 (2009).
DOI: 10.1007/s10853-009-3272-7

[14] Yang D. Y., Zhang P., Qiu F. X., Cao, G. R.: Preparation and properties of the internal crosslinking waterborne polyurethaneurea (in Chinese). Chemical Industry and Engineering Progress, **27**, 270–273 (2008).

[15] Shao C-H., Wang T-Z., Chen G-N., Chen K-J., Yeh J-T., Chen K-N.: Aqueous-based polyurethane with dual-functional curing agent. Journal of Polymer Research, **7**, 41–49 (2000).
DOI: 10.1007/s10965-006-0102-3

[16] Kong X., Li S. M., Qu J. Q., Chen H. Q.: Self-emulsifying hydroxy acrylic polymer dispersions for two component waterborne polyurethane coatings. Journal of Macromolecular Science Part A: Pure and Applied Chemistry, **47**, 368–374 (2010).
DOI: 10.1080/10601320903539330

[17] Bao L-H., Lan Y-J., Zhang S-F.: Synthesis and properties of waterborne polyurethane dispersions with ions in the soft segments. Journal of Polymer Research, **13**, 507–514 (2006).
DOI: 10.1007/s10965-006-9073-7

[18] Park S. H., Chung I. D., Hartwig A., Kim B. K.: Hydrolytic stability and physical properties of waterborne polyurethane based on hydrolytically stable polyol. Colloids and Surfaces A: Physicochemical and Engineering Aspects, **305**, 126–131 (2007).
DOI: 10.1016/j.colsurfa.2007.04.051

[19] Han S-D., Jin Y-Z., Wang F.: Effects on the curing rate of ultraviolet-curable waterborne system (in Chinese). Journal of Beijing University of Chemical of Chemical Technology, **29**, 30–32 (2002).

Melt processable homo- and copolyimides with high thermo-oxidative stability as derived from mixed thioetherdiphthalic anhydride isomers

Y. Han, X. Z. Fang*, X. X. Zuo

Ningbo Key Laboratory of Polymer Materials, Polymers and Composites Division, Ningbo Institute of Materials Technology & Engineering, Chinese Academy of Sciences, Ningbo, 315201, P. R. China

Abstract. A series of homo- and copolyimides based on mixed thioetherdiphthalic anhydride isomers (mixed-TDPA) were synthesized with several kinds of aromatic diamines. The properties of these polyimides were characterized by glass transition temperature (T_g), thermal decomposition temperature, and melt processability. A series of copolyimides were prepared to achieve high T_g concurrently with melt processability by means of selecting appropriate diamines and their composition in the copolyimides. As a result, we obtained rheological information for a series of polyimide resins as a function of temperature, time and shear rate. It is found that the processability (e.g., melt viscosity of polyimides) and ultimate product properties (e.g., T_g of polyimides) can be systematically varied by changing the variety and composition of the aromatic diamines. It has been demonstrated that the incorporation of meta- or flexible diamines improve the melt processability of polyimides significantly. Meanwhile, T_g of copolyimides from dual-diamines can be predicted and regulated. Accordingly, copolyimides from 1,3-phenylenediamine (*m*-PDA) and 3,4'-oxydianiline (3,4'-ODA) were obtained with higher T_g and lower melt viscosity. Such correlations of chemical structures and rheological behavior provide the necessary database for tailor-making new polyimide systems with desirable processability and physical properties.

Keywords: *thermal properties, melt processable, isomeric polyimide, rheology*

1. Introduction

Aromatic polyimides (PIs), due to their excellent thermal stability, superior mechanical strength and good chemical resistance properties, found their application in many industrial fields [1]. The outstanding properties of PIs are based on the combination of their stiff chain structures and ordered structure formation caused by strong interchain interactions. However, these advantages, meanwhile, give rise to poor solubility and processability of PIs. General methods to improve the processability are to incorporate flexible linkage into the polymer backbones [2–4]. This approach, nevertheless, inevitably leads to a decrease of glass transi-

tion temperature (T_g) in many cases. For instance, commercial thermoplastic polyimide Ultem possesses excellent melt processability but its long-term service temperature is limited to lower than 170°C. Moreover, the thermoxidative stability of Ultem is also relatively poor because of the presence of thermally unstable isopropylidene groups in the polymer backbones [5].

Thermoplastic PIs are commonly applied in various industries because of the ease of processing, handling, and storage. Most application requires thermoplastic PIs to exhibit enhanced melt flow behavior at relatively low processing temperatures. However, the high melt viscosity of these materials

requires high pressure to be used in processing to fabricate structural composites and adhesive joints. Therefore, improvements are required to reduce the melt viscosities without compromising other properties.

It was reasoned that introduction of the monomers containing asymmetric or noncoplanar structure to replace the linear symmetrical dianhydride in polymer chain could weaken the interchain interaction thus enhancing the solubility and melt flowability [6]. As of result of that, it has been further demonstrated that replacement of the symmetrical dianhydride in PIs with asymmetric ones decreases the melt viscosity but increases the T_g relative to the corresponding symmetrical PIs [4, 7–9]. Thioetherdiphthalic anhydride (TDPA) is an aromatic bridged dianhydride which has three isomers as shown in Figure 1. The flexible thioether moiety offers the polymer with flexibility and easy melt processability. As a consequence, thioether links have been introduced to many polymers. And polythioetherimides have been synthesized by many researchers for different purposes [10–12]. In previous research, PIs based on 2,3,3',4'-thioetherdiphthalic anhydride (3,4'-TDPA) exhibited a higher T_g than that of symmetric 3,3',4,4'-thioetherdiphthalic anhydride (4,4'-TDPA) and also presented a remarkable drop in the complex viscosity above T_g [13]. This is attributed to the remarkable decrease in the intermolecular interactions of the geometrically irregular 3,4'-TDPA-based PI. According to the research on a similar dianhydride ODPA, TDPA-based polyimides show similar thermal stability and mechanical properties as ODPA-based polyimides, meanwhile, more excellent melt flowability. Moreover, the synthesis of TDPA is more convenient than that of ODPA [4].

Copolymerization by incorporating monomers with flexible moieties, which disrupts the regularity of molecular chain and prevents the interaction of polymer chains, is a simple but effective way for structure modification to balance the processability and the desired properties [14, 15]. For example, 3,4'-oxydianiline (3,4'-ODA) has been proved to be a diamine with polyimide derivatives having better melt flowability than polymers from its isomer 4,4'-oxydianiline(4,4'-ODA) [16]. Other isomeric diamines, such as 1,3-bis(4-aminophenoxy) benzene (TPER) and 1,3-phenylenediamine (*m*-PDA), can also offer polyimides relatively lower melt viscosity than the corresponding *para*-isomers [5, 17]. As a consequence, the processability of copolyimides is enhanced dramatically. The T_g of these copolyimides generally range between that of homopolyimides from the two dianhydrides or diamines [5, 16, 18]. This principle makes it possible to predict the T_g of copolyimides by appropriately selecting the structure and ratios of dianhydride and diamine component while obtaining improved melt flowability of PIs.

Based on the thermal and rheological behavior of 3,4'-TDPA based polyimides, we have successfully prepared copolyimides from mixture of three TDPA isomers (mixed-TDPA) [19]. These kinds of isomeric copolyimides show excellent melt processability similar to the homopolyimide from 3,4'-TDPA. Even though PIs from mixed-TDPA didn't show obviously better melt flowability than that from 3,4'-TDPA, the mixed isomeric dianhydrides can be synthesized by a more convenient routine than that of 3,4'-TDPA [20], which is favorable to prepare a novel melt processable PI with relatively low cost. Meanwhile, it has also been proved that regulating the number-average molecular weight at an appropriate level by stoichiometric imbalance has a significant effect on the melt flowability and the T_g of the copolyimides.

We wish to lower the viscosity of PIs by the replacement of the rigid repeat unit, namely 4,4'-ODA, in the backbone with more flexible ones in order to obtain a high performance melt processable PI. It is expected that the combination of flexible bonds, unsymmetrical moieties in the same macromolecule would yield new PIs offering a compromise between processability, on one side, and the physical and thermal characteristics, on the other. More-
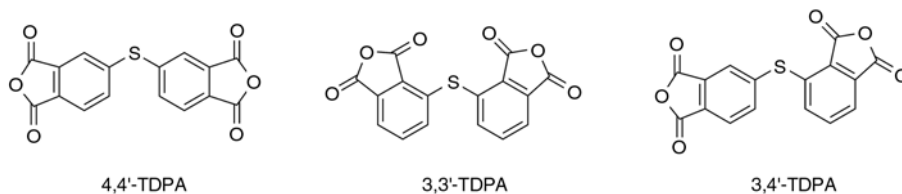

Figure 1. The structures of thioetherdiphthalic anhydride isomers

over, to tailor a PI to satisfy specific requirements between processability and high T_g, a careful examination and selection of variety and composition of diamines is of great importance. Therefore, the first part of this work is to establish the basic structure-property relationships in homopolyimides derived from mixed-TDPA and a variety of aromatic diamines. On the basis of T_gs, thermal stability, and rheological properties, some promising combination of diamines were selected to synthesized melt-processable copolyimides afterwards. And the characterization was focused on processability of these copolyimides systems.

2. Experimental
2.1. Monomer and other chemicals

3- and 4-chlorophthalic anhydrides were obtained from Harbin Shidai Science and Technology Co., Ltd., China and used as received. Anhydrous sodium sulfide was purchased from Inner Mongolia Lichuan Chemistry Co., Ltd., China and used as received. Phthalic anhydride (PA) was purified by sublimation before use. 4,4'-ODA, mp 189~190°C, was purchased from Sinopharm Chemical Reagent Co., Ltd., China and used as received. 3,4'-ODA, mp 74~75°C, was purchased from Changzhou Sunlight Medical Raw Material Co., Ltd., China and recrystallized from a 9/1 ratio of toluene/ethanol before use. 1,4-Phenylenediamine (PDA), mp 138~140°C, was purchased from Sinopharm Chemical Reagent Co., Ltd., and recrystallized from ethyl acetate. *m*-PDA, mp 63~65°C, was purchased from Aladdin and recrystallized from a 9/1 ratio of toluene/cyclohexane before use. 1,4-bis(4-aminophenoxy)benzene (TPEQ), mp 173°C, and TPER, mp 116°C, were purchased from Changzhou Sunlight Medical Raw Material Co., Ltd., and used as received. All of the other reagents were from the Sinopharm Chemical Reagent Co., Ltd. and were of analytical grade.

2.2. Characterization

The inherent viscosities (η_{inh}) were determined at 30°C with an Ubbelohde viscometer and the concentration was 0.5 g·dL^{-1} in *m*-cresol. ^{1}H NMR spectra were recorded on a Bruker AV/ANCE at 400 MHz using DMSO-d_6 as solvent and tetramethylsilane as an internal standard. The differential

scanning calorimetry (DSC) was conducted on a Perkin-Elmer Diamond DSC system at a heating rate of 20°C/min under nitrogen atmosphere. The thermal stability of PIs was estimated using a Perkin-Elemer Diamond TG/DTA thermogravimetric analyzer at a heating rate of 10°C/min in nitrogen or an air atmosphere. The tensile measurements were carried out on an Instron model 5567 tensile tester at a crosshead speed of 5 mm/min at room temperature.

The rheological properties of PIs were performed on a rotational Physica MCR 301 rheometer in an air flow. The parallel plate diameter was 25 mm and the gap was set to about 1.0 mm in all the runs. Sample discs of 25 mm diameter and 1 mm thickness were prepared by press-molding of the powder-like PI at 80°C under high pressure. The complex viscosity (η^*) of PIs was measured by scanning the temperature from 280 to 420°C at a ramp rate of 3°C/min with a frequency of 1 Hz and a strain of 1%. Data acquisitions began 30 min after sample mounting. Meanwhile, dynamic time sweep test was performed at 340°C to evaluate the melt stability of PIs. The η^*, storage elastic modulus (G') and the loss elastic modulus (G'') data were isothermally collected at 340°C with a frequency of 1 Hz and a strain of 1%. Steady shear viscosity of PIs was obtained subjected to small amplitude oscillatory shear at 1% strain over a frequency range from 0.01 to 100 s^{-1}.

2.3. Monomer synthesis

3,3'-TDPA and 4,4'-TDPA and the isomer mixtures, mixed-TDPA were synthesized as reported in the literature [21]. 3,4'-TDPA was synthesized by a method revealed by a Chinese patent [20].

The composition of isomers in mixed-TDPA was calculated according to integrals of ^{1}H NMR spectra of the mixture and three isomers. The detailed information was as presented in reference [19]. As a result, the content of each isomer in the mixture was determined as follows: 21% (3,3'-TDPA), 18% (4,4'-TDPA), and 61% (3,4'-TDPA).

2.4. Polyimides synthesis

All PIs were prepared through one-pot method in *m*-cresol as shown in Figure 2. The inherent viscosity of PIs was regulated in the range of 0.4 to
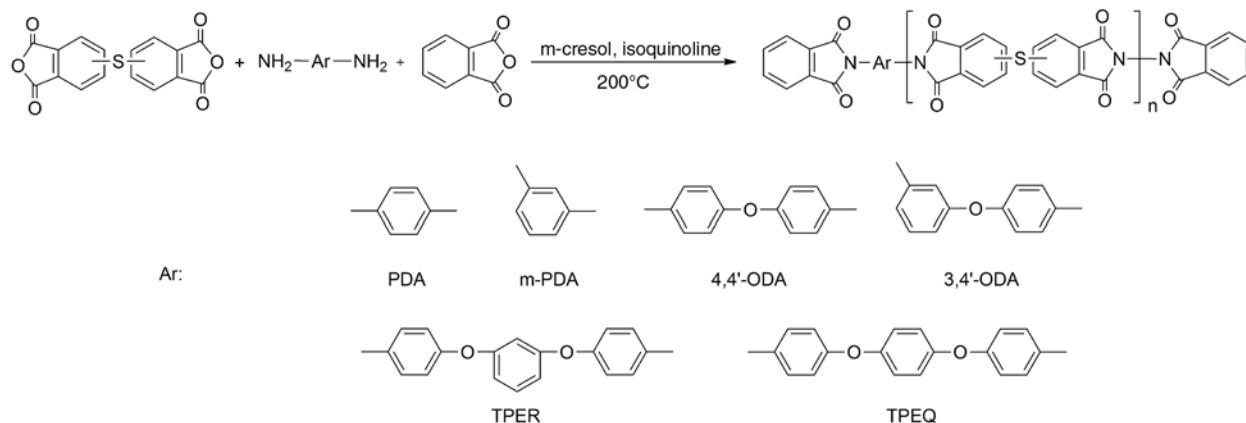
Figure 2. Synthesis of polyimides derived from mixed-TDPA via one-step polymerization

0.5 dL·g^{-1} by the stoichiometric imbalances between dianhydrides and diamines. PA as an end-capper was added for improving thermal stability of PIs. A typical procedure is described as follows as an example.

To a 100 ml completely dried three-neck flask were added 2.0024 g (10.0 mmol) of 4,4'-ODA, 45 ml *m*-cresol under nitrogen flow with stirring. After 4,4'-ODA was completely dissolved, 3.1975 g (9.8 mmol) of mixed-TDPA, 0.0592 g (0.4 mmol, designated as 2%) of PA, and several drops of isoquinoline were added. The mixture was stirred at room temperature for a few minutes and then heated at 100°C for 1 h and 200°C for 8 h. After cooling to room temperature, the viscous solution was diluted with additional 50 ml *m*-cresol and then poured into 500 ml of ethanol with stirring. The precipitate was filtered off, washed with boiling ethanol twice and dried in vacuo at 100°C for 10 h.

The copolyimides based on mixed-TDPA and two different diamines were prepared by similar process as above. Mixed-TDPA was added in the *m*-cresol solution of two diamines until the diamines were completely dissolved.

3. Results and discussion
3.1. Mixed-TDPA-based melt-processable homopolyimides
3.1.1. Basic properties of homopolyimides
In order to appreciate the basic relationships between structure and properties of mixed-TDPA-based PIs, especially the melt processability, we synthesized a series of controlled molecular weight PIs from mixed-TDPA and a variety of diamines via one-step polymerization. Table 1 shows the basic prop-

Table 1. Properties of controlled molecular weight homopolyimides based on mixed-TDPA

Diamines	η_{inh} [dL·g^{-1}]	T_g [°C]	$T_{5\%}$ [°C]		R_w^a
			N$_2$	Air	
4,4'-ODA	0.42	265	529	534	60%
3,4'-ODA	0.45	246	527	538	60%
PDA	0.45	320	537	550	61%
m-PDA	0.41	289	524	530	62%
TPEQ	0.48	234	525	538	55%
TPER	0.47	217	529	518	58%

^{a}Residual weight at 700°C in N$_2$

erties of mixed-TDPA-based homopolyimides, each of which are designated by the abbreviation of diamines. The inherent viscosities of these PIs, which were controlled by the stoichiometric imbalances between dianhydrides and diamines, ranged from 0.4 to 0.5 dL·g^{-1}, indicating the polymer had similarly moderate molecular weights for comparing effectively while ensuring these PIs hold enough mechanical properties. According to our previous investigation, the value of $\eta_{inh} = 0.36$ corresponds to the critical molecular weight for obtaining a flexible film from PIs based on mixed-TDPA and ODA, below which the films become brittle. Meanwhile, all of the PIs in this range of molecular weight exhibit some extent of melt-flow behavior at elevated temperatures. PA was used as an endcapper for the high-temperature stability of the melt viscosity.

An important aspect of this study is the effect of the structural changes on the T_g. As presented in Table 1, the T_g of mixed-TDPA-based PIs determined by DSC varies in a broad range from 217~320°C depending on the structures of the diamines. The introduction of flexible linkage diamines significantly decreases the T_g such as TPER and TPEQ contrary to the effect of more

rigid diamines such as PDA and *m*-PDA. As for the influence of isomerism, the results are as expected in terms of the effect of para/meta isomerism on the T_gs. PIs derived from para diamines show higher T_g's, i.e. $T_g = 265°C$ (mixed-TDPA/4,4'-ODA) > 246°C (mixed-TDPA/3,4'-ODA), 320°C (mixed-TDPA/PDA) > 289°C (mixed-TDPA/*m*-PDA), 234°C (mixed-TDPA/TPEQ) > 217°C (mixed-TDPA/TPER). This phenomenon can be attributed to the PIs with meta linkages disturb the intimate chain stacking necessary for intermolecular interaction [5]. As a result, the introduction of meta-linkages causes a significant decrease in T_g. These PI powders displayed no melting peak in the DSC scan, indicating that these polymers are totally amorphous. It is reasonable because the polyimides derived from three isomeric TDPA are amorphous as well [13]. In the case of mixed-TDPA-based PIs, the less ordered nature attributed by copolymerization of isomers suggests a greater degrees of molecular freedom and less intermolecular interaction.

Thermogravimetric analysis was performed to provide an insight into the thermal and thermoxidative stability of the PIs and to measure their decomposition temperatures. The temperatures at which a weight loss of 5% occurred both under N_2 and air were recorded, along with the char yield at 700°C in N_2. From the results in Table 1, mixed-TDPA-based PIs have a high thermal and thermoxidative stability ($T_{5\%} > 520°C$ both in N_2 and air). It is worthwhile to note that the $T_{5\%}$ of these copolyimides in air is higher than that in nitrogen which is just contrary to a majority of PIs. This phenomenon has been found in the other sulfur-containing polymers, which is ascribed to the different degradation mechanisms in various atmospheres [12, 22].

3.1.2. Melt rheological properties of homopolyimides

In order to obtain melt processable mixed-TDPA-based PIs, we investigate the relationships between melt viscosity and the structure of diamines. Molecular weight is one of the most important variables affecting the viscosity of a polymer melt. Therefore, all of the PIs were prepared at an established range of moderate molecular weight.

Similar to the variation of T_g values with chemical structures, the more rigid structures tend to impart higher melt viscosities to the PIs. Within a series of

PIs based on a several diamines and the same level of molecular weight, melt viscosity generally increases in the order of increasing rigidity of the diamines.

The dynamic melt complex viscosity (η^*) curves are shown in Figure 3 and the η^* in three temperatures and minimum melt viscosity data are tabulated in Table 2. The melt viscosity of all the samples monotonically decreased with increasing temperature except the mixed-TDPA/PDA which has quite a high viscosity during the testing range, the curve of which was not presented in the figure. It is known that the asymmetric structure and meta linkages, such as the moieties in 3,4'-ODA and TPER, significantly decrease the degree of molecular packing and weaken the intermolecular force [17]. As a consequence, the melt flowability is improved by incorporation of these diamines. As presented in the table, the melt viscosity at three temperatures as well as the minimum viscosity of the PIs from TPER and 3,4'-ODA is much lower than that of 4,4'-ODA, which has similar melt viscosity in our previous research [19]. Take the η^* of PI (4,4'-ODA) and PI (3,4'-ODA) as an example, the former has a η^* of 21 100 Pa·s when the processing temperature was 340°C, and the minimum η^*
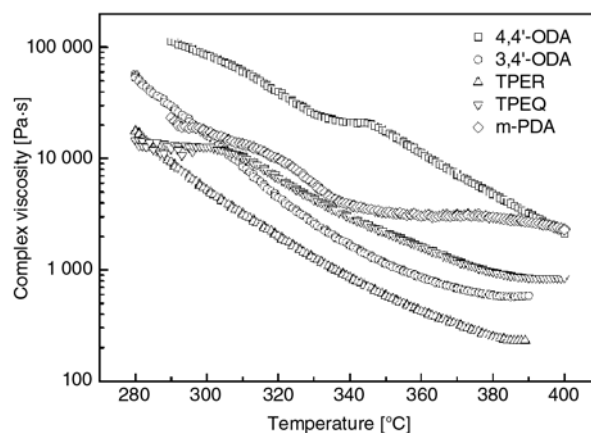

Figure 3. Melt complex viscosity of homopolyimides based on mixed-TDPA

Table 2. Melt complex viscosity of homopolyimides based on mixed-TDPA

Diamines	Melt complex viscosity [Pa·s] at			Min melt viscosity [Pa·s]
	320°C	**340°C**	**380°C**	
4,4'-ODA	39 900	21 100	4 790	2 110 at 400°C
3,4'-ODA	4 440	1 700	595	577 at 385°C
TPER	2 010	858	250	231 at 387°C
TPEQ	6 650	2 970	962	840 at 396°C
m-PDA	9 970	3 890	2 990	2 290 at 400°C
PDA	–	25 300	43 000	25 000 at 341°C

was approximately 2000 Pa·s at 400°C. As for the PI (3,4'-ODA), the polymer has a η^* of 1700 Pa·s at 340°C and a minimum η^* of 577 Pa·s at 385°C. Replacement of the rigid diamine with the more flexible ones causes a sharp decrease in the η^*. These results suggests that molecular interactions of the TPER and 3,4'-ODA based PIs are weaker than the other PI systems. In addition, the PI (*m*-PDA) shows a lower melt viscosity than 4,4'-ODA. This phenomenon is valuable because the incorporation of *m*-PDA could impart a higher T_g to the polymer than that of 4,4'-ODA.

We try to elaborate the intrinsic disparity of melt flowability between PIs from different diamines by means of investigating the melt shear viscosity dependence on shear rate of PIs (4,4'-ODA and 3,4'-ODA) at several temperatures to demonstrate the effect of diamines. And the melt flow activation energy of polymer was calculated to compare between each other. The shear viscosity data as a function of shear rate for PIs from 4,4'-ODA and 3,4'-ODA at 330, 340, 350, 360, and 370°C are presented in Figure 4. Burks and St. Clair [10] had introduced sulfur in polyetherimides for the purpose of obtaining melt processable polyimides. According to the variation of apparent viscosity with shear rate, polythioetherimides in our system have shown better melt flowability than PIs based on 4,4'-bis(3,4-dicarboxyphenoxy)diphenylsulfide dianhydride. PIs from mixed-TDPA and 4,4'-ODA, 3,4'-ODA show shear viscosity less than 10^3 Pa·s when shear rate are close to 10^2 s^{-1}.

Simple mathematical models formulated for representing steady-flow viscosity data in terms of shear rate, the Carreau-Yasuda model has the following form (Equation (1)) [23]:

$$\frac{\eta(\gamma) - \eta_\infty}{\eta_0 - \eta_\infty} = \left[1 + (\lambda\gamma)^a \right]^{\frac{n-1}{a}} \qquad (1)$$

where η_0 is called the zero-shear viscosity, η_∞ is the infinite-shear-rate viscosity. λ is a characteristic viscous relaxation time that defines the location of the transition from Newtonian to shear-thinning behavior. a is a dimensionless parameter (sometimes called 'the Yasuda constant' since it was a parameter added to the Carreau equation by Yasuda) which describes the transition zone between the Newtonian plateau and the shear-thinning region and is inversely related to the breadth of this zone. The exponent ($n-1$) defines the slope of the $\eta(\gamma)$ versus γ curve within the power law region. For our purposes, η_∞ is negligible (zero). Then the Carreau-Yasuda model was employed and the η_0 was calculated by the software of rheometer automatically. The continuous curves drawn in this figure are the Carreau-Yasuda equation fits of the experimental data. For each temperature, one can observe that the low shear rate viscosity plateau broadly spans to 10^{-2} s, which allows the determination of the zero-shear-rate viscosity η_0 with satisfactory accuracy.

The values of η_0 are listed in Table 3. The η_0 of PI (3,4'-ODA) are lower than that of PI (4,4'-ODA) at

Table 3. The zero-shear-rate viscosity of PI (4,4'-ODA) and PI (3,4'-ODA)

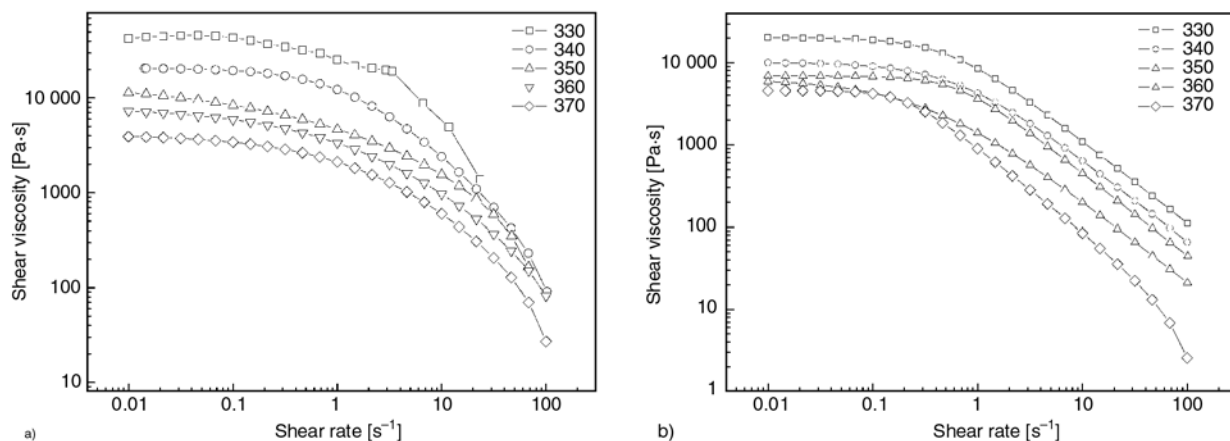| T [°C]	η_0 [Pa·s]	
	4,4'-ODA	**3,4'-ODA**
330	44 813	20 343
340	20 985	10 083
350	15 106	6 900
360	8 013	6 328
370	4 565	4 148

Figure 4. Shear viscosity as a function of shear rate at different temperatures (a): PI(4,4'-ODA), (b): PI(3,4'-ODA)

each temperature, indicating that the former exhibits higher melt flowability. The temperature dependence of the melt shear viscosity of polymer melts is one of the most important parameters in polymer flow, which can be expressed by the Arrhenius expression (Equation (2)) form [24]:

$$\eta_0 = A \exp \frac{E_a}{RT} \qquad (2)$$

where R is the gas constant, A is a constant, and E_a is flow activation energy. E_a varies widely from polymer to polymer, and depends on chain composition. In our system, PIs possess different chain flexibility values related to the diamine structure. This disparity in flexibility and melt flowability are reflected in the different values of E_a.

Values of E_a are calculated by using η_0 data at temperatures from 330 to 370°C. Thus, the E_a values decrease from 178 to 118 kJ/mol, for the PI (4,4'-ODA) and PI (3,4'-ODA), respectively. And there is no doubt that this decrease is induced by the incorporation of asymmetrical moiety into polymer. Increasing flexibility by introduction of flexible bonds and unsymmetrical groups in PIs creates a lower energy barrier for the movement of the molecular chains in polymer melts. As a consequence, this modification leads to a reduction of E_a demonstrating that a more flowable structure is obtained.

3.2. Mixed-TDPA-based melt-processable copolyimides

3.2.1. T_g of copolyimides

It has been known that copolymerization is a simple and effective way for structure modification to balance desired properties, such as melt processability, thermal stability and mechanical properties [14]. Therefore, a series of copolyimides based on mixed-TDPA were prepared on the basis of the structure-property relationships for the homopoly-

imides with the purpose of obtaining PIs with both nice melt-processability and a relative higher T_gs. Table 4 summarizes the properties of copolyimides based on mixed-TDPA and several compositions of diamines. The DSC scans of the copolyimides exhibited only one T_g, indicating that the various repeating units were randomly distributed along the polymer chain, thus a random copolymer structure had been formed. The T_gs of these copolyimides were found to be in the range 229~255°C. The Fox equation is usually used to estimate T_g depending on composition for miscible blends and random copolymers in a bulk state [25]. In this study, the Fox equation was used to estimate composition dependence of the T_gs of copolyimides. The constructed Equation (3) is as follows:

$$\frac{1}{T_g^*} = \frac{w_1}{T_{g1}} + \frac{w_2}{T_{g2}} \qquad (3)$$

where w_1 and w_2 ($w_1 + w_2 = 1$) are the weight fractions of diamine components, T_{g1} and T_{g2} represent the T_g of each homopolyimides. Thus T_g^* is the predicted glass transition temperature depending on the composition of the diamines and the results are listed in the table as well. Most of the T_g^* values predicted by the Fox equation generally are very close to the actual T_gs of the copolyimides. It is worth noting that the T_g of PI (*m*-PDA/TPER) is obviously higher than the predicted value T_g^*. This could be explained by the asymmetric structures of both these diamines significantly offered polymer a more twisted structure resulting that the movement of segment need more space and energy. However, the Fox equation could still be applied to estimate a T_g value of copolyimides in our system.

3.2.2. Melt rheological properties of copolyimides

The dynamic melt complex viscosity curves of copolyimides are shown in Figure 5 and the com-

Table 4. Properties of copolyimides based on mixed-TDPA

Diamines X/Y [mol ratio]	η_{inh} [dL·g^{-1}]	T_g [°C]	T_g^* [°C]	$T_{5\%}$ [°C]		R_w[a]
				N$_2$	AIR	
3,4'/4,4'-ODA(1/1)	0.48	255	255	532	539	59%
TPER/TPEQ(1/1)	0.47	229	226	521	525	56%
TPER/3,4'-ODA(1/1)	0.46	231	228	528	535	59%
m-PDA/TPER(1/1)	0.42	242	233	517	527	56%
m-PDA/3,4'-ODA(3/7)	0.44	255	253	520	529	59%
PDA/3,4'-ODA(15/85)	0.44	249	251	518	529	56%

[a]Residual weight at 700°C in N$_2$

Table 5. Complex melt viscosity of copolyimides based on mixed-TDPA

Diamines	Complex melt viscosity [Pa·s] at			Min melt viscosity [Pa·s]
	320°C	**340°C**	**380°C**	
TPER/TPEQ(1/1)	4 020	2220	1270	1260 at 385°C
TPER/3,4'-ODA(1/1)	5 440	2620	980	909 at 389°C
4,4'/3,4'-ODA(1/1)	10 900	8100	2580	1560 at 403°C
m-PDA/TPER(1/1)	7 090	4100	999	745 at 395°C
m-PDA/3,4'-ODA(3/7)	15 200	5190	800	410 at 403°C
PDA/3,4'-ODA(15/85)	13 200	7420	1 800	1190 at 400°C
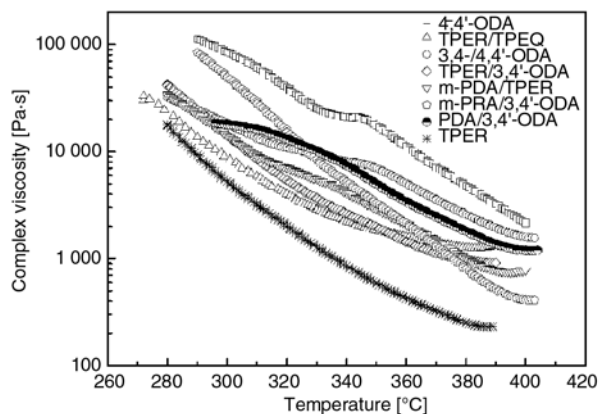
Figure 5. Melt complex viscosity of copolyimides based on mixed-TDPA

plex viscosity in three temperatures and minimum melt viscosity data are tabulated in Table 5. From the figure, most of the copolyimides exhibit enhanced melt flowability compared to PI (4,4'-ODA) which has melt viscosity around 2000 Pa·s at 400°C. In our previous research [19], PIs based on mixed-TDPA and 4,4'-ODA have a similar melt viscosity when the inherent viscosity was between the range of 0.4~0.5 dL/g. However, the T_gs of copolyimides decrease to a certain extent owing to the incorporation of flexible structures. Among the mixed-TDPA-based copolyimides, PI (*m*-PDA/TPER) and PI (*m*-PDA/3,4'-ODA) simultaneously

satisfied the demands of good melt flowability and less sacrifice of T_gs. Therefore, it has been demonstrated that processability of PIs as derived from mixed-TDPA can be be regulated in terms of diamine variety and composition. From the variations of T_gs we can also figure out that flexible diamine with a relatively high molecular weight, namely a greater weight fraction in the composition, has a prominent effect on the physical properties of PIs.

3.3. Melt stability of homo- and co-polyimides based on mixed-TDPA

Isothermal viscosity measurements at 340°C were also conducted on most of the PIs to evaluate the melt stability in air. The curves of melt viscosity and data were showed in Figure 6 and Table 6, respectively. The melt viscosity ratio (*MVR*) calculated by Equation (4) was usually employed to describe the melt stability [26]:

$$MVR = \frac{MV30}{MV5} \tag{4}$$

where *MV*5 and *MV*30 are the melt viscosities [Pa·s] measured at 5 and 30 min, respectively, after the solid sample was completely molten. The polymer
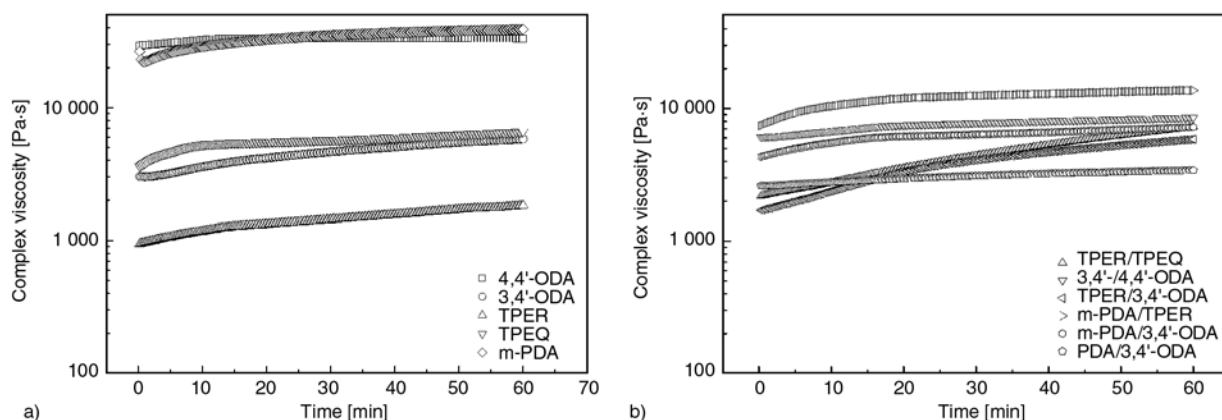

Figure 6. Complex viscosity of homopolyimides (a) and copolyimides (b) in air as a function of time at 340°C

Table 6. Melt stability of homo- and copolyimides based on mixed-TDPA

Diamines	Complex melt viscosity [Pa·s] at			MVR
	5 min	30 min	60 min	
4,4'-ODA	30 800	33 500	33 200	1.1
3,4'-ODA	3 190	4 640	5 800	1.4
TPER	1 060	1 430	1 830	1.3
TPEQ	4 600	5 690	6 600	1.2
m-PDA	26 000	35 100	38 900	1.3
TPER/TPEQ (1/1)	2 450	4 410	7 220	1.8
TPER/3,4'-ODA (1/1)	2 000	4 090	5 850	2.0
4,4'/3,4'-ODA (1/1)	6 370	7 780	8 560	1.2
m-PDA/TPER (1/1)	9 170	12 500	13 700	1.3
m-PDA/3,4'-ODA (3/7)	4 970	6 360	7 240	1.3
PDA/3,4'-ODA (15/85)	2 670	3 100	3 410	1.2

Table 7. Tensile properties of homo- and copolyimides based on mixed-TDPA

Diamines	Tensile properties		
	Strength [MPa]	Modulus [MPa]	Elongation [%]
4,4'-ODA	116	3 200	6.4
3,4'-ODA	120	3 305	5.1
PDA	121	3 521	7.9
m-PDA	111	3 655	8.4
TPEQ	101	2 623	6.8
TPER	116	3 046	6.6
4,4'-ODA/3,4'-ODA(1/1)	113	3 025	6.1
TPEQ/TPER(1/1)	110	2 997	5.8
TPER/3,4'-ODA(1/1)	107	3 012	5.0
m-PDA/TPER(1/1)	108	3 140	4.3
m-PDA/3,4'-ODA(3/7)	121	3 435	7.4
PDA/3,4'-ODA(15/85)	122	3 174	8.6

could be considered as having good melt stability if its *MVR* value was located in the range of 1.0~1.5. In the experiment, the test specimen was loaded when the chamber was preheated, and the measurement was started when the temperature of the specimen and chamber was stabilized at 340°C.

The isothermal viscosity data demonstrate that the viscosity increase after 60 min hold periods is acceptable and most of their *MVR* are below 1.5. This indicates that undesirable crosslinking occurred slightly during the heating process which is favorable for melt-processing.

3.4. Tensile properties of homo- and co-polyimides based on mixed-TDPA

All PIs formed flexible films by dissolving polymer powder in *m*-cresol solution followed by volatizing the solvent in a forced air oven. The tensile properties of the thin films (20~30 μm) were measured at room temperature, and are summarized in Table 7. As shown in the table, the tensile properties of PIs derived from mixed-TDPA indicated strengths at break of 100~120 MPa, tensile moduli ranging from 2600 to 3500 MPa, with an elongation at break of 4~8%. As mentioned above, PIs with molecular weights in this range have nice mechanical properties as thermoplastic engineering materials. It is worthy to note that in the homopolyimides derived from mixed-TDPA, the meta-diamine-based PIs showed a higher tensile modulus than the para-diamine-based PIs. A similar behavior has been observed in PIs from isomeric biphenyltetracarboxylic dianhydrides (BPDA). The a-BPDA/meta-diamine-based PIs showed a higher storage

modulus measured by DMA as well as a higher tensile modulus. This phenomenon may be explained by a mechanism that a segment containing the meta-linkages can take a more extended conformation form than that containing the para-linkages [7–8]. However, this tendency is hard to distinguish in copolyimides based on mixed-TDPA, which may be attributed to that additional monomers disrupt the conformational consistency resulting in the loss of tensile modulus.

3.5. Solubility

Solubility is a major indicator for the intermolecular interaction, chain flexibility and conformation of PIs. Solubility of all the copolyimides were measured quantitatively by dissolving 0.1 g polymer powder in 2 ml solvents and the results are summarized in Table 8. In general, the more bent and non-coplanar structure of molecular backbone result in weaker intermolecular interaction. Thus the PIs derived from *m*-PDA and 3,4'-ODA are more soluble than their counterparts from PDA and 4,4'-ODA. However, PIs from TPER and TPEQ show similarly nice solubility because of their flexible nature. Copolymerization is an effective method to enhance the solubility of insoluble PIs since the addition of a new component disrupts the symmetry and recurrence regularity of the polymer chain. It is also verified by investigating the solubility of copolyimides from diamines resulting better and less soluble PIs, such as *m*-PDA/3,4'-ODA, *m*-PDA/TPER, and PDA/3,4'-ODA. From the results of table, these copolyimides show improved

Table 8. Solubility of homo- and copolyimides based on mixed-TDPA

Diamines	DMAC	DMF	DMSO	NMP	m-cresol	CH₃Cl
PDA	–	–	–	+ –	+	–
m-PDA	–	–	+ –	+ –	+	–
3,4'-ODA	+ +	+ –	+ +	+ +	+ +	+ +
4,4'-ODA	+ –	+ –	+ –	+ –	+	+ +
TPEQ	+ +	+ +	+ +	+ +	+ +	+ +
TPER	+ +	+ +	+ +	+ +	+ +	+ +
m-PDA/3,4'-ODA	+ +	+ +	+	+ +	+ +	+ –
m-PDA/TPER	+ +	+ –	+	+ +	+ +	–
PDA/3,4'-ODA	+ +	+ +	+ +	+ +	+ +	+ +

+ +: soluble at room temperature; +: soluble on heating; + –: partially soluble on heating; –: insoluble

solubility than the homopolyimides based on m-PDA and PDA, respectively.

4. Conclusions

A series of PIs based on mixed-TDPAs have been synthesized with a variety of aromatic diamines. According to the basic structure-property relationships several promising melt processable copolyimides combined with melt flowability and relatively higher T_g were developed. The copolyimides with controlled molecular weights were characterized by good mechanical properties, lower melt viscosities compared to the PI (mixed-TDPA/4,4'-ODA) while remaining high thermal stability. The decrease of E_a from 178 kJ/mol of PI (4,4'-ODA) to 118 kJ/mol of PI (3,4'-ODA) demonstrated that the incorporation of unsymmetrical structure into the polyimide backbone enhances the melt flowability. From the melt thermal stability point of view, this series of copolyimides are favorable to be applied as thermoplastic engineering materials.

References

[1] Wilson D., Stenzenberger H. D., Hergenrother P. M.: Polyimides. Blackie and Son, Glasgow (1990).

[2] Wang K., Fan L., Liu J-G., Zhan M-S., Yang S-Y.: Preparation and properties of melt-processable polyimides based on fluorinated aromatic diamines and aromatic dianhydrides. Journal of Applied Polymer Science, **107**, 2126–2135 (2008).
DOI: 10.1002/app.25056

[3] Zuo H. J., Chen J. S., Yang H. X., Hu A. J., Fan L., Yang S. Y.: Synthesis and characterization of melt-processable polyimides derived from 1,4-bis(4-amino-2-trifluoromethylphenoxy)benzene. Journal of Applied Polymer Science, **107**, 755–765 (2008).
DOI: 10.1002/app.26965

[4] Li Q., Fang X., Wang Z., Gao L., Ding M.: Polyimides from isomeric oxydiphthalic anhydrides. Journal of Polymer Science Part A: Polymer Chemistry, **41**, 3249–3260 (2003).
DOI: 10.1002/pola.10918

[5] Shi Z., Hasegawa M., Shindo Y., Yokata R., He F., Yamaguchi H., Ozawa H.: Thermo-processable polyimides with high thermo-oxidative as derived from oxydiphthalic anhydride and bisphenol A type dianhydride. High Performance Polymers, **12**, 377–393 (2000).
DOI: 10.1088/0954-0083/12/3/302

[6] Ding M.: Isomeric polyimides. Progress in Polymer Science, **32**, 623–668 (2007).
DOI: 10.1016/j.progpolymsci.2007.01.007

[7] Hergenrother P. M., Watson K. A., Smith J. G., Connell J. W., Yokota R.: Polyimides from 2,3,3′,4′-biphenyltetracarboxylic dianhydride and aromatic diamines. Polymer, **43**, 5077–5093 (2002).
DOI: 10.1016/S0032-3861(02)00362-2

[8] Chen C., Yokota R., Hasegawa M., Kochi M., Horie K., Hergenrother P.: Isomeric biphenyl polyimides. (I) Chemical structure-property relationships. High Performance Polymers, **17**, 317–333 (2005).
DOI: 10.1177/0954008305055556

[9] Fang X. Z., Wang Z., Yang Z. H., Gao L. X., Li Q. X., Ding M. X.: Novel polyimides derived from 2,3,3′,4′-benzophenonetetracarboxylic dianhydride. Polymer, **44**, 2641–2646 (2003).
DOI: 10.1016/S0032-3861(03)00181-2

[10] Burks H. D., St. Clair T. L.: Processable aromatic polyimides. Journal of Applied Polymer Science, **30,** 2401–2411 (1985).
DOI: 10.1002/app.1985.070300611

[11] Glatz F. P., Mülhaupt R.: Syntheses and properties of soluble poly(arylene thioether imide)s and the corresponding poly(arylene sulfone imide)s. Polymer Bulletin, **31**, 137–143 (1993).
DOI: 10.1007/BF00329958

[12] Liu J-G., Shibasaki Y., Ando S., Ueda M.: Synthesis and thermal properties of polythioetherimides derived from 4,4′-[p-thiobis(phenylenesulfanyl)]diphthalic anhydride and various aromatic diamines. High Performance Polymers, **20**, 221–237 (2008).
DOI: 10.1177/0954008307082508

[13] Zhang M., Wang Z., Gao L. X., Ding M. X.: Polyimides from isomeric diphenylthioether dianhydrides. Journal of Polymer Science Part A: Polymer Chemistry, **44**, 959–967 (2006).
DOI: 10.1002/pola.21204

[14] de Abajo J., de la Campa J. G.: Processable aromatic polyimides. Progress in Polyimide Chemistry I: Advances in Polymer Science, **140**, 23–59 (1999).
DOI: 10.1007/3-540-49815-X_2

[15] Hasegawa M., Sensui N., Shindo Y., Yokota R.: Improvement of thermoplasticity for s-BPDA/PDA by copolymerization and blend with novel asymmetric BPDA-based polyimides. Journal of Polymer Science Part B: Polymer Physics, **37**, 2499–2511 (1999).
DOI: 10.1002/(SICI)1099-0488(19990901)37:17 <2499::AID-POLB21>3.0.CO;2-G

[16] Yokota R., Yamamoto S., Yano S., Sawaguchi T., Hasegawa M., Yamaguchi H., Ozawa H., Sato R.: Molecular design of heat resistant polyimides having excellent processability and high glass transition temperature. High Performance Polymers, **13**, S61–S72 (2001).
DOI: 10.1088/0954-0083/13/2/306

[17] Simone C. D., Scola D. A.: Phenylethynyl end-capped polyimides derived from 4,4′-(2,2,2-trifluoro-1-phenylethylidene)diphthalic anhydride, 4,4′-(hexafluoroisopropylidene)diphthalic anhydride, and 3,3′,4,4′-biphenylene dianhydride: Structure-viscosity relationship. Macromolecules, **36**, 6780–6790 (2003).
DOI: 10.1021/ma0300701

[18] Tamai S., Oikawa H., Ohta M., Yamaguchi A.: Melt processable copolyimides based on 4,4′-bis(3-aminophenoxy)biphenyl. Polymer, **39**, 1945–1949 (1998).
DOI: 10.1016/S0032-3861(97)00491-6

[19] Han Y., Fang X. Z., Zuo X. X.: The influence of molecular weight on properties of melt-processable copolyimides derived from thioetherdiphthalic anhydride isomers. Journal of Materials Science, **45**, 1921–1929 (2010).
DOI: 10.1007/s10853-009-4179-z

[20] Yang Z. H., Ding M. X.: The method of synthesis of diphenylthioethertetracarboxylic acid and its derivatives. Chinese Patent 1081436A (1994).

[21] Evans T. L., Williams F. J., Donahue P. E., Grade M. M.: Synthesis and polymerization of thioether dianhydride. Polymer Preprints, **24**, 268–269 (1984).

[22] Li X-G., Huang M-R., Bai H., Yang Y-L.: High-resolution thermogravimetry of polyphenylene sulfide film under four atmospheres. Journal of Applied Polymer Science, **83**, 2053–2059 (2002).
DOI: 10.1002/app.10011

[23] Bird R. B., Armstrong R. C., Hassager O.: Dynamics of polymeric liquids, fluid mechanics. Wiley, New York (1987).

[24] Graessley W. W., Raju V. R.: Some rheological properties of solutions and blends of hydrogenated polybutadiene. Journal of Polymer Science Polymer Symposia, **71**, 77–93 (1984).
DOI: 10.1002/polc.5070710109

[25] Fox T. G.: Influence of diluent and of copolymer composition on the glass temperature of a polymer system. Bulletin of the American Physical Society, **1**, 123–125 (1956).

[26] Kuroki T., Sakata Y., Okumura T.: Crystalline polyimide for melt molding with satisfactory thermal stability. U.S. Patent 6458912 (2002).

Poly(vinyl chloride)-grafted multi-walled carbon nanotubes via Friedel-Crafts alkylation

X. L. Wu, P. Liu**

Key Laboratory of Nonferrous Metal Chemistry and Resources Utilization of Gansu Province and State Key Laboratory of Applied Organic Chemistry, College of Chemistry and Chemical Engineering, Lanzhou University, Lanzhou 730000, China

Abstract. A novel approach was developed for the surface modification of the multi-walled carbon nanotubes (MWCNTs) with high percentage of grafting (PG%) by the grafting of polymer via the Friedel-Crafts alkylation. The graft reaction conditions, such as the amount of catalyst added, the reaction temperature, and the reaction time were optimized for the Friedel-Crafts alkylation of the MWCNTs with poly(vinyl chloride) (PVC) with anhydrous aluminum chloride ($AlCl_3$) as catalyst in chloroform ($CHCl_3$). The Fourier Transform Infrared (FT-IR), Raman, and thermogravimetric (TGA) analysis showed that PVC had been successfully grafted onto MWCNTs both at the ends and on the sidewalls by the proposed Friedel-Crafts alkylation. The PVC grafted MWCNTs (PVC-MWCNTs) could be dispersed well in organic solvent and the dispersion was more stable.

Keywords: nanomaterials, carbon nanotubes, surface modification, Friedel-Crafts alkylation, polyvinyl chloride

1. Introduction

Carbon nanotubes (CNTs) have won more and more intense interest since their discovery because of their unique structural, mechanical and electronic properties [1–3]. However, the processing of CNTs has been limited by their insolubility in most common solvents, due to the strong inter-tube van der Waals attraction [4].

Consequently, various methods have been proposed for functionalizing CNTs. Functionalization of CNTs with polymers is gaining comprehensive interest because the polymer chains can promote the solubility of CNTs in common solvents. The widely used methods for the chemical functionalization of CNTs are the 'grafting to' and 'grafting from' approaches [5]. The functional groups, such as carboxyl groups [6] or amino groups [7] for the 'grafting to' approaches, and initiating groups [8]

or polymerizable groups [9] for the 'grafting from' approaches, must be introduced onto the surfaces of CNTs before the grafting reactions.

Most recently, the research interest in the research field has focused on the 'free radical addition' [10–12] and 'anionic addition' [13, 14] approaches for the chemical functionalization of CNTs by the addition reaction of the polymer radicals or polymer anions on the surface π-bonds of the CNTs. These approaches seem to be simpler than the 'grafting to' and 'grafting from' approaches because the surface modification of the CNTs with the functional groups is not needed.

Friedel-Crafts reaction has been successfully applied for the chemical functionalization of carbon nanofibers [15] and CNTs with small molecules [16, 17]. In the present work, we report the grafting of poly(vinyl chloride) (PVC) onto multi-walled car-

---

*Corresponding author, e-mail: pliu@lzu.edu.cn

bon nanotubes (MWCNTs) MWCNTs both at the ends and on the sidewalls via the Friedel-Crafts alkylation reaction with anhydrous aluminum chloride ($AlCl_3$) as catalyst for the first time. Similarly to the 'free radical addition' and 'anionic addition' approaches, the pre-functionalization of the MWC-NTs with functional groups is not needed. Furthermore, the pristine MWCNTs without any treatment were used in the proposed method. Therefore, the original length of the MWCNTs remained.

2. Experimental
2.1. Materials
MWCNTs, synthesized by a thermal chemical vapor deposition method, were obtained from Shenzhen Nanotech Port Co., Ltd. (Shenzhen, China) with an average diameter of 20–40 nm and a purity of 95%. The MWCNTs were used without any purification process.

PVC was bought from the Chemical factory of Yanguoxia in Gansu, and dried in vacuum. Anhydrous aluminum chloride ($AlCl_3$) was provided by Sitong Chemical Factory in Tianjin. Chloroform ($CHCl_3$) was dehydrated with anhydrous calcium chloride ($CaCl_2$) and then distilled under reduced pressure. Other solvents were analytical grade obtained from Tianjin Chemical Co. Ltd.

2.2. Friedel-Crafts alkylation
For a typical Friedel-Crafts alkylation reaction, 0.20 g MWCNTs, certain amount of anhydrous aluminum chloride, and dehydrated chloroform 30 ml were combined into a three neck flask. Then the mixture was stirred electromagnetically at certain temperature for certain time under nitrogen atmosphere. After being cooled to room temperature, the mixture was dispersed in THF with ultrasonic vibration and centrifuged (12 000 rpm for 10 min) until no PVC could be detected in the supernatant liquid. The resulting products, poly(vinyl chloride) grafted MWCNTs (PVC-MWCNTs), were dried naturally. The conditions of the Friedel-Crafts alkylation reaction were summarized in Table 1.

For comparison, the reaction was also conducted without PVC or MWCNTs at 60°C for 30 h.

2.3. Analysis and characterizations
A Bruker IFS 66 v/s infrared spectrometer was used for the Fourier transform infrared (FTIR) spectroscopy analysis. Raman measurements were carried out on the powder samples using FT-Raman spectrometer (BRUKER RFS 100/S) with the excitation laser of Nd:YAG (wavelength: 1064 nm). The morphologies of the MWCNTs and PVC-MWCNTs were characterized with a JEM-1200 EX/S transmission electron microscope (TEM). The powders were dispersed in THF in an ultrasonic bath for 5 min, and then deposited on a copper grid covered with a perforated carbon film. Thermogravimetric analysis (TGA) was performed with a Perkin-Elmer TGA-7 system at a scan rate of 20°C·min^{-1} to 800°C in N_2. The percentage of grafting (PG%) of the PVC-MWCNTs was calculated from the TGA analysis.

3. Results and discussion
Friedel-Crafts alkylation, an electrophilic substitution reaction between aromatic rings and a chloroalkane with strong Lewis acids as catalysts, allows the synthesis of alkylated products via the reaction of arenes with alkyl halides or alkenes. Recently, it had been used for the surface chemical

Table 1. The conditions of the Friedel-Crafts alkylation reaction

Samples	Reaction conditions			Weight loss at 400°C [%]	PG%
	Catalyst [g]	Reaction temperature [°C]	Reaction time [h]		
MWCNTs$_c$	0.50	60	30	4.91	–
PVC$_c$	0.50	60	30	67.27	–
PVC-MWCNTs 1	0.50	60	6	38.58	117.4
PVC-MWCNTs 2	0.50	60	12	39.32	123.1
PVC-MWCNTs 3	0.50	60	18	39.94	128.2
PVC-MWCNTs 4	0.50	60	24	43.00	156.9
PVC-MWCNTs 5	0.50	60	30	44.87	178.4
PVC-MWCNTs 6	0.75	60	30	46.64	202.3
PVC-MWCNTs 7	1.00	60	30	49.27	246.4
PVC-MWCNTs 8	0.50	50	30	33.44	84.3

functionalization of the carbon nanotubes with small organic molecules, such as lauroyl chloride [16] and 4-(2,4,6-trimethylphenoxy)benzamide (TMPBA) [17]. Here the reaction was used for the grafting of poly(vinyl chloride) (PVC) onto the surfaces of MWCNTs with anhydrous aluminum chloride as catalyst.

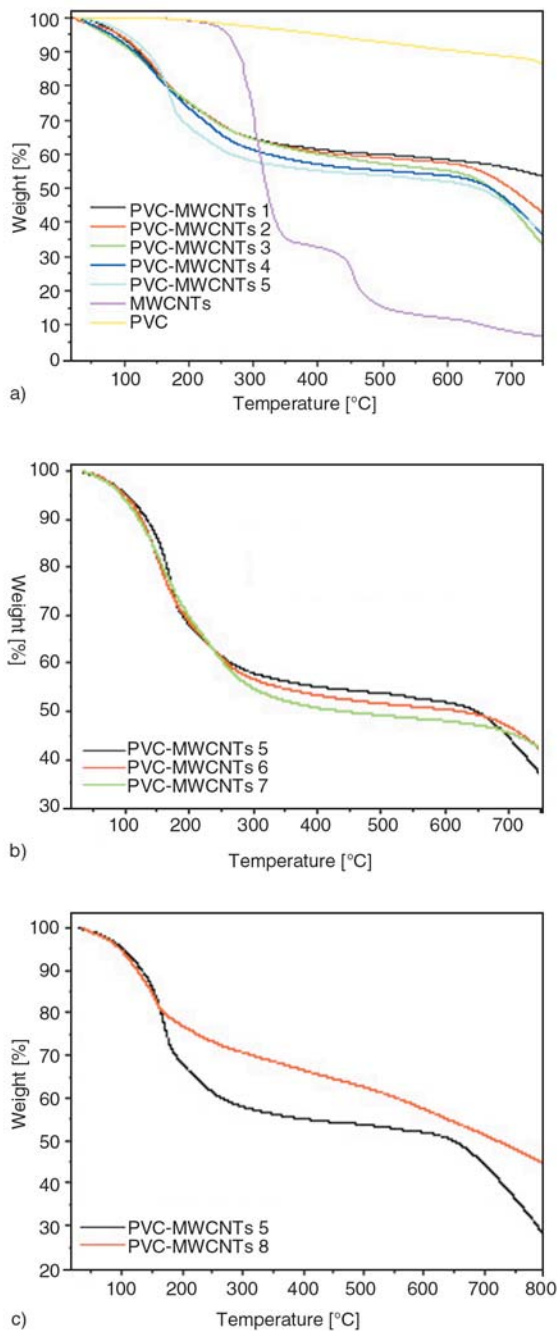The TGA curves of the poly(vinyl chloride) grafted multi-walled carbon nanotubes (PVC-MWCNTs)

Figure 1. TGA curves of the PVC-MWCNTs obtained from the different reaction conditions: (a) effect of the reaction time; (b) effect of the catalyst added; and (c) effect of the reaction temperature

prepared with different reaction conditions, the product from the comparative experiment without PVC (defined as MWCNTs$_c$) or without MWCNTs (defined as PVC$_c$) are presented in Figure 1. The weight loss of less than 5% was found in the comparative MWCNTs sample (MWCNTs$_c$) until 400°C, it indicated that nearly no CHCl$_3$ has reacted with the CNTs under the reaction condition. However, the comparative PVC sample (PVC$_c$) had a weight loss of near to 70% in the temperature range of 200–400°C, as summarized in Table 1. So the percentage of grafting (PG%) could be calculated by the comparison of the weight loss of PVC$_c$ and MWCNTs$_c$ with those of the PVC-MWCNTs until 400°C (Table 1). The lower on-set thermal decomposition temperature of the PVC-MWCNTs than that of the pure PVC might be caused by the residual catalyst AlCl$_3$, which is also the catalyst for the thermal decomposition of PVC [18].

The effect of the reaction conditions on the percentage of grafting (PG%) of the products, the poly(vinyl chloride) grafted multi-walled carbon nanotubes (PVC-MWCNTs), calculated from their TGA analysis (Figure 1), were summarized in Table 1. The PVC-MWCNTs samples (1–8) had the PG% in the range of about 110–180%. It means that 1.10–1.80 g PVC had been grafted onto per gram of the pristine MWCNTs. It is much higher than the polymer grafted CNTs with other methods. It might be due to the crosslinking reaction of PVC under the grafting condition because that the comparative PVC sample (PVC$_c$) was gel and could not be dissolved in THF. Furthermore, the strategy developed is facile because that the pre-functionalization of the CNTs is not needed. So another strong point emerges that the length of the pristine CNTs could be maintained in the procedure. It could be concluded that the longer reaction time, more catalyst added, and higher reaction temperature favored the Friedel-Crafts alkylation between MWCNTs and PVC.

After the Friedel-Crafts alkylation of the pristine MWCNTs with PVC and the extraction of the products with THF, some absorbance peaks such as the symmetrical stretching vibrations of C–Cl at 600–700 cm^{-1}, stretching vibrations of C–H at 2930, 2850, and 1250 cm^{-1}, asymmetrical vibrations of –CH$_2$ at 1420 cm^{-1}, which do not exist in the FTIR spectrum of the pristine MWCNTs, appeared in that of the PVC-MWCNTs (Figure 2).
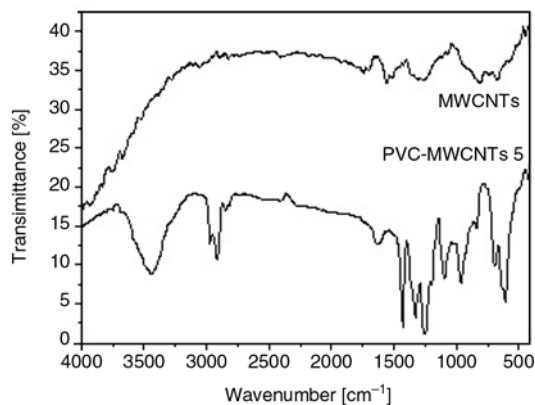
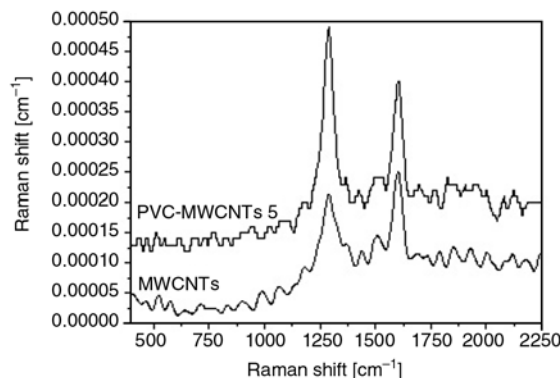**Figure 2.** FT-IR spectra of the pristine MWCNTs and the PVC-MWCNTs 7

Figure 4. Raman spectra of the pristine MWCNTs and the PVC-MWCNTs 7

It indicated that the PVC molecules had been successfully grafted onto the surfaces of the MWCNTs via the Friedel-Crafts alkylation. The grafting mechanism could be deduced as shown in Figure 3.

Raman spectrum has been prevalently applied for providing qualitative information on the status of the sidewall functionalization of CNTs. The Raman spectrum of the pristine MWCNTs and the PVC-MWWNTs are shown in Figure 4. Two usual bands of CNTs were detected for the MWCNTs: the D-band (the vibration of sp^2-bonded carbon atoms in a two-dimensional hexagonal lattice, such as in a graphitic layer) at 1290 cm^{-1} and the G-band (scattering from sp^3-hybridized carbons defects in the hexagonal framework of the MWCNTs walls) at 1600 cm^{-1}. The value of intensity ratio between the D- and G-bands (I_D/I_G) is an indication of the degree of the covalent functionalization of the MWCNTs. Figure 4 showed that I_D/I_G of the pristine MWCNTs was about 0.74, while I_D/I_G was around 1.68 for the PVC-MWWNTs. I_D/I_G of the MWCNTs was enhanced, indicating that more sp^3-hybridized carbons of the nanotube sidewalls were produced after the Friedel-Crafts alkylation.

Transmission electron microscopy (TEM) was employed to detect the structure and morphology of the resulting samples (Figure 5). In the image of the pristine MWCNTs (Figure 5a), it is clear that many pristine MWCNTs were piled up and the average diameter of the pristine MWCNTs is in the range of 20–40 nm. The surface of the pristine MWCNTs is featureless. The convex surfaces of the pristine MWCNTs seem to be smooth with nothing adhering to them. In contrast, it can be found that after the surface Friedel-Crafts alkylation, the surfaces of the MWCNTs are coated with a PVC layer (Figure 5b). Obviously, a core-shell structure with MWCNTs at the center can be clearly observed for the nanohybrids. Furthermore, compared with the pristine MWCNTs, the external diameters of the functionalized MWCNTs was about 30–60 nm which was remarkably increased. As a consequence, we believe such ideal wrapping would be the result of covalent grafting.

Dispersion of the pristine MWCNTs into aqueous solution or organic solvent was very difficult even after it was ultrasonically irradiated. However, dispersion of the PVC-MWCNTs into polar solvents
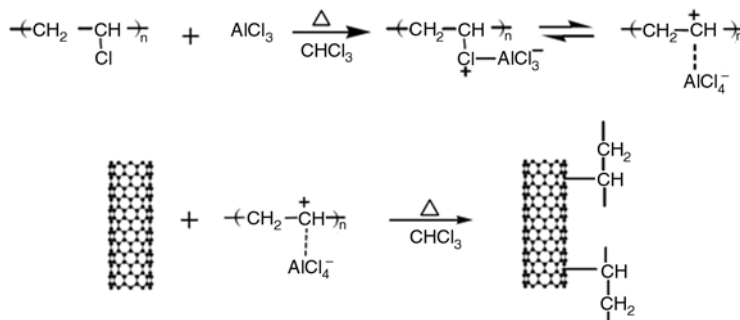

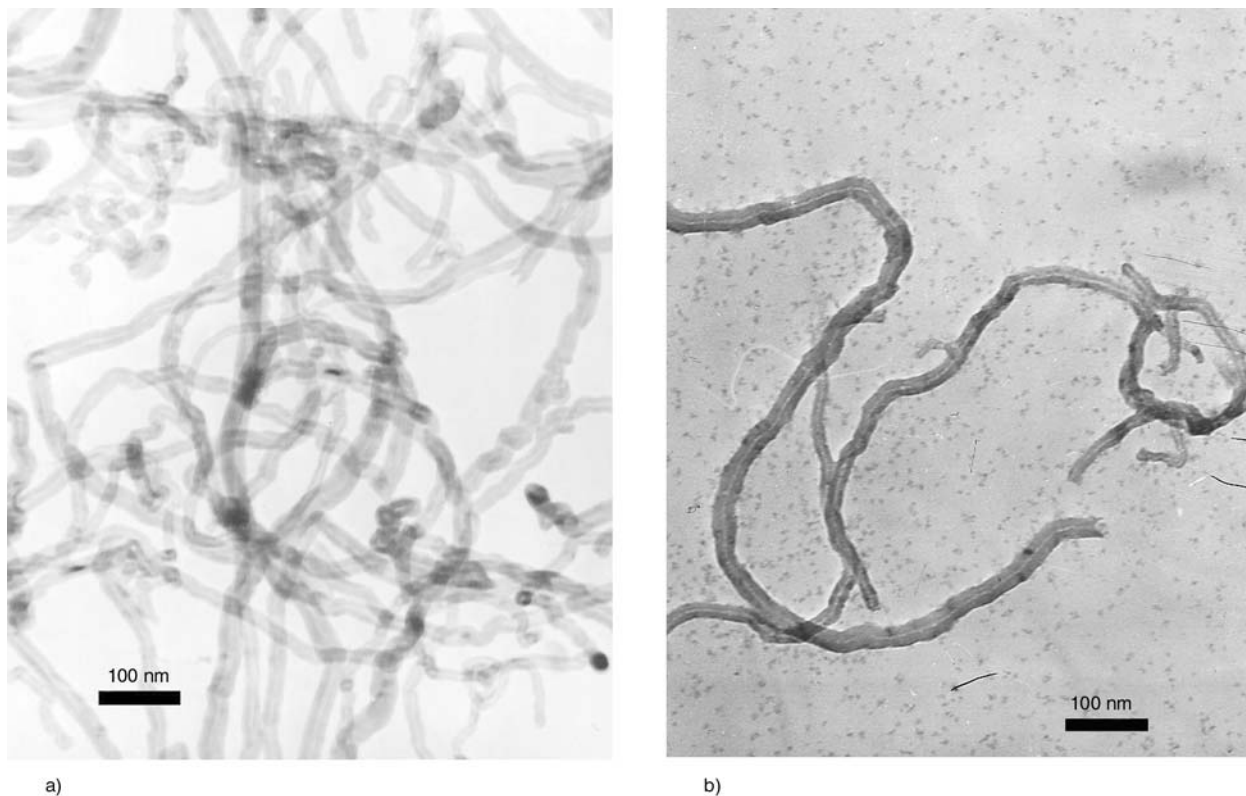**Figure 3.** Proposed mechanism of grafting reaction

Figure 5. TEM images of the pristine MWCNTs and the PVC-MWCNTs 7: (a) pristine MWCNTs; and (b) PVC-MWC-NTs 7

Figure 6. Photographs of the pristine MWCNTs (left) and the PVC-MWCNTs (right) dispersed in THF

such as tetrahydrofuran (THF) was very easy. So the solubility or dispersibility of the functionalized MWCNTs strongly depends on the structure and amounts of the grafted moieties. Figure 6 gives the digital photos of the pristine MWCNTs and the PVC-MWCNTs in THF. It is clear that the dispersibility of the pristine MWCNTs in THF is very poor, and they were only swollen (left). However, the PVC-MWCNTs are dispersable in THF, forming a homogeneous dispersion, and there was no sedimentation observed even after one month as shown in Figure 6 (right). All of the evidence indicates that PVC chains have grafted onto the surface of the MWCNTs via the Friedel-Crafts alkylation.

4. Conclusions

In summary, a facile strategy was developed for the grafting of polymers onto the the ends and sidewalls of the carbon nanotubes via the Friedel-Crafts alkylation catalyzed with strong Lewis acids. The TGA analysis proved that the precedentless high PG% was achieved. The modified MWCNTs exhibited excellent dispersibility in THF and the dispersion had good stability. It is expected that the strategy could be extended to the surface modification of CNTs with other polymers by using the Friedel-Crafts reactions.

References

[1] Sinnott S. B., Andrews R.: Carbon nanotubes: Synthesis, properties, and applications. Critical Reviews in Solid State and Materials Sciences, **26**, 145–249 (2001).
DOI: 10.1080/20014091104189

[2] Terrones M.: Science and technology of the twenty-first century: Synthesis, properties, and applications of carbon nanotubes. Annual Review of Materials Research, **33**, 419–501 (2003).
DOI: 10.1146/annurev.matsci.33.012802.100255

[3] Tasis D., Tagmatarchis N., Bianco A., Prato M.: Chemistry of carbon nanotubes. Chemical Reviews, **106**, 1105–1136 (2006).
DOI: 10.1021/cr050569o

[4] Baughman R. H., Zakhidov A. A., de Heer W. A.: Carbon nanotubes – The route toward applications. Science, **297**, 787–792 (2002).
DOI: 10.1126/science.1060928

[5] Liu P.: Modifications of carbon nanotubes with polymers. European Polymer Journal, **41**, 2693–2703 (2005).
DOI: 10.1016/j.eurpolymj.2005.05.017

[6] Shi J-H., Yang B-X., Goh S. H.: Covalent functionalization of multiwalled carbon nanotubes with poly(styrene-co-acrylonitrile) by reactive melt blending. European Polymer Journal, **45**, 1002–1008 (2009).
DOI: 10.1016/j.eurpolymj.2008.12.040

[7] Zhang K., Lim J. Y., Choi H. J.: Amino functionalization and characteristics of multi-walled carbon nanotubes/poly(methyl methacrylate) nanocomposites. Diamond and Related Materials, **18**, 316–318 (2009).
DOI: 10.1016/j.diamond.2008.08.005

[8] Baskaran D., Mays J. W., Bratcher M. S.: Polymer-grafted multiwalled carbon nanotubes through surface-initiated polymerization. Angewandte Chemie International Edition, **43**, 2138–2142 (2004).
DOI: 10.1002/anie.200353329

[9] Li S. Y., Chen H., Bi W. G., Zhou J. J., Wang Y. H., Li J. Z., Cheng W. X., Li M. Y., Li L., Tang T.: Synthesis and characterization of polyethylene chains grafted onto the sidewalls of single-walled carbon nanotubes via copolymerization. Journal of Polymer Science Part A: Polymer Chemistry, **45**, 5459–5469 (2007).
DOI: 10.1002/pola.22290

[10] Park S. J., Cho M. S., Lim S. T., Choi H. J., Jhon M. S.: Synthesis and dispersion characteristics of multi-walled carbon nanotube composites with poly(methyl methacrylate) prepared by *in-situ* bulk polymerization. Macromolecular Rapid Communications, **24**, 1070–1073 (2003).
DOI: 10.1002/marc.200300089

[11] Oh S. B., Kim H. L., Chang J. H., Lee Y-W., Han J. H., An S. S. A., Joo S-W., Kim H. K., Choi I. S., Paik H-J.: Facile covalent attachment of well-defined poly(t-butyl acrylate) on carbon nanotubes via radical addition reaction. Journal of Nanoscience and Nanotechnology, **8**, 4598–4602 (2008).
DOI: 10.1166/jnn.2008.IC15

[12] Liu P.: Facile graft polystyrene onto multi-walled carbon nanotubes via *in situ* thermo-induced radical polymerization. Journal of Nanoparticle Research, **11**, 1011–1016 (2009).
DOI: 10.1007/s11051-008-9563-0

[13] Baskaran D., Sakellariou G., Mays J. W., Bratcher M. S.: Grafting reactions of living macroanions with multi-walled carbon nanotubes. Journal of Nanoscience and Nanotechnology, **7**, 1560–1567 (2007).
DOI: 10.1166/jnn.2007.459

[14] Mountrichas G., Pispas S., Tagmatarchis N.: Grafting-to approach for the functionalization of carbon nanotubes with polystyrene. Materials Science and Engineering: B, **152**, 40–43 (2008).
DOI: 10.1016/j.mseb.2008.06.006

[15] Baek J-B., Lyons C. B., Tan L-S.: Covalent modification of vapour-grown carbon nanofibers via direct Friedel-Crafts acylation in polyphosphoric acid. Journal of Materials Chemistry, **14**, 2052–2056 (2004).
DOI: 10.1039/b401401d

[16] Balaban T. S., Balaban M. C., Malik S., Hennrich F., Fischer R., Rosner H., Kappes M. M.: Polyacylation of single-walled carbon nanotubes under friedel-crafts conditions: An efficient method for functionalizing, purifying, decorating, and linking carbon allotropes. Advanced Materials, **18**, 2763–2767 (2006).
DOI: 10.1002/adma.200600138

[17] Han S-W., Oh S-J., Tan L-S., Baek J-B.: Grafting of 4-(2,4,6-trimethylphenoxy)benzoyl onto single-walled carbon nanotubes in poly(phosphoric acid) via amide function. Nanoscale Research Letters, **4**, 766–772 (2009).
DOI: 10.1007/s11671-009-9308-8

[18] Müller J., Dongmann G., Frischkorn C. G. B.: The effect of aluminium on the formation of PAH, methyl-PAH and chlorinated aromatic compounds during thermal decomposition of PVC. Journal of Analytical and Applied Pyrolysis, **43**, 157–168 (1997).
DOI: 10.1016/S0165-2370(97)00065-X

Comparative study of the morphology and properties of PP/LLDPE/wood powder and MAPP/LLDPE/wood powder polymer blend composites

D. G. Dikobe, A. S. Luyt**

Department of Chemistry, University of the Free State (Qwaqwa Campus), Private Bag X13, Phuthaditjhaba, 9866, South Africa

Abstract. In this study, polypropylene (PP)/linear low-density polyethylene (LLDPE) and maleic anhydride grafted polypropylene (MAPP)/LLDPE blend systems were comparatively investigated. The blends and composites contained equal amounts of the two polymers, and the compatibility and miscibility between the two polymers were investigated. Composites with 10, 20 and 30 wt% wood powder (WP), but still with equal amounts of the two polymers, were prepared and investigated. The morphologies, as well as mechanical and thermal properties, of the blends and the blend composites were investigated. The MAPP/LLDPE blend and composites showed better properties than the PP/LLDPE blend and composites as a result of the stronger interfacial interaction between MAPP, LLDPE and WP. The SEM and DSC results of the PP/LLDPE/WP blend composites showed that WP located itself more in the LLDPE phase. In the MAPP/LLDPE/WP composites the WP was in contact with both polymers, although it had a greater affinity for MAPP. The TGA results show that the MAPP/LLDPE blend and composites are more thermally stable than the PP/LLDPE blend and composites.

Keywords: *polymer composites, polypropylene, maleic anhydride grafted polypropylene, linear low-density polyethylene, wood powder*

1. Introduction

The blending of two or more polymers is a cheaper and more effective alternative, not only for the development of polymers with new properties, but also for recycling of greener materials [1–3]. Polypropylene/polyethylene (PP/PE) blends are amongst polymer blends that were studied by various researchers [4–6]. Three different types of PE, namely low-density polyethylene (LDPE), high-density polyethylene (HDPE), and linear low-density polyethylene (LLDPE) were used to modify the physical and mechanical behaviour of PP by forming physical blends [2]. The interest in PP and PE is specifically due to the fact that both these polymers are widely used as important engineering materials in the automotive, electrical appliances and packaging industries due to their excellent properties such as rigidity and stiffness, oil resistance and their thermal stability [7]. Apart from these good properties that PP has, its applications are often limited due to its low impact strength and Young's modulus, particularly at low and high temperature loading conditions. These PP drawbacks can be considerably improved by blending PP with other polymers [7–9].

Blending of PP and different PEs largely depends on the miscibility or immiscibility of the two components. PP and LDPE or HDPE are generally considered immiscible in the whole composition range and shows a remarkable phase separation during

cooling/crystallization [2, 7, 9]. On the other hand, PP and LLDPE are considered to be compatible in the liquid state. However, PP/LLDPE miscibility is restricted by the processing conditions, composition and high temperatures. If a blend of PP and LLDPE is cooled from a miscible melt it may separate into two phases resulting in an immiscible blend [10].

The incorporation of fillers into thermoplastics is another method widely used to enhance certain properties. The degree of property enhancement depends on the filler particle size and shape, the content of filler, the surface treatment promoting interaction between the polymer matrix and filler and most importantly the filler's origin [11]. Natural fibres are favoured over synthetic fibres due to strict environmental policies that promote the manufacturing of biodegradable materials. One of the disadvantages of using natural fibres is that they are incompatible with hydrophobic thermoplastics. MA-maleated PP (MAPP) has been widely used at low concentrations as a compatibilizing agent and adhesion promoter for bio-filler filled polypropylene composites. The maleic anhydride (MA) functional group which grafts onto the PP backbone acts as a chemical link between the hydrophobic matrix polymer and the hydrophilic surface of natural fillers [12–17].

Two ways used to improve polymer properties are polymer blending and the use of filler to form polymer composites. These two methods were extensively, but separately used. Studies dealing with polymer blends reinforced with rigid fillers to give three-phase polymer composites are still fairly new [18]. In cases where these studies were done, synthetic and mineral fibres such as talc, glass fibre and calcium carbonate ($CaCO_3$) were used as fillers [18–21]. Very few studies of ternary systems involving natural fibres as reinforcement were reported [11, 22–25].

In this study, PP/LLDPE and MAPP/LLDPE blend systems, where the two polymers in each system were mixed in equal quantities, were comparatively investigated. This work was primarily a study on the interaction of wood powder (WP) particles with one or more of the phases of different 50/50 w/w polyolefin blends, and of the influence of the presence of WP particles and the respective interactions on the crystallization and melting behaviour of the different polymers in the blends. Maleic anhydride

grafted polypropylene (MAPP) was introduced to compare the properties of PP/PE blend composites when one of the polymer phases (PP) is replaced by its functionalized equivalent (MAPP). The morphologies, thermal stabilities and mechanical properties of the blends and blend composites were also investigated.

2. Experimental
2.1. Materials

MAPP, supplied by Pluss Polymers Pvt. Ltd. (India), has a density of 0.91 g·cm^{-3}, a melting point of 161°C, a tensile strength of 24 MPa and a melt flow index (MFI) of 55 g/10 min (190°C, 2.16 kg). PP, supplied by Sasol Polymers (Johannesburg, South Africa) has a density of 0.90 g·cm^{-3}, a melting point of 165°C and MFI of 12 g/10 min (230°C, 2.16 kg). LLDPE, supplied by Sasol Polymers (Johannesburg, South Africa) has a density of 0.94 g·cm^{-3}, a melting point of 127°C and an MFI of 3.5 g/10 min (190°C, 2.16 kg). Pine wood powder (WP), or pine saw dust, was obtained from FBW Taurus (Phuthaditjhaba, South Africa). WP was supplied as a light orange coloured powder with a density of 1.5 g·cm^{-3} and was dried at 120°C for 48 hours. Particles with sizes ≤150 μm were obtained by sieving the dried WP using a laboratory test sieve of 150 μm pore size.

2.2. Preparation of the blends and composites

The blends and blend composites were weighed according to the required ratios (100/0/0, 0/100/0, 50/50/0, 45/45/10, 40/40/20, 35/35/30 w/w PP/LLDPE/WP and MAPP/LLDPE/WP) to make up a total of 38 g (which is the mass required for thoroughly mixing the different components in the Brabender Plastograph 50 ml mixer). Mixing of the samples was done at a temperature of 180°C and a mixing speed of 30 rpm for 15 minutes. The samples were then melt pressed at 190°C and 100 bar for 3 minutes. The pressed samples were allowed to cool at room temperature for 10 minutes.

2.3. Composite analysis

The morphologies of the 50/50 w/w PP/LLDPE and MAPP/LLDPE blends and the 40/40/20 w/w PP/LLDPE/WP and MAPP/LLDPE/WP blend com-

posites were examined using a Shimadzu SSX-550 Superscan scanning electron microscope (SEM) (Bangkok, Thailand). Each sample was immersed in liquid nitrogen to ensure perfect breakage. The fractured surface was sputter coated with gold dust (between 20 and 60 nm) before viewing.

Differential scanning calorimetric (DSC) analyses were carried out in a Perkin-Elmer DSC7 (Waltham, Massachusetts, USA) under flowing nitrogen (20 ml·min^{-1}). Samples with masses of approximately 7.5 mg were heated from 25 to 190°C at a rate of 10°C·min^{-1} in order to eliminate the thermal history, cooled to 25°C at 10°C·min^{-1}, and reheated under the same conditions. Three different samples were analysed for each composition. The melting and crystallization data were obtained from the second scan, and the average and standard deviation values for each thermal property are reported.

Tensile testing was performed under ambient conditions on a Hounsfield H5KS universal tester at a cross-head speed of 50 mm·min^{-1}. Tensile test specimens (gauge length 24 mm, width 5 mm, thickness 2 mm) were prepared using a dumbbell shaped hollow punch. Six samples per composition were analysed.

For dynamic mechanical (DMA) analysis, rectangular samples of 50 mm×12.5 mm×2 mm were used. A Perkin Elmer Diamond DMA (Wellesley, Massachusetts, USA) was used for the evaluation of the storage modulus, loss modulus and mechanical damping factor. The temperature range over which the properties were measured was –100 to 100°C at a heating rate of 5°C·min^{-1} under 30 ml·min^{-1} flowing nitrogen. The tests were carried out at a frequency of 1 Hz.

Thermogravimetric analyses (TGA) were carried out using a Perkin-Elmer TGA7 (Waltham, Massachusetts, USA). Samples with masses of approximately 10 mg were heated from 50 to 600°C at a

heating rate of 20°C·min^{-1} under flowing nitrogen (20 ml·min^{-1}).

3. Results and discussion
3.1. Scanning electron microscopy (SEM)

The morphology of immiscible polymer blends depends on the components, ratios, component melt viscosities, and processing conditions. In most heterogeneous systems, a morphology whereby one phase is distributed in another phase is observed. Long *et al.* [10] used polarized optical microscopy (POM) to study the morphology of PP/LLDPE blends and reported different morphologies when various contents of polymers were used. In a 90/10 w/w PP/LLDPE blend, PP spherulites were observed while LLDPE appeared as domains in the PP matrix. In blends where the PP content was lower, the PP spherulites disappeared and LLDPE became the continuous phase. Hassan *et al.* [26] used SEM to study the morphology of an 80/20 w/w PP/LLDPE binary blend and observed a discrete phase of LLDPE as domains sticking to the surface of the PP matrix. These droplets were quite uniformly distributed/dispersed rather than dissolved inside the PP matrix. The droplet formation shows that PP and LLDPE were immiscible and thus they were microscopically separated in the blends.

The SEM photos of the 50/50 w/w PP/LLDPE and MAPP/LLDPE systems are shown in Figures 1a and 1b respectively. Both systems appear to have a co-continuous morphology and as a result it was difficult to identify the individual polymers in the blends. Wang *et al.* [7] studied the morphology of a 50/50 w/w PP/LLDPE blend and reported a co-continuous two phase structure that could be broken down into an island-like structure by manual deformation. Zhang *et al.* [4] and Liang *et al.* [27] used two-dimensional wide-angle X-ray scattering to
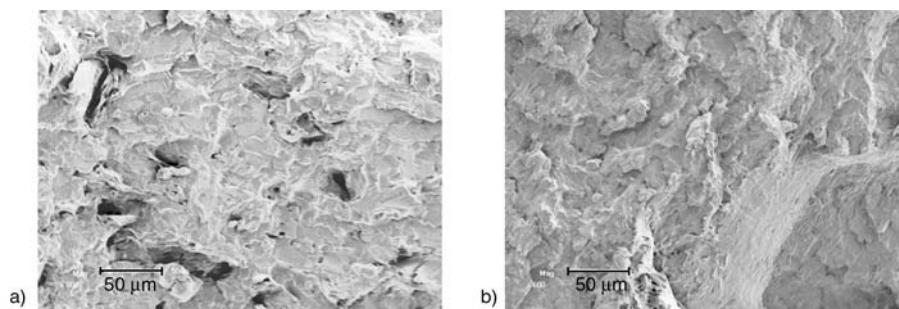

Figure 1. SEM photos of the fracture surfaces of (a) 50/50 w/w PP/LLDPE and (b) 50/50 w/w MAPP/LLDPE (600× magnification)
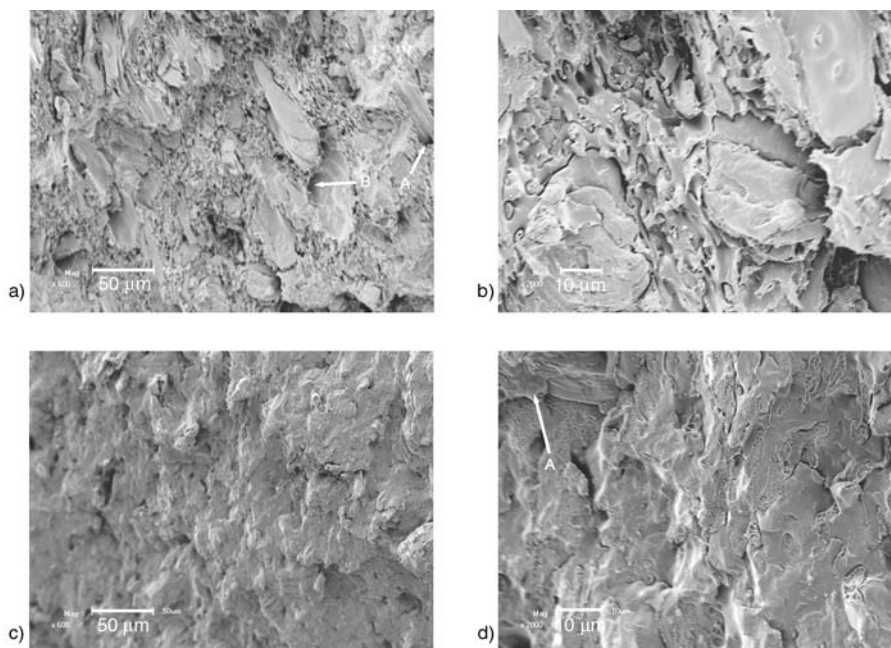
Figure 2. SEM photos of the fracture surfaces of (a) 40/40/20 w/w PP/LLDPE/WP (600× magnification); (b) 40/40/20 w/w PP/LLDPE/WP (2000× magnification); (c) 40/40/20 w/w MAPP/LLDPE/WP (600× magnification); (d) 40/40/20 w/w MAPP/LLDPE/WP (2000× magnification)

study the morphology and interphase structure of an LLDPE/PP blend. They reported that no cross orientation was observed when PP and LLDPE were blended, and this finding was supported by the lack of change in the orientation of LLDPE even in the presence of PP fibres. Figure 1b shows a much smoother fracture surface, which seems to indicate better interfacial adhesion between MAPP and LLDPE.

The SEM photos of the 40/40/20 w/w PP/LLDPE/WP blend composite (Figures 2a and 2b) show cavities around the WP particles (A), as well as fibre pull-out (B). This indicates a fairly weak interaction between the fibre and the matrix. However, the macroscopic surface structure of the sample looks smoother than that of the PP/LLDPE blend (Figure 1). This may be the result of some affinity between the WP and LLDPE (see discussion of DSC results below). Some authors observed the same for the PP/NR/LLDPE ternary blend which was more homogeneous and had a finer disperse phase particle diameter than the PP/NR binary blend, due to the preference of natural rubber for LLDPE [26].

The SEM photos of the 40/40/20 w/w MAPP/LLDPE/WP composite (Figures 2c and 2d) do not show the highly porous morphology, fibre pull-out and lack of intimate contact between the matrix and fibres, as were observed for the 40/40/20 w/w PP/LLDPE/WP composite (Figures 2a and 2b). The higher magnification photo in Figure 2d shows that WP (indicated by A) seems to be in contact with both MAPP and LLDPE, but that it has more contact with one polymer than with the other one. This polymer is likely to be MAPP, due to its maleic anhydride functional groups that will react/interact with the –OH groups on WP. Since WP seems to have a fairly good interaction with both LLDPE and MAPP, the composite structure should be less porous and the fractured surface smoother at first glance.

3.2. Differential scanning calorimetry (DSC)

The DSC heating curves of the PP/LLDPE and MAPP/LLDPE systems are presented in Figures 3 and 4. The LLDPE endothermic melting peak is at 127°C, while PP and MAPP both melt around 162°C. The PP/LLDPE and the MAPP/LLDPE blends both show two peaks corresponding to the melting points of the two polymers. The DSC curve of the MAPP/LLDPE blend in Figure 4 shows two small endothermic peaks between the melting peaks of LLDPE and MAPP, while there are no intermediate peaks between those of PP and LLDPE in the PP/LLDPE blend (Figure 3). This indicates that there is probable formation of co-crystallites of the higher melting fraction of
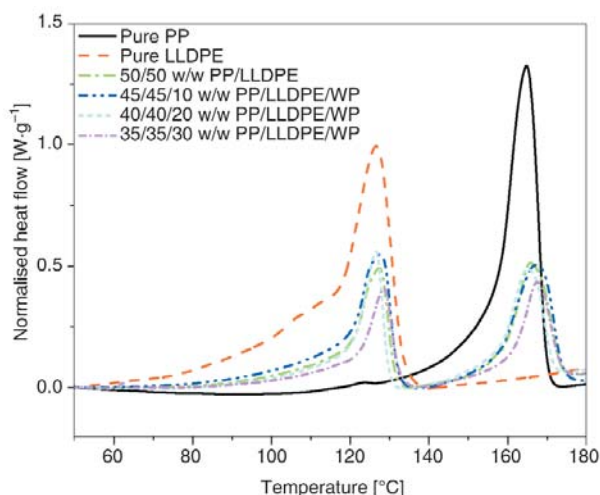
Figure 3. DSC heating curves of PP, LLDPE, the PP/LLDPE blend, and the PP/LLDPE/WP blend composites
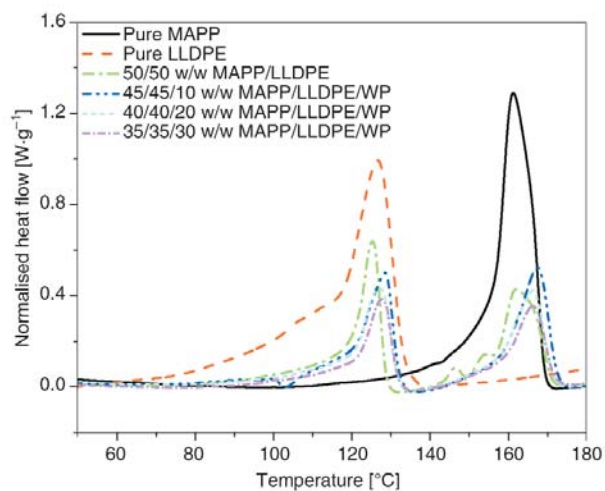

Figure 4. DSC heating curves of MAPP, LLDPE, the MAPP/LLDPE blend, and the MAPP/LLDPE/WP blend composites

LLDPE and the lower melting fraction of MAPP. Fonseca and Harrison [28] investigated co-crystallinity in LDPE/HDPE blends using DSC and a co-crystal melting peak was observed at an intermediate temperature between those of LDPE and HDPE. The DSC data presented a melting-recrystallization-melting phenomenon. They concluded that the co-crystals were the result of crystallites melting, recrystallizing and melting again during the heating cycle of the DSC.

Similar blends were studied by Xu *et al.* [25] who reported that co-crystals can occur in two forms: firstly the linear parts of LDPE may be incorporated in the HDPE crystals; secondly the co-crystals may segregate from both the HDPE and LDPE and exist as a separate part, showing a third intermediate melting peak between the melting peaks of the two pure polymers.

The enthalpy values of the two components in the blends are shown in Table 1. The observed enthalpy values (ΔH^{obs}) of both LLDPE and PP in the 50/50 w/w PP/LLDPE blend are the same as the calculated values (ΔH^{calc}) that were calculated taking into account the fractions of the respective polymers in the blends and assuming that the blending did not change the crystallization behaviour of the respective polymers. This indicates that blending did not significantly change the crystallization characteristics of the two polymers. The presence of WP particles slightly affected the LLDPE crystallization behaviour, while that of PP was not affected by the presence of WP. This is supported by the fact that the $\Delta H_{obs} > \Delta H_{calc}$ in LLDPE while the differences between these values in PP are insignificant.

Table 1. DSC melting data for all the investigated samples

	T^{Peak} [°C]		ΔH^{obs} [J·g^{-1}]		ΔH^{calc} [J·g^{-1}]	
PP/LLDPE/WP [w/w]	**LLDPE**	**PP**	**LLDPE**	**PP**	**LLDPE**	**PP**
100/0/0	–	165.4 ± 4.1	–	79.3 ± 3.8	–	79.3 ± 3.8
0/100/0	127.4 ± 2.3	–	87.7 ± 1.9	–	87.7 ± 1.9	–
50/50/0	128.1 ± 3.1	165.5 ± 2.1	44.2 ± 1.3	38.9 ± 1.7	43.9 ± 2.3	39.6 ± 2.5
45/45/10	127.3 ± 4.3	168.4 ± 2.9	42.2 ± 2.8	34.6 ± 1.5	39.5 ± 1.4	35.7 ± 2.6
40/40/20	127.5 ± 3.8	165.3 ± 1.9	37.3 ± 2.1	30.7± 1.8	35.1 ± 1.5	31.7 ± 3.2
35/35/30	128.4 ± 2.1	167.4± 3.4	32.9 ± 0.5	26.9 ± 1.5	30.7 ± 1.8	27.7 ± 2.1
MAPP/LLDPE/WP [w/w]						
100/0/0	–	161.0 ± 4.1	–	75.3 ± 3.8	–	75.3 ± 3.8
0/100/0	127.4 ± 2.3	–	87.7 ± 1.9	–	87.7 ± 1.9	–
50/50/0	127.1 ± 2.8	162.3 ± 2.3	41.6 ± 0.9	24.8 ± 1.3	43.9 ± 2.1	37.7 ± 1.7
45/45/10	128.5 ± 3.3	167.5 ± 2.5	38.4 ± 0.8	22.7 ± 1.6	39.5± 1.8	33.9 ± 1.6
40/40/20	127.2 ± 1.9	163.4 ± 3.2	33.8 ± 1.1	19.8 ± 1.9	35.1 ± 1.2	30.1 ± 1.1
35/35/30	128.5 ± 2.4	167.6± 3.4	28.1 ± 0.5	17.4 ± 0.8	30.7 ± 1.5	26.3 ± 1.7

T^{Peak} – melting peak temperature; $\Delta H^{obs}/\Delta H^{calc}$ – observed/calculated melting enthalpies

There are differences between the ΔH^{obs} and the ΔH^{calc} values of LLDPE and MAPP in the MAPP/LLDPE blend (Table 1), which indicates that the crystallization behaviour of both these polymers is influenced by the presence of the other polymer in the blend. It seems as if the MAPP crystallization is influenced more by the presence of LLDPE than *vice versa*. The absence of the additional small peaks in all the heating curves of the MAPP/LLDPE/WP blend composites shows that the MAPP probably crystallized on the WP surfaces, which would reduce the co-crystallization of MAPP and LLDPE.

The DSC cooling curves of the PP/LLDPE systems are shown in Figure 5. The LLDPE and PP crystallization peak temperatures are at 105 and 110°C respectively. The 50/50 w/w PP/LLDPE blend shows one crystallization peak at 107°C, despite the immiscibility of the two components. The single crystallization peak for the blend is due to the very close crystallization temperatures of the individual polymers. The most probable reason for the formation of a single crystallization peak is the fact that the polymer blend was cooled at a relatively high rate of 10°C·min⁻¹. The crystallization of PP/HDPE blend-based nanocomposites was studied by Chiu *et al.* [29], who reported a single crystallization exotherm when cooled at 10°C·min⁻¹. Faster cooling rates allow less time for reorganization and therefore prohibit the diffusion and proper separation of one polymer from the other [28]. Li *et al.* [30] studied the miscibility and isothermal crystallization of polypropylene in polyethylene melts,
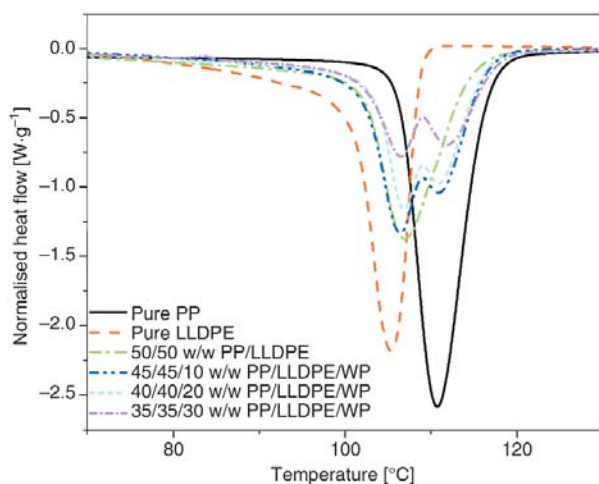
and reported that the crystallization temperature of PP is close to that of HDPE so that the two peaks overlap. The PP/HDPE (20/80) blend showed only a single peak between the crystallization temperatures of PP and HDPE, which was broader than the crystallization peaks of pure PP and HDPE. Similar results were reported for the PP/LLDPE (20/80) blend, but in this system a new peak, which has been identified as the crystallization of PP, appeared at 88°C. It was explained as the dissolution of the PP in the LLDPE in the molten state [30]. The appearance of the lower PP crystallization peak is explained as a delay in the PP crystallization because the concentration of PP in the PE-rich matrix is too low to form nuclei, and hence the crystallization of PP is delayed. During the crystallization of LLDPE, the concentration of PP in the melt increases to the point where PP is able to crystallize at a lower temperature and the crystalline LLDPE act as nuclei for the crystallization of PP. It was further observed that the intensity of the peak at 88°C decreased until the peak disappeared and only one crystallization peak for the PP/LLDPE blend was observed. This is due to the simultaneous crystallization of PP and LLDPE, and is in line with our own observations on the crystallization behaviour of this blend. The presence of WP promotes the separate crystallization of the two polymers. There was a small increase in the crystallization temperature of the LLDPE, while that of PP remained constant in the presence of WP. It seems as if there is some interaction between LLDPE and WP (see SEM discussion above) which retards the LLDPE crystallization, while the crystallization of PP is not affected by the presence of WP. This observation indicates that WP preferably locates itself in LLDPE and retards its crystallization, allowing PP to crystallize first.

The crystallization peaks of pure LLDPE and pure MAPP are at 105 and 110°C respectively (Figure 6). Considering the heating rate and the closeness of the crystallization, it would be expected that the MAPP/LLDPE blend will show a single crystallization peak as was observed for the PP/LLDPE blend. However, in this case two overlapping crystallization peaks at 107 and 110°C are observed. A possible explanation for the separate crystallization peaks in this blend is that MAPP and LLDPE are less miscible in the melt, and that MAPP therefore started crystallizing at its normal crystallization
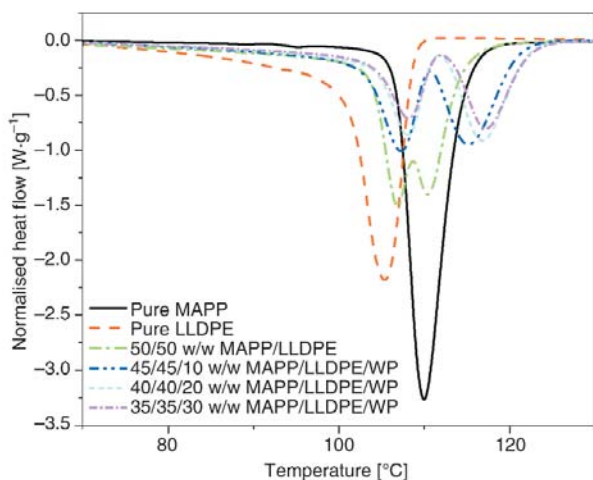

Figure 5. DSC cooling curves of PP, LLDPE, the PP/LLDPE blend, and the PP/LLDPE/WP blend composites

Figure 6. DSC cooling curves of MAPP, LLDPE, the MAPP/LLDPE blend, and the MAPP/LLDPE/ WP blend composites

temperature. However, it seems as if the crystallized MAPP acted as nuclei for the crystallization of LLDPE, and if there was some co-crystallization of some MAPP and LLDPE fractions (see discussion of DSC heating curves). The co-crystalline material probably contained the higher melting fraction of LLDPE and the lower melting fraction of MAPP. Fonseca and Harrison [28] made similar observations, and explained the interaction between the two components as being due to the formation of co-crystallites from the higher temperature portion of LDPE and the lower temperature tail of HDPE. Chiu *et al.* [29] also reported two crystallization isotherms of a PP/HDPE blend in the presence of MAPP.

The crystallization temperatures of both LLDPE and MAPP increased in the presence of WP. Since there should be stronger interaction between WP and MAPP [31], the WP probably acts as a nucleating agent for MAPP crystallization, so that the MAPP starts crystallizing at a higher temperature. Both the WP and the crystallized MAPP will nucleate LLDPE crystallization, so that the LLDPE also starts crystallizing at a higher temperature. This to

some extent explains the SEM observations that both polymers are in contact with WP, but that more of the one polymer (probably MAPP) seems to be in contact with the WP.

3.3. Mechanical properties

The tensile modulus (E), elongation at break (ε_b) and tensile strength at break (σ_b) of the polymers, blends and blend composites are shown in Table 2. All the mechanical property values of the pure polymers have the trend: PP>MAPP>LLDPE. However, the MAPP/LLDPE blend has better mechanical properties than PP/LLDPE. Morphology is a major determinant of the properties of heterogeneous polymer blends. Weak adhesion would result in poor mechanical properties in the blends. The inferior properties of the PP/LLDPE blend can be confirmed from the SEM photo of the blend (Figure 1a), which shows incompatibility. The voids observed in this blend will act as defects when mechanical stress is applied. The MAPP/ LLDPE blend shows almost no voids (Figure 1b) that should give rise to better mechanical properties.

A continuous increase in Young's modulus in the composites of both types of blends indicates the ability of the composites to resist deformation as more fibre is added. This is due the stiff characteristic of the fibres. The Young's modulus of all the PP/LLDPE/WP blend composites is higher than those of the comparable MAPP/LLDPE/WP blend composites. This is understandable considering that pure PP is rigid and has a higher modulus than MAPP.

The blending of MAPP and LLDPE resulted in a blend with elongation at break higher than those of the individual polymers. However, the elongation at break of the PP/LLDPE blend is lower than the two individual polymers, and is related to the incompatibility of the two polymers. The increase

Table 2. Tensile properties of MAPP/LLDPE/WP and PP/LLDPE/WP blend composites

	$E \pm sE$ [MPa]	$\varepsilon_b \pm s\varepsilon_b$ [%]	$\sigma_b \pm s\sigma_b$ [MPa]	$E \pm sE$ [MPa]	$\varepsilon_b \pm s\varepsilon_b$ [%]	$\sigma_b \pm s\sigma_b$ [MPa]
	MAPP/LLDPE/WP [w/w]			**PP/LLDPE/WP [w/w]**		
100/0/0	377.7 ± 20.3	13.3 ± 1.2	24.4 ± 0.5	498.5 ± 13.5	26.7 ± 2.5	29.9 ± 1.3
0/100/0	323.2 ± 17.6	10.5 ±1.4	15.3 ± 1.6	323.2 ± 17.6	10.5 ± 1.4	15.3 ± 1.6
50/50/0	770.2 ± 19.6	18.9 ± 2.4	18.7 ± 1.5	612.2 ± 11.2	10.7 ± 0.9	17.6 ± 0.6
45/45/10	784.4 ± 22.5	3.8 ± 1.4	15.8 ± 1.7	850.9 ± 29.8	3.2 ± 0.2	14.8 ± 0.2
40/40/20	794.5 ± 35.9	3.7 ± 0.2	10.6 ± 1.4	887.8 ± 27.2	2.8 ± 0.2	8.4 ± 1.1
35/35/30	878.7 ± 43.6	2.5 ± 0.2	10.3 ± 1.4	946.7 ± 30.9	1.9 ± 0.1	5.7 ± 0.4

E – tensile modulus, ε_b – elongation at break, σ_b –tensile strength

in the elongation at break of the MAPP/LLDPE blend is related to an interaction that leads to the formation of the co-crystallites between MAPP and LLDPE. The elongation at break of the MAPP/LLDPE/WP blend composites is higher than that of the comparable PP/LLDPE/WP blend composites, which is in line with the observations on the respective blends.

Pure PP shows better stress at break values than pure MAPP (Table 2), but the difference is not significant, and therefore any differences between the stress at break values of the blends and blend composites may be explained in terms of reduced or improved interactions between the different components in the samples. It is interesting that the MAPP/LLDPE blend shows a higher average stress at break than the PP/LLDPE blend, despite the higher stress at break for pure PP. This is in line with the conclusion from the SEM observations that there seems to be stronger interaction between MAPP and LLDPE. For both MAPP/LLDPE and PP/LLDPE the stress at break values are between those of pure LLDPE and pure MAPP or PP, and this indicates (at least partial) co-continuity between the LLDPE and MAPP/PP phases. The PP/LLDPE/WP composites show a decrease in stress at break with increasing fibre content, which is the result of poor interaction between WP and the polymers in the blend matrix, and of the fibres acting as defect centres for crack propagation. The MAPP/LLDPE/WP composites also show lower stress at break values than the individual polymers or the blend, but the vales are generally higher than the respective values for the PP/LLDPE/WP composites. The better interaction between MAPP and WP would cause better stress transfer, but not significant enough to maintain or even improve the tensile strength at break of the composites compared to the pure polymers or the blend.

3.4. Dynamic mechanical analysis (DMA)

The storage modulus is closely related to the load carrying capacity of the material [32]. The storage modulus curves of PP, MAPP, LLDPE, the PP/LLDPE and MAPP/LLDPE blends, and their 10% WP containing composites are presented in Figure 7. The storage modulus values of PP and MAPP are very close to each over the whole temperature range. This indicates that the stiffness of PP and
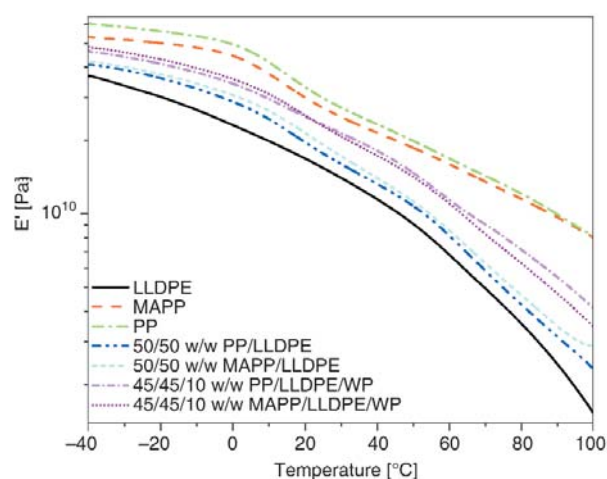
Figure 7. DMA storage modulus curves of PP, MAPP, LLDPE, their blends and their 10% WP containing blend composites

MAPP is similar, and that maleic anhydride grafting did not significantly change this property. A continuous decrease in the storage modulus of MAPP and PP with increasing temperature is observed, with a faster decrease around the glass transition temperature (16°C). The storage modulus of LLDPE is lower than those of MAPP and PP over the whole temperature range, and the difference becomes more significant at higher temperatures. The storage moduli of the PP/LLDPE and MAPP/LLDPE blends are only slightly higher than those of LLDPE, but observably lower than those of PP and MAPP. However, the storage moduli of the MAPP/LLDPE blend are slightly higher than those of the PP/LLDPE blend, probably due to some interaction between MAPP and LLDPE. The PP/LLDPE/WP and MAPP/LLDPE/WP samples have almost the same storage moduli, but higher than those of the blend. This is due to the stiffening effect of the WP. The storage modulus results of the different samples are not in line with the tensile modulus results (Table 2). As already discussed, the tensile moduli of the blends and 10% WP containing composites are observably higher than those of the pure polymers. The reason for this is probably that dynamic mechanical analysis involves only weak stresses, and that the adhesion (or lack of adhesion) between the filler and matrix has a different influence on the storage modulus compared to the tensile modulus [32].

The mechanical loss/damping factor is the ratio of loss modulus to storage modulus and is represented as tanδ. The damping properties of the material
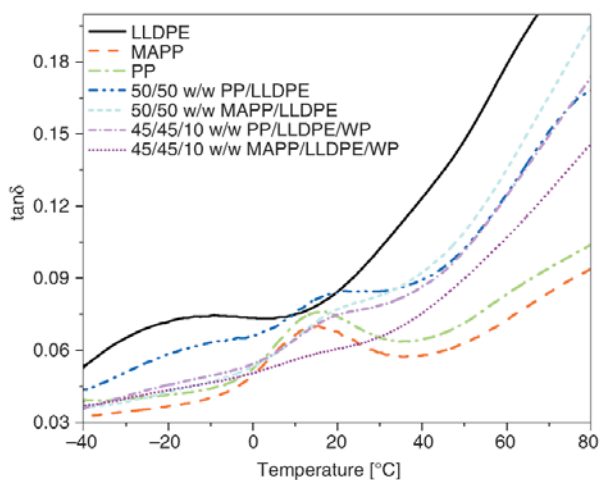
Figure 8. Loss factor curves of PP, MAPP, LLDPE, their blends and their 10% WP containing blend composites

give the balance between the elastic phase and the viscous phase in a polymeric structure. The damping behaviour of a polymer blend is governed by the mechanical relaxation of the two blended polymers, the content used and the interface between the two polymers. In composites, the damping transitions are characterized by the mechanical relaxation of the polymer matrix and the filler, the content used and the filler size or length [33, 34]. Figure 8 shows a comparison of tanδ as a function of temperature of PP, MAPP, LLDPE, the PP/LLDPE and MAPP/LLDPE blends, and their 10% WP containing blend composites. Both PP and MAPP have a β-transition peak at about 16°C. This transition corresponds to the glass transition (T_g) of the amorphous region in PP and MAPP [24, 33]. LLDPE has a β-transition at –15°C, which is related to the movement of polymer side or short chains [35]. The damping peaks in the blend and the blend composites show a decrease in intensity compared to the pure polymers. With the presence of other components in the polymer, the amount of polymer in a blend or composite decreases and the polymer structure becomes partially loosened so as to accommodate the other component. The decrease in the quantity of matrix used and the loosening of the polymer structure lead to a reduction in the intensity of the damping peak [33].

The PP/LLDPE blend shows peaks related to the PP and the LLDPE transitions, and the presence of both these transitions indicate the incompatibility of the two polymers [35]. In the MAPP/LLDPE blend, the LLDPE transition has disappeared,

whereas the MAPP glass transition has broadened and has slightly shifted to a higher temperature of 20°C. This indicates that the polymer chain mobility has been restricted due to the partial miscibility of and/or the interfacial interaction between MAPP and LLDPE.

In the PP/LLDPE/WP composites the transition related to LLDPE disappears, while the PP transition is still visible at the same temperature as in the PP/LLDPE blend. This may be due to the stronger interaction between LLDPE and WP. The MAPP glass transition, which is clearly visible for the MAPP/LLDPE blend, disappears when WP is present in the MAPP/LLDPE blend. This indicates that WP influences the MAPP chain mobility due to the interaction between WP and MAPP. The damping factor values of the MAPP containing composites are generally lower than those of the PP containing composites. This indicates that the energy dissipation of the MAPP containing systems is lower than that of the PP containing systems. Since energy dissipation occurs at the interface, the better interfacial adhesion in the MAPP containing systems may be responsible for the lower dissipation of energy. Similar results were reported by Kim *et al.* [34].

3.5. Thermogravimetric analysis (TGA)

The TGA curves of the different samples are shown in Figures 9 and 10. PP, LLDPE and the PP/LLDPE blend all have a single degradation step. PP starts degrading at 330°C while LLDPE starts degrading at 400°C. The single degradation step for both polymers confirms that the polymers are composed
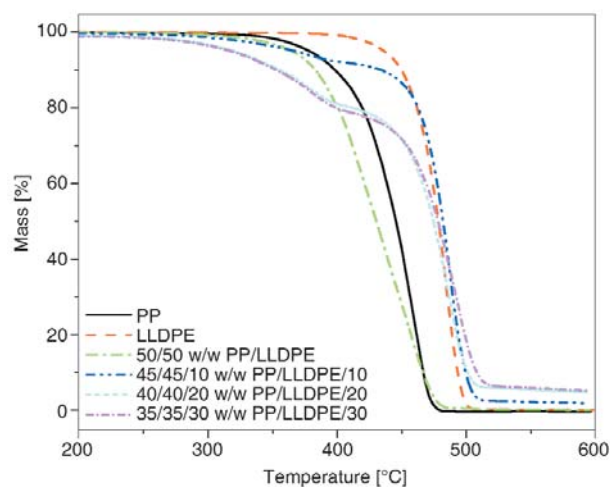

Figure 9. TGA curves of PP, LLDPE, the PP/LLDPE blend, and the PP/LLDPE/WP blend composites

of the carbon-carbon bonds in the main chain, thereby allowing a temperature increase to promote random scission, with associated thermal degradation and thermal depolymerization taking place at a weak part of the polymer main chain [34]. Above 450 and 500°C, for PP and LLDPE respectively, no residue or char was visible. The PP/LLDPE blend starts degrading at 310°C, despite the fact that the two individual polymers are both degrading at higher temperatures, and leaves no residue. Mourad [36] studied the thermo-mechanical characteristics of thermally aged polyethylene/polypropylene blends and reported that the 50/50 w/w PP/PE blend had a lower degradation temperature than the pure polymers and the PP/PE blends of other ratios. The decrease in the thermal stability of the PP/ LLDPE blend is probably due to the presence of voids in the blend (Figure 1a) which trap oxygen that will promote the degradation process and cause a decrease in thermal stability.

The PP/LLDPE/WP blend composites have two degradation steps. The first step corresponds to the degradation of WP. The depolymerization of hemi-celluse occurs between 150 and 350°C, the random cleavage of glycosidic linkages of cellulose between 275 and 350°C, and the degradation of lignin between 250 and 480°C. During the degradation of these WP constituents, volatile materials such as CO and CH$_4$, and residue/char are formed [36]. The second step corresponds to the degradation of the polymer blend matrix. When 30% of WP is used, the residue at 515°C is about 6.5%. The char formation caused a diffusion effect, which inhibited the emission of the gaseous degradation products, showing an apparent increase in the thermal stability of the composite matrix (Figure 7). Chiu *et al.* [30] reported that the inclusion of a nano-filler in PP/HDPE enhanced the blend's thermal stability. Similar findings were reported by Duquesne *et al.* [37] and Peeterbroeck *et al.* [38] while investigating EVA/nanoclay systems. Dikobe and Luyt [24] studied PP/EVA/WP blend composites and reported an increase in the thermal stability of the PP/EVA blend in the presence of WP.

MAPP is more thermally stable than PP, and also has one degradation step which starts at 340°C (Figure 10). The MAPP/LLDPE blend is more thermally stable (starts degrading at 410°C) than the individual polymers. The improved thermal stabil-
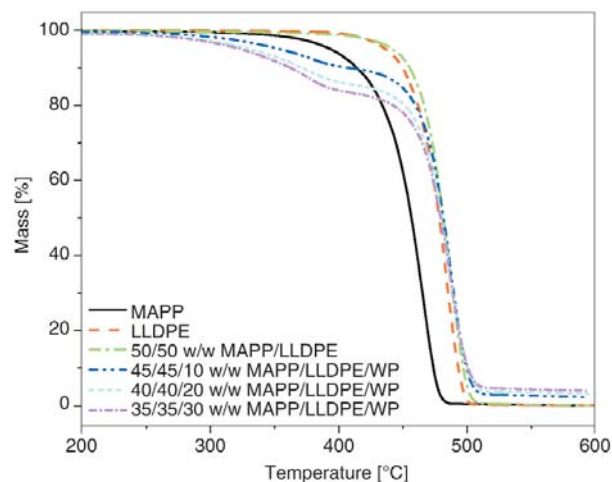

Figure 10. TGA curves of MAPP, LLDPE, the MAPP/ LLDPE blend, and the MAPP/LLDPE/WP blend composites

ity of the MAPP containing blend was due to limited co-crystallization that occurred between MAPP and LLDPE. The resulting polymer blend has an intact structure with fewer voids and hence only a small ability to trap air that will promote degradation. Chiu *et al.* [29] reported that the improvement in thermal stability of smooth/finer surfaced PP/HDPE/PP-MA was due to oxygen and heat permeability reduction in the blend matrix during the heating process. Another reason may be that stronger interaction between the MAPP functional groups and the gaseous degradation products retarded the diffusion of these products out of the sample, so that mass loss was only observed at higher temperatures, indicating an apparent higher thermal stability.

The presence of WP in the MAPP/LLDPE blend also gives rise to two degradation steps. There is a delay in the thermal degradation of WP in the MAPP/LLDPE/WP blend composites, which may also have been the result of a diffusion effect caused by interaction between the gaseous degradation products of WP and the functional groups on MAPP. Although there is an observable increase in the decomposition temperature of the first step, an insignificant change in the decomposition temperature of the second step is observed. Kim *et al.* [17] studied the effect of MAPP and HDPE-MA compatibilizers on rice husk flour (RHF)/polymer composites. They reported that in both RHF-filled PP and RHF-filled LDPE composites, the first and second degradation temperatures slightly shifted to

higher temperatures as compared to the non-treated composites and slightly increased with increasing MAPP and HDPE-MA content.

4. Conclusions

Morphology is an important determinant of the properties of heterogeneous polymer blends and their composites. The MAPP/LLDPE blend and the MAPP/LLDPE/WP blend composites show better mechanical properties than the PP/LLDPE blend and the PP/LLDPE/WP blend composites, because of apparent stronger interaction between the different components of the blend and composites. The SEM photos of the MAPP/LLDPE blend show a smoother fracture surface than the PP/LLDPE blends, which may be an indication of better interaction between MAPP and LLDPE. The DSC heating curves show stronger interaction between and probable co-crystallization of MAPP and LLDPE in the MAPP/LLDPE blend. This interactive co-crystallization seems to be absent when WP is present in this blend, probably because there is a stronger interaction between MAPP and WP which leads to the MAPP preferably crystallizing on the WP surfaces. The WP also seems to locate itself in both polymers, although it has a stronger affinity for MAPP. These interactions seem to be absent between PP and LLDPE in the PP/LLDPE blend and the PP/LLDPE/WP blend composites. The DSC results indicate some interaction between WP and LLDPE in the PP/LLDPE/WP composites, but this seems to be insignificant compared to the interaction between WP and MAPP in the MAPP/LLDPE/WP composites. These interactions, or the lack thereof, are reflected in the non-isothermal crystallization behaviour of the respective polymers in the different blends and composites, in their dynamic mechanical properties, and in the TGA results, where the PP/LLDPE blend is less thermally stable than the individual polymers, but the MAPP/LLDPE blend is more thermally stable than the individual polymers. The MAPP/LLDPE/WP composites are also more thermally stable than the PP/LLDPE/WP composites due to stronger interactions between the different components.

References

[1] Li Z-H., Yang W., Xie B-H., Yang S. Y., Yang M-B., Feng J-M., Huang R.: Effects of compatibilization on the essential work of fracture parameters of in situ microfiber reinforced poly(ethylene terephtahalate)/ polyethylene blend. Materials Research Bulletin, **38**, 1867–1878 (2003).
DOI: 10.1016/j.materresbull.2003.07.007

[2] Chen J-H., Zhong J-C., Cai Y-H., Su W-B., Yang Y-B.: Morphology and thermal properties in the binary blends of poly(propylene-co-ethylene) copolymer and isotactic polypropylene with polyethylene. Polymer, **48**, 2946–2957 (2007).
DOI: 10.1016/j.polymer.2007.03.037

[3] Menyhárd A., Varga J.: The effect of compatibilizers on the crystallization, melting and polymorphic composition of β-nucleated isotactic polypropylene and polyamides 6 blends. European Polymer Journal, **42**, 3257–3268 (2006).
DOI: 10.1016/j.eurpolymj.2006.09.003

[4] Zhang X. M., Ajji A.: Oriented structure of PP/LLDPE multilayer and blends films. Polymer, **46**, 3385–3393 (2005).
DOI: 10.1016/j.polymer.2005.03.004

[5] Nitta K-H., Shin Y-W., Hashiguchi H., Tanimoto S., Terano M.: Morphology and mechanical properties in the binary blends of isotactic polypropylene and novel propylene-co-olefin random copolymers with isotactic propylene sequence. 1. Ethylene-propylene copolymers. Polymer, **46**, 965–975 (2005).
DOI: 10.1016/j.polymer.2004.11.033

[6] Nedkov T., Lednický F.: Morphologies of polyethylene-ethylene/propylene/diene monomer particles in polypropylene-rich polyolefin blends: Flake structure. Journal of Applied Polymer Science, **90**, 3087–3092 (2003).
DOI: 10.1002/app.13050

[7] Wang Y., Zou H., Fu Q., Zhang G., Shen K., Thomann R.: Shear-induced morphological change in PP/LLDPE blend. Macromolecular Rapid Communications, **23**, 749–752 (2002).
DOI: 10.1002/1521-3927(20020901)23:13<749::AID-MARC749>3.0.CO;2-X

[8] Huerta-Martínez B. M., Ramirez-Vargas E., Medellín-Rodrequez F. J., Garcia R. C.: Compatibility mechanisms between EVA and complex impact heterophasic PP-EPx copolymers as a function of EP content. European Polymer Journal, **41**, 519–525 (2005).
DOI: 10.1016/j.eurpolymj.2004.10.021

[9] González J., Albano C., Ichazo M., Díaz B.: Effects of coupling agents on mechanical and morphological behavior of the PP/HDPE blend with two different $CaCO_3$. European Polymer Journal, **38**, 2465–2475 (2002).
DOI: 10.1016/S0014-3057(02)00120-9

[10] Long Y., Shanks R. A., Stachurski Z. H.: Time dependent morphologies of immiscible polymer blends. Journal of Material Science Letters, **15**, 610–612 (1996).
DOI: 10.1007/BF00579266

[11] Albano C., Reyes J., Ichazo M., González J., Chipara M. I.: Influence of gamma irradiation on the thermal stability of blends with previously treated sisal fibre. Polymer Degradation and Stability, **73**, 225–236 (2001).
DOI: 10.1016/S0141-3910(01)00036-2

[12] Salemane M. G., Luyt A. S.: Thermal and mechanical properties of polypropylene-wood powder composites. Journal of Applied Polymer Science, **100**, 4173–4180 (2006).
DOI: 10.1002/app.23521

[13] Suarez J. C. M., Coutihno F. M. B., Sydentricker T. H.: SEM studies of tensile fracture surfaces of polypropylene-sawdust composites. Polymer Testing, **22**, 819–824 (2003).
DOI: 10.1016/S0142-9418(03)00017-5

[14] Amash A., Zugenmaier P.: Morphology and properties of isotropic and oriented samples of cellulose fibre-polypropylene composites. Polymer, **41**, 1589–1596 (2000).
DOI: 10.1016/S0032-3861(99)00273-6

[15] Bledzki A. K., Gassan J.: Composites reinforced with cellulose based fibres. Progress in Polymer Science, **24**, 221–274 (1999).
DOI: 10.1016/S0079-6700(98)00018-5

[16] Harper D., Wolcott M.: Interaction between coupling agent and lubricants in wood-polypropylene composites. Composites Part A: Applied Science and Manufacturing, **35**, 385–394 (2004).
DOI: 10.1016/j.compositesa.2003.09.018

[17] Kim H-S., Lee B-H., Choi S-W., Kim S., Kim H-J., Yang H-S.: The effect of types of maleic anhydride-grafted polypropylene (MAPP) on the interfacial adhesion properties of bio-flour-filled polypropylene composites. Composites Part A: Applied Science and Manufacturing, **38**, 1473–1482 (2007).
DOI: 10.1016/j.compositesa.2007.01.004

[18] Premphet K., Horanont P.: Phase structure of ternary polypropylene/elastomer/filler composites: Effect of elastomer polarity. Polymer, **41**, 9283–9290 (2000).
DOI: 10.1016/S0032-3861(00)00303-7

[19] Albano C., González J., Ichazo M., Rosales C., Urbina de Navcarro C., Parra C.: Mechanical and morphological behavior of polyolefin blends in the presence of $CaCO_3$. Composite Structures, **48**, 49–58 (2000).
DOI: 10.1016/S0263-8223(99)00072-0

[20] Ramos M. A., Berna M. S., Matheu J. P. V.: Effect of talc surface treatment on the mechanical properties of composites based on PP/LDPE blend matrices. Polymer Engineering and Science, **31**, 245–252 (1991).
DOI: 10.1002/pen.760310407

[21] Gupta A. P., Saroop U. K. Verma M.: Studies of mechanical and thermal properties of polypropylene/LLDPE-copolymer blends and its glass fiber compositions. Polymer-Plastics Technology and Engineering, **43**, 937–950 (2004).
DOI: 10.1081/PPT-120038071

[22] Ichazo M. N., Albano C., González J.: Behavior of polyolefins blends with acetylated sisal fiber. Polymer International, **49**, 1409–1416 (2000).
DOI: 10.1002/1097-0126(200011)49:11<1409::AID-PI512>3.0.CO;2-T

[23] Espert A., Vilaplana F., Karlsson S.: Comparison of water absorption in natural cellulosic fibres from wood and one-year crops in polypropylene composites and its influence on their mechanical properties. Composites Part A: Applied Science and Manufacturing, **35**, 1267–1276 (2004).
DOI: 10.1016/j.compositesa.2004.04.004

[24] Dikobe D. G., Luyt A. S.: Morphology and properties of polypropylene/ethylene vinyl acetate copolymer/wood powder blend composites. Express Polymer Letters, **3**, 190–199 (2009).
DOI: 10.3144/expresspolymlett.2009.24

[25] Xu J., Xu X., Chen L., Feng L., Chen W.: Effect of composition distribution on miscibility and co-crystallization phenomena in the blends of low density polyethylene with conventional and metallocene-based ethylene-butene copolymers. Polymer, **42**, 3867–3874 (2001).
DOI: 10.1016/S0032-3861(00)00756-4

[26] Hassan A., Wahit M. U., Chee C. Y.: Mechanical and morphological properties of PP/NR/LLDPE ternary blend- Effect of HVA-2. Polymer Testing, **22**, 281–290 (2003).
DOI: 10.1016/S0142-9418(02)00100-9

[27] Liang S., Wang K., Yang H., Zhang Q., Du R., Fu Q.: Crystal morphology and tensile properties of LLDPE containing PP fibers as obtained via dynamic packing injection molding. Polymer, **47**, 7115–7122 (2006).
DOI: 10.1016/j.polymer.2006.08.021

[28] Fonseca C. A., Harrison I. R.: An investigation of co-crystallization in LDPE/HDPE blends using DSC and TREF. Thermochimica Acta, **313**, 37–41 (1998).
DOI: 10.1016/S0040-6031(97)00465-6

[29] Chiu F-C., Yen H-Z., Lee C-E.: Characterization of PP/HDPE blend-based nanocomposites using different maleated polyolefins as compatibilizers. Polymer Testing, **29**, 397–406 (2010).
DOI: 10.1016/j.polymertesting.2010.01.004

[30] Li J., Shanks R. A., Olley R. H., Greenway G. R.: Miscibility and isothermal crystallisation of polypropylene in polyethylene melts. Polymer, **42**, 7685–7694 (2001).
DOI: 10.1016/S0032-3861(01)00248-8

[31] Dikobe D. G., Luyt A. S.: Morphology and thermal properties of maleic anhydride grafted polypropylene/ethylene-vinyl acetate copolymer/wood powder blend composites. Journal of Applied Polymer Science, **116**, 3193–3201 (2010).
DOI: 10.1002/app.31630

[32] Dufresne A., Dupeyre D., Paillet M.: Lignocellulosic flour-reinforced poly(hydroxybutyrate-co-valerate) composites. Journal of Applied Polymer Science, **87**, 1302–1315 (2003).
DOI: 10.1002/app.11546

[33] Jayanarayan K., Thomas S., Joseph K.: Morphology, static and dynamic mechanical properties of in situ microfibrillar composites based on polypropylene/poly(ethylene terephthalate) blends. Composites Part A: Applied Science and Manufacturing, **39**, 164–175 (2008).
DOI: 10.1016/j.compositesa.2007.11.008

[34] Kim H-S., Kim S., Kim H-J., Yang H-S.: Thermal properties of bio-flour-filled polyolefin composites with different compatibilizing agent type and content. Thermochimica Acta, **451**, 181–188 (2006).
DOI: 10.1016/j.tca.2006.09.013

[35] Dahlan H. M., Zaman M. D. K., Ibrahim A.: The morphology and thermal properties of liquid naturalrubber (LNR)-compatibilized 60/40 NR/LLDPE blends. Polymer Testing, **21**, 905–911 (2002).
DOI: 10.1016/S0142-9418(02)00027-2

[36] Mourad A-H. I.: Thermo-mechanical characteristics of thermally aged polyethylene/polypropylene blends. Materials and Design, **31**, 918–929 (2010).
DOI: 10.1016/j.matdes.2009.07.031

[37] Duquesne S., Jama C., Le Bras M., Delobel R., Recourt P., Gloaguen J. M.: Elaboration of EVA-nanoclay systems- Characterization, thermal behaviour and fire performance. Composites Science and Technology, **63**, 1141–1148 (2003).
DOI: 10.1016/S0266-3538(03)00035-6

[38] Peeterbroeck S., Alexandre M., Jérome R., Dubois Ph.: Poly(ethylene-*co*-vinyl acetate)/clay nanocomposites: Effect of clay nature and organic modifiers on morphology, mechanical and thermal properties. Polymer Degradation and Stability, **90**, 288–294 (2005).
DOI: 10.1016/j.polymdegradstab.2005.03.023